Test and commissioning of the detector system in the $^{209}\text{Bi}^{80+}$ experiment at the Experimental Storage Ring (ESR) at GSI

Rubén López Coto

Master Thesis

Institut für Kernphysik

Mathematisch-Naturwissenschaftliche Fakultät

Westfälische Wilhelms-Universität Münster

July 2010

revised edition
November 21, 2010

WESTFÄLISCHE
WILHELMS-UNIVERSITÄT
MÜNSTER

Science is a game, but a game with reality, it's a game with sharp knifes... If someone cuts carefully an image in thousand peaces, you can solve the jigsaw if you place them correctly again. In a scientific game, your opponent is the Good God. He hasn't just provided the game, but also the rules, although these ones aren't completely known. He has left the half for you to discover or determine them. An experiment is the warm sword you can successfully take up again darkness spirits, but also can defeat you shamefully. The uncertainty is in how many rules has God permanently created and how much seem to be caused by your mental inertia; the solution just can be possible exceeding this limit. Maybe this is the most fascinating thing of the game. Because, in that case, you fight against the imaginary border between God and you, a border that might not exist. ERWIN SCHRÖDINGER.

— Jorge Volpi, In search of Klingsor.

A mis padres

I certify that I have independently written this thesis and no other sources than the mentioned ones have been used.

Referent: Prof. Dr. Christian Weinheimer

Correferent: Dr. Volker Hannen

Contents

Acknowledgements 95

1. Introduction

Quantum ElectroDynamics (QED) is the most complete theory available in Physics at the moment to explain electromagnetic phenomenon. It's also known as *the jewel of physics* [Fey85] because of the non comparable precision of the results it gives. Although it has been checked many times in the laboratory, it hasn't been checked in the presence of very strong electromagnetic fields yet. Highly-charged ions are excellent laboratories to test QED in the presence of extreme strong electromagnetic fields, that can otherwise not be achieved in a laboratory. One can theoretically calculate the hyperfine splitting of the atomic levels for these ions and the energy of the transitions between these levels, but the uncertainties introduced by corrections like the Bohr-Weisskopf effect don't allow a direct extraction of the Quantum Electrodynamics contributions from a single measurement.

To perform a measurement of this contribution, a novel technique has been developed measuring the HFS transitions for two highly charged ions of the same isotope. By comparing the HFS transition in hydrogen and lithium-like ions of the same isotope, the nuclear structure contributions, like the Bohr-Weisskopf effect cancel and it's possible to extract QED contributions with high precision. The ions are accelerated at the GSI facility and are stored in the Experimental Storage Ring (ESR). The ions will be excitated with a laser and the photons emitted in the de-excitation of the ions have to be measured. Photons emitted due to the transitions will be shifted because of the Doppler effect. The task that has to be achieved is to detect the shifted photons.

The present thesis will explain the improvements on the detector systems at the ESR, in order to measure the hyperfine splitting of Lithium-like Bismuth. The construction and test of a new detection system based on a movable parabolic mirror is presented in detail, followed by results from first test-measurements that have taken place during the period of this thesis.

The structure of this thesis will follow this outline:

- In **Chapter 2** a brief introduction to Quantum Electrodynamics and the theory of the hyperfine level splitting is presented. The topics of highly charged ions, the calculation of their hyperfine splittings and the corrections introduced are explained. An important point on this chapter is the extraction of the Quantum electrodynamics contributions from the HFS transitions in H-like and Li-like ions and how to get rid of the Bohr-Weisskopf effect. Finally, a brief explanation about laser spectroscopy and a description of previous measurements that have taken place at the ESR can be found.

- **Chapter 3** will be about the experimental setup at GSI. It will talk about the process to produce highly charged ions, the acelerating system and the ESR. The

laser system used to excitate the ions will also be discussed. As a conclusion, a brief introduction of the detector system used in the previous experiment and the ones designed for the new one will be given.

- **Chapter 4** describes the main detector system. The parabolic mirror system will be the principal tool that will be used to detect the signal coming from the Li-like Bismuth ions. A description of the construction and the characteristics of the components is given. The PMT used, as well as all the optical adaptor to optimize its work can also be found in this chapter.

- **Chapter 5** is where the detector system for the forward direction will be presented. A description of all the components as well as the construction and the test measurements done can be found here. A detailed description about the photomultiplier used in this system close the chapter.

- **Chapter 6** presents the parasitic test measurements done at the ESR in order to test and optimize the electronics and data acquistion. All the measurements, their results and conclusions are presented in this chapter.

- **Chapter 7** is the conclusion of this thesis including an outlook of the future work which has to be done before the beamtime expected on Spring 2011.

2. Theoretical background

The theory of the $^{209}\text{Bi}^{80+}$ HFS experiment is presented. Starting with the Schrödinger wave equation an overview of the derivation of the HFS splitting will be presented. The particular case of highly charged ions will be introduced and the splitting and corrections for this case calculated. A brief introduction about laser spectroscopy of highly charged ions will be given and also the particular case of these measurements at the ESR.

2.1. Quantum mechanics

First of all, the Schrödinger equation for the case of atoms with one electron is given by

$$\hat{H}\phi(\mathbf{r}) = E\phi(\mathbf{r}); \quad \text{with } \hat{H} = \frac{-\hbar^2}{2\mu}\nabla^2 - \frac{e^2}{r} \tag{2.1}$$

The solution of this equation lead us to a quantization in the possible energy levels of the atoms [Coh77]:

$$E_n = -Z\frac{\mu e^4}{2\hbar^2}; \quad \text{n} = 1,2,3,\dots \tag{2.2}$$

Corrections introduced in the Hamiltonian H given in equation 2.1 will give a differentiation of the energy levels. The corrections are introduced because of relativistic effects, spin-orbit coupling and the Darwin term [Ari10]. Next we can see the so-called fine structure hamiltonian H':

$$H' = H + W_{rel} + W_{SO} + W_D \tag{2.3}$$

Solving equation 2.1 with the new hamiltonian H' will give a splitting of the energy levels [Dem05].

$$E_{n,j} = E_n \left[1 - \frac{Z^2\alpha^2}{n}\left(\frac{1}{j+1/2} - \frac{3}{4n}\right) \right] \tag{2.4}$$

where $\mathbf{j}=\mathbf{l}+\mathbf{s}$ is the result of coupling the orbital angular momentum $\mathbf{l}$ with the spin $\mathbf{s}$. Equation 2.4 shows that the energy splitting of each level depends just on j, which can take the following values: $|l-s| < j < |l+s|$.

But now the nuclear momentum $\mathbf{I}$ and its coupling with the electron total angular momentum $\mathbf{j}$ should also be considered. Calling $\mathbf{F}=\mathbf{j}+\mathbf{I}$ the total angular momentum of the system, we obtain another splitting on the energy levels. The energy is now given by equation 2.5

$$E_{HFS} = E_{n,j} + \frac{A}{2}[F(F+1) - j(j+1) - I(I+1)]; \quad \text{with } A = \frac{g_I \cdot \mu_K \cdot B_j}{\sqrt{j(j+1)}} \quad (2.5)$$

where g_I is called nuclear g-factor, μ_K the nuclear magneton and B_j the magnetic field generated by the electron at the position of the nucleus.
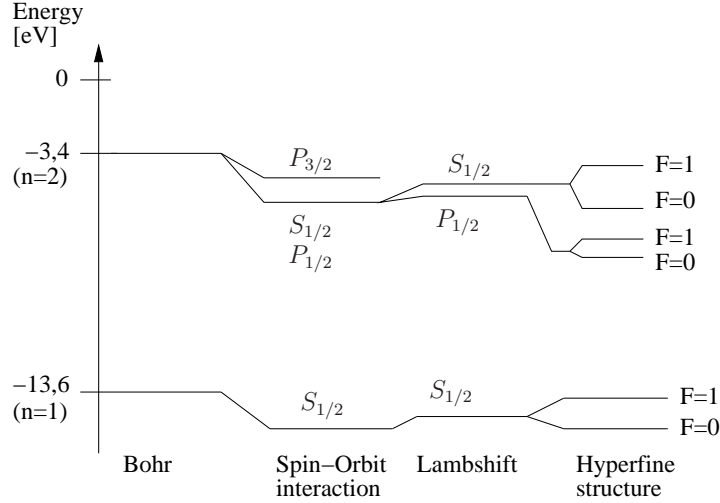
Figure 2.1.: Fine- and Hyperfine- splitting for the first two energy levels in the one-electron atom (Graphic from [Ham08b]).

2.2. Hyperfine transitions in highly charged ions

As it has been said, highly charged ions have peculiar properties that allow to perform tests not possible to be done in a usual laboratory. The most important advantage they offer are the high electric and magnetic fields generated in their proximities. On Figure 2.2, a representation of the electric and magnetic fields reached by highly charged ions can be seen.

But highly charged ions have other remarkable characteristics. Using equation (2.5) one should be able to calculate the hyperfine splitting of every atom, but if we have highly charged ions we need to introduce some corrections to this value. We find a first non relativistic correction, given by [Nör07]

$$\Delta E_{HFS} = \alpha g_I \frac{m_e}{m_p} \frac{F(F+1) - j(j+1) - I(I+1)}{2j(j+1)} m_e c^2 \cdot \frac{(Z\alpha)^3}{n^3(2l+1)} \quad (2.6)$$

More important is the one that includes Quantum Electrodynamics contributions, relativistic effects and nuclear structure contributions [Nör07]:

- Nuclear Mass correction $\mathcal{M}$: due to the finite nuclear mass the nucleus and the electrons move around a common center of mass.
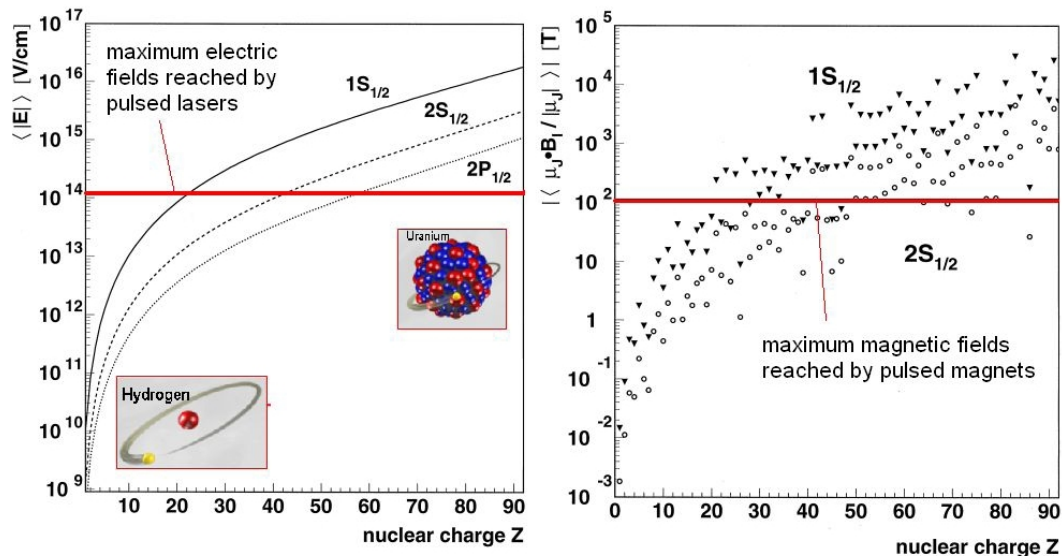
Figure 2.2.: Electric and magnetic fields present in H-like ions a function of their atomic number Z. The red lines mark the maximum artificial fields reachable in a laboratory [Her07], [Loc10a] (Graphic from [Ani10a]).

- Relativistic effects $A(Z\alpha)$: due to the factor $Z\alpha$ is big for heavy ions (Z>>), the nuclear recoil has to be considered to all orders in this parameter.

- Breit-Rosenthal Effect $(1-\delta)$, including the finite distribution of the nuclear charge [Ros32].

- Bohr-Weisskopf Effect $(1-\epsilon)$, that includes the influence of the spatial distribution of the nuclear magnetization [Boh50].

- QED Effect $\frac{\alpha}{\pi}\Delta\epsilon_{QED}$, like self-energy and vacuum-polarization.

$$\Delta E_{HFS} = \alpha g_I \frac{m_e}{m_p} \frac{F(F+1) - j(j+1) - I(I+1)}{2j(j+1)} m_e c^2 \cdot \frac{(Z\alpha)^3}{n^3(2l+1)}$$
$$\cdot \mathcal{M}\left(A(Z\alpha)(1-\delta)(1-\epsilon) + \frac{\alpha}{\pi}\Delta\epsilon_{QED}\right) \quad (2.7)$$

Having the expression of the hyperfine splitting of highly charged ions (Equation 2.7) it should be possible to extract the value of the QED contribution from the measurements. The problem is that althuoght the other effects are well known, the Bohr-Weisskopf effect gives an uncertainty about the order of the QED effects [Nör08].

2.2.1. QED and nuclear structure contributions

Bohr-Weisskopf effect

The Bohr-Weisskopf effect has been introduced to explain inconsistencies between experimental data and theoretical calculations. These differences arise when the nuclear magnetic moment is considered to be a magnetic dipole instead of having a distribution of magnetism over the nuclear volume [Boh50].

Lets call μ_i the magnetic moment of the nucleus and B_j the magnetic field generated by the motion of the electron. The interaction Hamiltonian is given by:

$$H_{\text{int,HFS}} = -\boldsymbol{\mu_i} \cdot \mathbf{B_j} \tag{2.8}$$

The interaction Hamiltonian can also be expressed with the help of a magnetic potential $\mathbf{A}$:

$$-\boldsymbol{\mu} \cdot \mathbf{B} = e\boldsymbol{\alpha} \cdot \mathbf{A}; \quad \text{where } \mathbf{A}_{\text{HFS}}(\mathbf{r}) = \frac{\boldsymbol{\mu_i} \times \mathbf{r}}{4\pi r^3} \tag{2.9}$$

Equation 2.9 represents a point-dipole field [Bei00a].

To estimate the Bohr-Weisskopf effect, some models have been used. The simplest one is due to Bohr and Weisskopf and explains the extended magnetization as due to an additional odd nucleon (only nuclei with an odd number of nucleons have a nuclear spin and thus a magnetic moment in their ground state). This model is therefore called the "single-particle model" [Boh50].

For a more accurate calculation, one should use more realistic nuclear models [Mig83], [Joh70] or [Tom95]. But a comparison between the theoretical predictions for the nuclear magnetic moments with the corresponding experimental values indicates that the deviation of the theory from the experiment may reach up to about 20%-30% [Sha97].
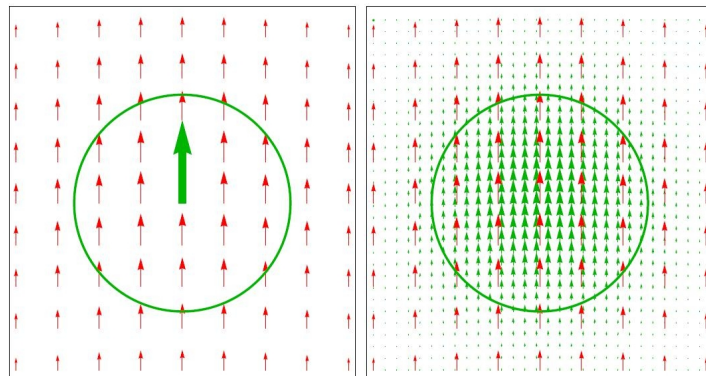

Figure 2.3.: Nucleus with magnetic moment μ_i on an external magnetic field B_j. The difference between considering a punctual magnetic dipole (left) and a distribution of magnetism over the nuclear volume (right) is shown. Image from [Loc10a].

QED contributions

The quantities of interest related to equation 2.7 are QED contributions. These include vacuum polarization and self-energy.

The self-energy terms have their origin in the interaction between an electron with itself. An electron may emit and reabsorb a photon, so terms including this possibility should be included in the equations. If we go to higher interaction orders, more photons may be produced and absorbed by the same electron, although the probability decreases with the number of particles interchanged [Fey61].

The vacuum polarization is a phenomenon that acts in the same way as the dielectric polarization. If we put a point charge q on a dielectric medium, this charge will attract the negative end of the molecular dipoles. Then, the electric field created by this particle will be screened and the effective charge reduced. In QED vacuum also behaves like a dielectric. It sprouts positron-electron pairs that screen the charge existing on the vacuum [Gri87].
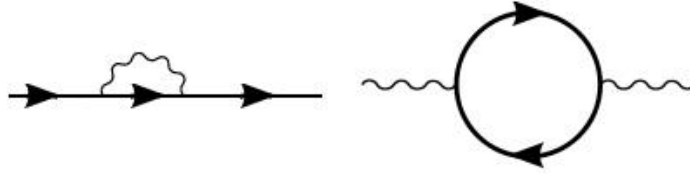

Figure 2.4.: One-loop contribution to self-energy (left) and vacuum polarization (right).

On Figure 2.5 the first order corrections of the factor (α/π) for a bound electron can be seen. For a detailed view on higher orders of this factor see [Bei00b].

Extraction of QED contributions

The uncertainty of the Bohr-Weisskopf effect has the same order as the complete QED contributions, so to be able to extract the latter from the data, one has to get rid of the Bohr-Weisskopf effect. This can be achieved by comparing the HFS energies measured in H-like and Li-like HCI of the same isotope [Sha01]. These energies can be written as follows:

$$\text{H-like:} \quad \Delta E^{(1s)} = \Delta E^{(1s)}_{\text{Dirac}}(1 - \epsilon^{(1s)}) + E^{(1s)}_{\text{QED}} \tag{2.10}$$

$$\text{Li-like:} \quad \Delta E^{(2s)} = \Delta E^{(2s)}_{\text{Dirac}}(1 - \epsilon^{(2s)}) + \Delta E_{\text{int}}(1 - \epsilon^{(\text{int})}) + \Delta E^{(2s)}_{\text{QED}} + \Delta E_{\text{int-QED}} \tag{2.11}$$

Here $\Delta E^{(1s)}_{\text{Dirac}}$ and $\Delta E^{(2s)}_{\text{Dirac}}$ are the one-electron relativistic values of the $1s$ and $2s$ hyperfine splitting including the nuclear charge distribution correction $\epsilon^{(1s)}$ and $\epsilon^{(2s)}$ denote the one-electron BW corrections for the $1s$ and $2s$ states, $\Delta E^{(1s)}_{\text{QED}}$ and $\Delta E^{(2s)}_{\text{QED}}$ are the one-electron QED corrections to the 1s and 2s hyperfine splitting, ΔE_{int} is the interelectronic-interaction contribution to the ground-state hyperfine splitting in the Li-like ion, $\epsilon^{(\text{int})}$ indicates the Bohr-Weisskopf effect on the interelectronic-interaction contribution, and $\Delta E_{\text{int-QED}}$ denotes the combined interelectronic-interaction QED correction.
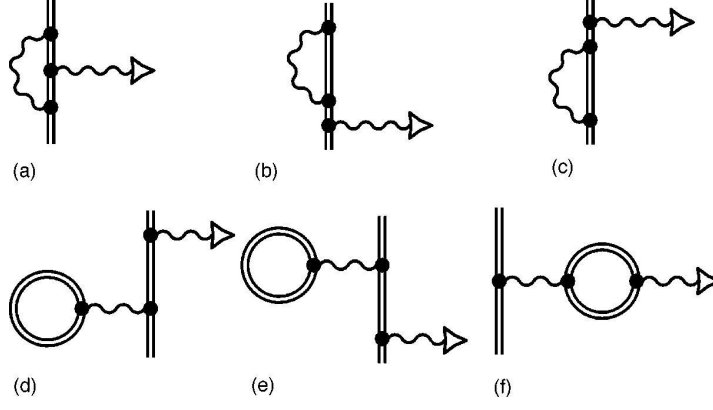
Figure 2.5.: Feynman diagrams representing the QED contributions of order (α/π) to the g factor of a bound electron. The wavy lines denote photons, which mediate the interaction with the external magnetic field represented by a triangle. In each diagram there is also one virtual photon. The solid double line indicates the electron and also virtual leptons in the electron-positron loops. The top diagrams are the self-energy-like corrections, the bottom ones the vacuum polarization-like corrections. For the free electron, only the diagram similar to diagram a contributes. Image from [Bei00b].

The ratios between the BW corrections can be written as a function of αZ:

$$\frac{\epsilon^{(2s)}}{\epsilon^{(1s)}} = f(\alpha Z) \qquad \Rightarrow \qquad \epsilon^{(2s)} = f(\alpha Z) \cdot \epsilon^{(1s)} \tag{2.12}$$

$$\frac{\epsilon^{(\text{int})}}{\epsilon^{(2s)}} = f_{\text{int}}(\alpha Z) \qquad \Rightarrow \qquad \epsilon^{(\text{int})} = f_{\text{int}}(\alpha Z) \cdot f(\alpha Z) \cdot \epsilon^{(1s)} \tag{2.13}$$

Substituting these results in equations (2.10) and (2.11), an equation independent of the BW correction can be written as:

$$\Delta E' = \Delta E^{(2s)} - \xi \Delta E^{(1s)}; \quad \text{where } \xi = f(\alpha Z) \frac{\Delta E_{\text{Dirac}}^{(2s)} + f_{\text{int}}(\alpha Z) \Delta E_{\text{int}}}{\Delta E_{\text{Dirac}}^{(1s)}} \tag{2.14}$$

As we can calculate ξ for a given Z, we now have a formula to accurately extract QED contributions without the uncertainty introduced by the BW effect. The quantity $\Delta E'$ can be calculated with a precision of ($\Delta E'$=61.27$\pm$0.04) meV [Ani10a].

The hydrogen ground-state hyperfine splitting corresponds to a wavelength of λ=21 cm and a mean lifetime of $\tau \approx 10^7$ years. This transition energy scales with the proton number Z as Z^3 and the mean lifetime as Z^{-9}, so for ions with an atomic number Z>70 the transitions enter the visible range and the lifetime is short enough to perform laser spectroscopy on these ions [Küh96]. The theoretical calculated wavelegths for some highly charged ions of interest are represented on Figure 2.6.
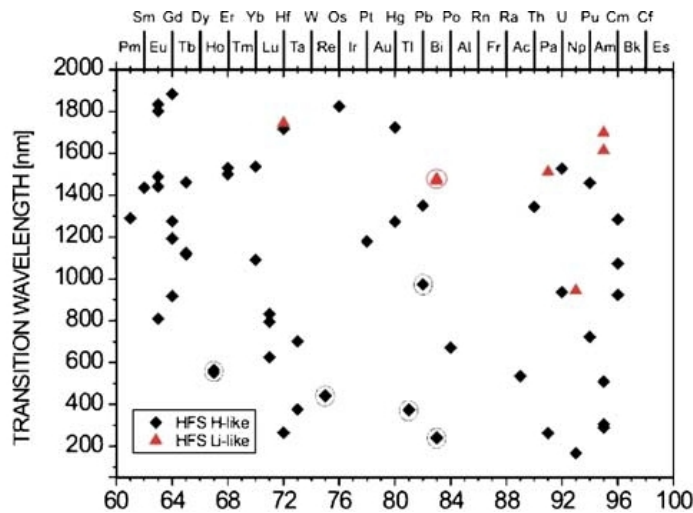
Figure 2.6.: Ground-state hyperfine splittings for H-like and Li-like heavy (Z>60) elements (Graphic from [And10]).

2.3. Studies of HFS transitions with laser spectroscopy

Laser spectroscopy is an accurate tool to study the HFS transitions of highly charged ions. Some measurements have already been performed with different techniques as can be seen on Table 2.1.

Ion	$\Delta E_{\mathrm{HFS}}/\mathrm{eV}$	Wavelength/nm	Experimental	Reference
$^{165}\mathrm{Ho}^{66+}$	2.1645 (6)	572.64 (15)	RETrap	[Cre96]
$^{185}\mathrm{Re}^{74+}$	2.7186 (18)	456.05 (30)	RETrap	[Cre98]
$^{187}\mathrm{Re}^{74+}$	2.7449 (18)	451.69 (30)	RETrap	[Cre98]
$^{203}\mathrm{Tl}^{80+}$	3.21351 (25)	385.822 (300)	RETrap	[Bei01]
$^{205}\mathrm{Tl}^{80+}$	3.24409 (29)	382.184 (340)	RETrap	[Bei01]
$^{207}\mathrm{Pb}^{81+}$	1.2159 (2)	1019.7 (2)	ESR	[See99]
$^{209}\mathrm{Bi}^{82+}$	5.0841 (4)	243.87 (4)	ESR	[Kla94]

Table 2.1.: H-like HFS transition energies and wavelengths from previous experiments (Table from [Krä07]).

All the transitions already measured are from H-like ions, but Li-like highly charge ion HFS transitions haven't been measured yet. The goal of the experiment that will take place at ESR is to be able to measure the HFS wavelength of Li-like Bismuth. This transition has been theoretically calculated before and also indirectly measured on another facility (EBIT in Livermore). The results can be found on Table 2.2.

The experimental values have a relative high uncertainty as the resolution of the measurements was approximately $\Delta\lambda/\lambda = 10^{-3}$. As the upcoming measurements are expecting to achieve a resolution of $\Delta\lambda/\lambda = 10^{-4}$ [Nör08], these results will improve the experimental knowledge of the HFS transition in Li-like Bi by one order of magnitude.

Hyperfine transition/meV	Wavelength/nm	Determination	Reference
797.1 (0,2)	1555.4 (0.4)	Theoretically	[Sha00]
797.15 (0,13)	1555.3 (0.3)	Theoretically	[Sap01]
783.9 (3,0)	1581.6 (6.0)	Theoretically	[Tom00]
820.0 (26,0)	1512 (48)	Experimentally	[Bei98]
791.2 (5,0)	1567 (10)	Experimentally	[Nör08]

Table 2.2.: Theoretical and experimental values measured for the HFS transition wavelength of $^{209}\text{Bi}^{80+}$.

2.4. Measurements at the ESR

Some HFS measurements have already been performed at ESR. Specifically, two HFS transitions have been determined with a $\Delta\lambda/\lambda = 10^{-4}$ precision [Nör08]. The HFS transitions successfully measured were for the ions $^{207}\text{Pb}^{81+}$ and $^{209}\text{Bi}^{82+}$ and the results can be found on Figure 2.7.
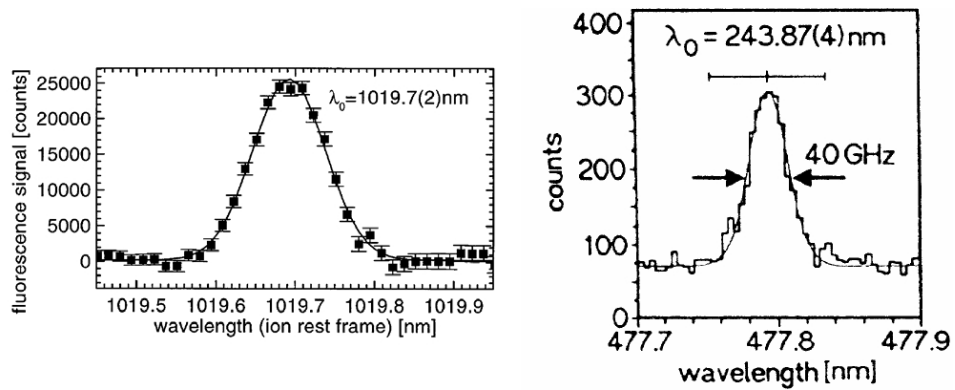
Figure 2.7.: $^{207}\text{Pb}^{81+}$ signal (left) and $^{209}\text{Bi}^{82+}$ signal (right).

Another HFS experiment was performed in order to measure the hyperfine transition of $^{209}\text{Bi}^{80+}$ in 2004, but the signal wasn't found during this beamtime. The main problems were the following:

- The detector system used wasn't very sensitive to the fluorescence photons from the $^{209}\text{Bi}^{80+}$ transition. Simulations have shown that the expected signal rate was only 15 s^{-1} on a background of about 600 s^{-1} (see Section 3.3.1).

- The measured time was insufficient [Ani10a].

On Table 2.3 some data about these ions can be found.

Isotop	Z	Nuclear spin	Hyperfine transition/eV	Wavelength	Mean life/ms
$^{207}\text{Pb}^{81+}$	82	1/2	1.22	1020	52 [See99]
$^{209}\text{Bi}^{82+}$	83	9/2	5.08	244	0.4 [Ham08b]
$^{209}\text{Bi}^{80+}$	83	9/2	≈ 0.80	≈ 1555	82 [Sha98]

Table 2.3.: Ions suitable to be measured at the Experimental Storage Ring (ESR) at GSI. (Source: Nuclear spin from [Man10], Energies/ Wavelengths from [Nör07]).

2.5. Detectors: Photomultiplier Tubes

To detect the photons emitted by the excited ions sensitive light detectors are needed. The rate of photons emitted by the excited ions is very low due to the relatively large lifetime of the $^{209}\text{Bi}^{80+}$ HFS transition of $\tau = 82$ ms, so the detectors need to be able to detect single photons with a very low dark count rate. Photomultiplier tubes are a suitable option to use on the low rate photon experiments.
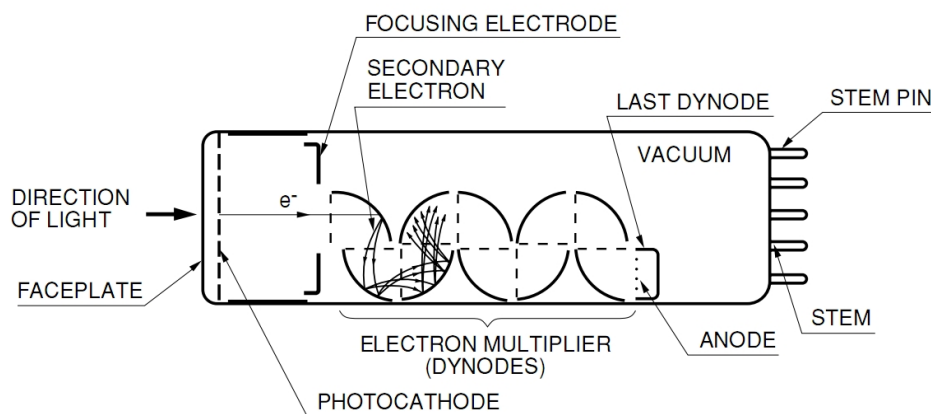

Figure 2.8.: Photomultiplier tube setup.

A photomultiplier tube consists of an input window, a photocathode, focusing electrodes, an electron multiplier and an anode usually sealed into an evacuated glass tube. When a photon in the wavelength sensibility range of the PMT hits the photocathode, an electron can be emitted due to the photoelectric effect and is accelerated due to the high voltage applied. The electron hits the first dynode generating a cascade process. The secondary electrons are collected on the anode [Ham08a]. To apply a voltage difference between the dynodes, a base with a voltage divider where all the pins for the dynodes are connected need to be used.

As it has been explained, a single electron is the only thing needed to have a signal. There are some processes that can create electrons without a photon hitting the photocathode. These electrons constitute the dark count rate of the PMT. The main source of background electrons is thermal emission from the photocathode. In order to reduce it, the PMT needs to be cooled down.
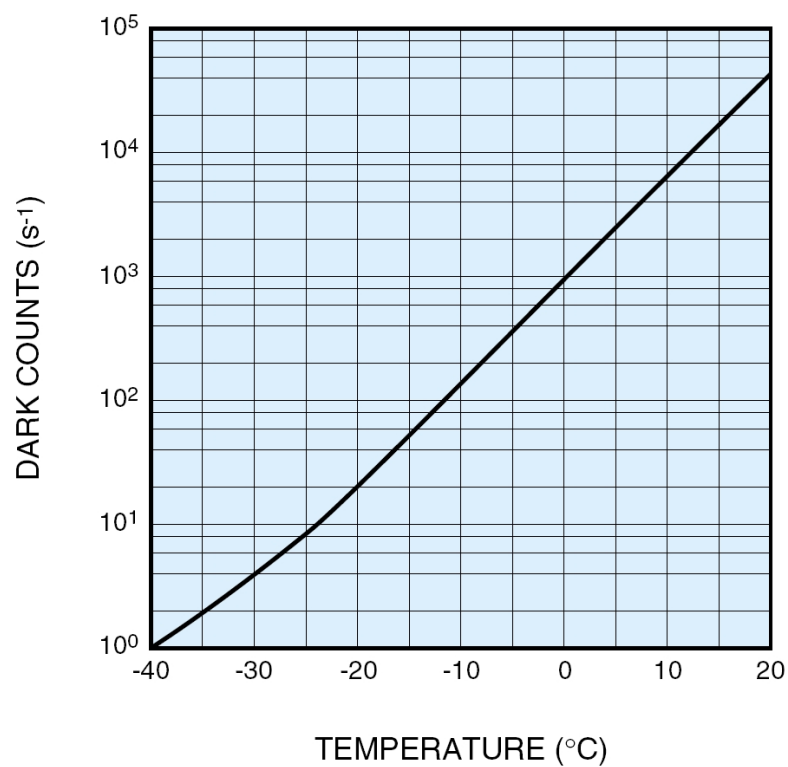
Figure 2.9.: Dark count rate as a function of temperature for the R943-02 PMT.

3. Experimental setup

A description of the experimental setup as well as a view of the facility at the GSI will be given in this chapter. The characteristics of the ion bunch, the production of the highly charged ions (HCI), the storage of the HCI in bunches in the ESR and the laser spectroscopy technique are described on the following pages. Finally, a brief description of detector system used can be found.

3.1. Obtaining and acelerating highly charged ions at the ESR

The main components of the GSI facility are the ion sources, a linear accelerator, two ring accelerators, a fragment separator and experimental caves in the low and the high energy area (Figure 3.1). With these devices particles ranging from protons up to bare uranium can be accelerated. Typically low-charged ions are produced by an ion source, are pre-accelerated to 1.4 MeV/u by a radio-frequency quadrupole structure (RFQ) and further accelerated by the universal linear accelerator (UNILAC) to an energy of typically 11.4 MeV/u for heavy ions. With this energy the ions can be injected into the Synchrotron (SIS) and reach an energy of 30 MeV/u up to 2 GeV/u for Ne^{10+} and up to nearly 1 GeV/u for U^{92+}. To produce these highly charged ions several targets, along the acceleration line and in the SIS, are available where electrons can be stripped off the low-charged ion beam. From the SIS the ions can be extracted either to the high energy experiment area or into the fragment separator (FRS). The latter allows for production and separation of exotic radioactive ion beams that can be stored and analysed in the ESR or reinjected into the SIS [Nov08].

To store or accelerate an ion beam in the ESR, the SIS or in any ring structure, two forces have to be taken into account: the centripetal force, required to bend the beam along the circumference of the ring and the repelling forces of the ion-ion interaction. In the ESR six 60° dipole magnets with a B-field up to 1.6 Tesla are distributed over the ring, keeping the particles on a closed orbit. Additionally, twenty quadrupole magnets (16 short and 4 long) focus the ions in both transversal directions [Fra87]. The ring has a circumference of 108 m and the shape of a drawn-out hexagon with two long sections. In one of these two straight sections of the ESR, an electron cooler is placed and in the other one the detectors are situated.

H- and Li-like Bismuth are electron-cooled at 400 MeV/u, and two bunches of 5-10 m length are formed by applying the second harmonic of the rotation frequency at RF cavities. At 400 MeV their velocity is $\beta = 0.71$, such that the wavelength of the HFS transitions are shifted to the visible regime. The wavelength for the H-like and Li-like
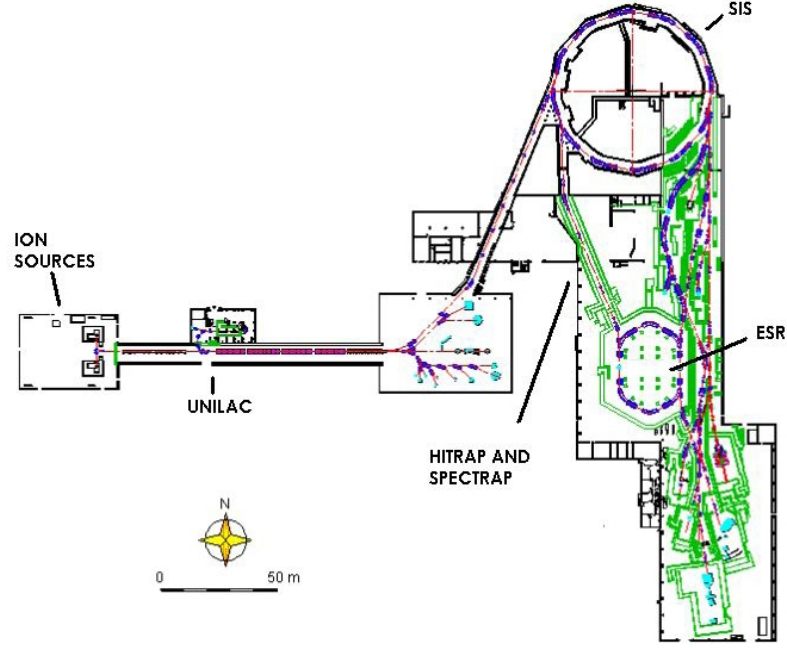
Figure 3.1.: GSI facility. Image from [Nör07].

Bismuth in the collinear and in the anti-collinear direction in the laboratory system are given by equations 3.1 and 3.2:

$$\text{H-like (Collinear):} \quad \lambda_{\text{lab}}^{\uparrow\uparrow} = \lambda_0 \frac{1}{\gamma(1-\beta)} \longrightarrow \lambda_{\text{lab}}^{\uparrow\uparrow} = 597.7 \text{ nm} \quad (3.1)$$

$$\text{Li-like(Anti-collinear):} \quad \lambda_{\text{lab}}^{\uparrow\downarrow} = \lambda_0 \frac{1}{\gamma(1+\beta)} \longrightarrow \lambda_{\text{lab}}^{\uparrow\downarrow} = 634.7 \text{ nm} \quad (3.2)$$

The wavelengths in the laboratory system have been calculated using the results included on Table 2.3.

3.2. Laser spectroscopy at the ESR

The laser beam to excitate the ions will be sent through the electron cooler section, opposite to the section where all the detectors are placed, in order to avoid that laser stray light increase the dark count rate. This can be done because the lifetimes of the HFS transitions are relatively long and the fluorescence will take place all over the ring. The procedure for the laser spectroscopy is the following: There are two bunches of ions stored in the ESR. The laser is synchronized with the RF frequency illuminating one of the bunches with a repetition rate of 50 Hz. The illuminated one is the signal bunch and the other one is the reference bunch. We will measure both bunches and the resulting
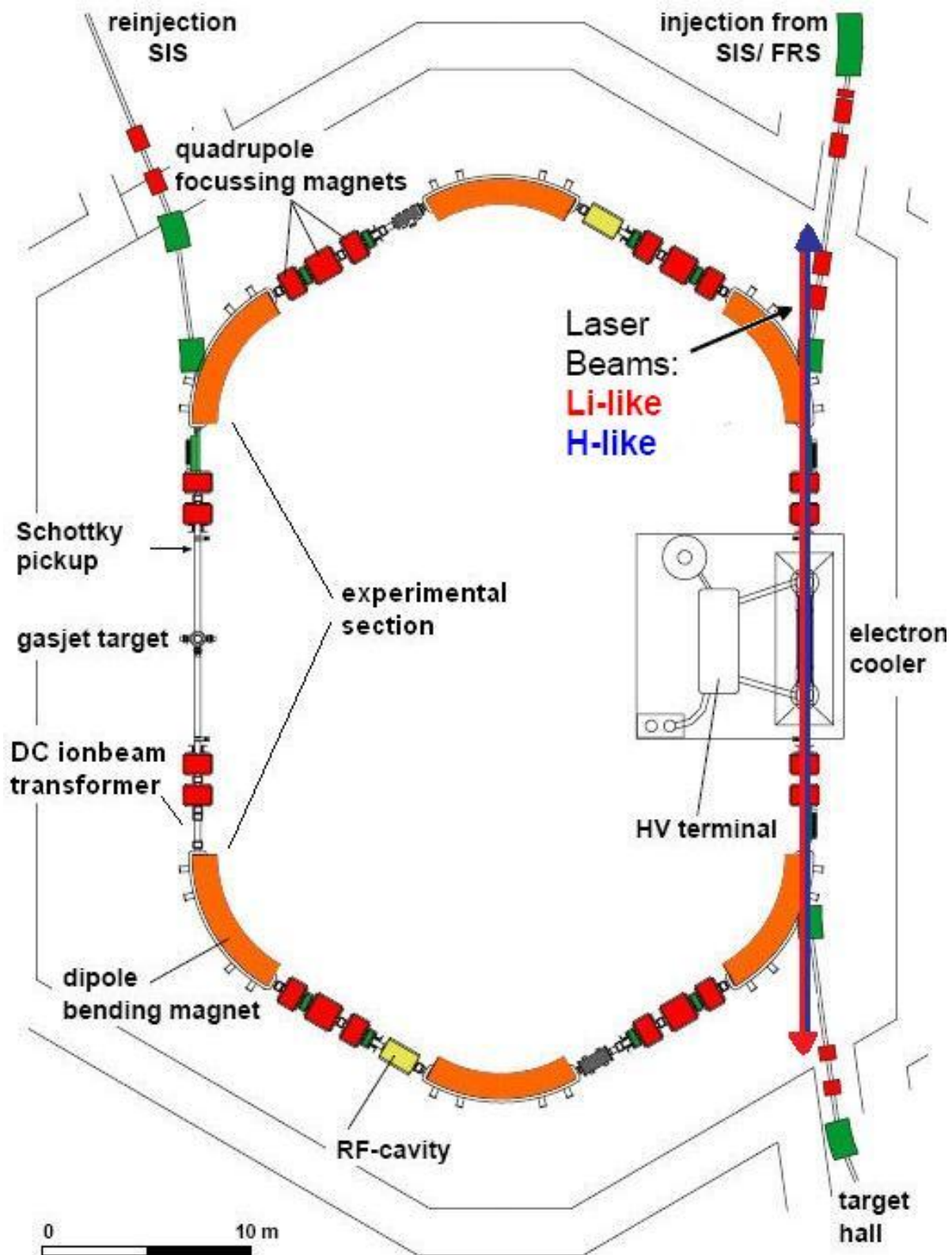
Figure 3.2.: Experimental Storage Ring (ESR). Image from [Nov08].

spectrum will be obtained from the difference of photon rates measured for the signal and the reference bunch (see Figure 3.3).

Each ion bunch extends between 5 and 10 metres and has a width of 15-18 mm FWHM. The number of ions contained in each bunch is 10^8 ions [Loc10b].
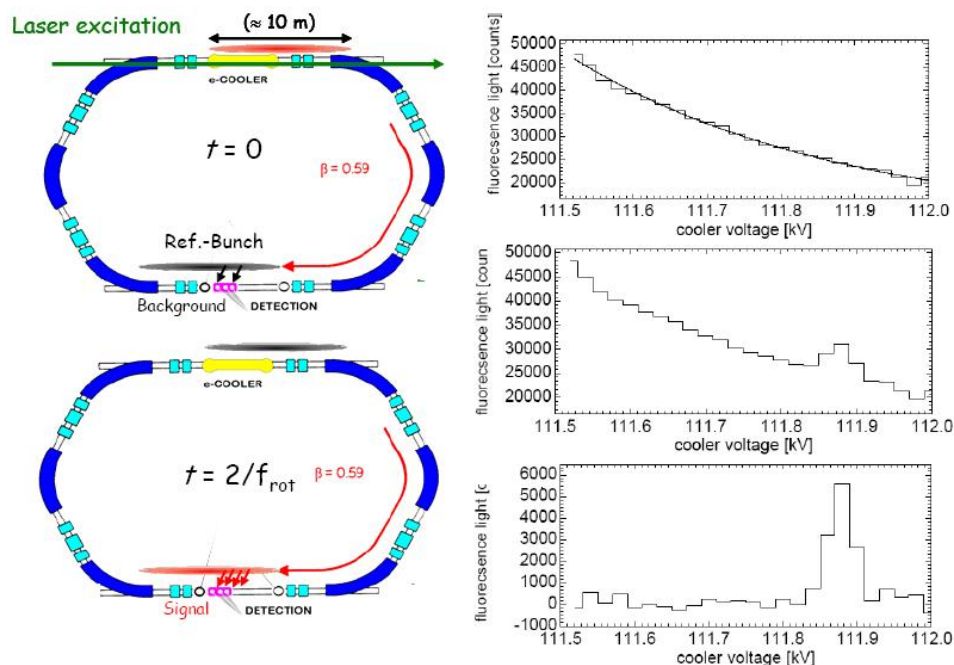

Figure 3.3.: Laser excitation of the bunch and signals obtained. Image from [Nör08].

As the H- and Li-like Bismuth shifted excitation wavelegths at 400 MeV/u are similar, the same laser system can be used. It consist of a frequency-doubled Nd:YAG laser ($\approx$500 mW at 532 nm) (see Figure 3.4) for pumping of a SpectraPhysics dye laser. This system was used in the last beam time and its power to excitate M1 transitions has already been proven.

3.2.1. SpecTrap experiment

The SpecTrap experiment is the next step for the HFS measurements. The precision of this facility is expected to be $\Delta\lambda/\lambda \approx 10^{-7}$ and it will allow to give a very accurate value of the hyperfine transition wavelength of the different highly charged ions [And10].

The way the ions take is the following (see Figure 3.5): Ions will be stored using the ESR and will be decelerated to 3 MeV/u energy. Then they are extracted in a fast-extraction mode as short ion bunches and go to a post decelerator that will slow them down till 6 keV/u energy. Finally, they're cooled by a Cooling Trap at 4 K, having a final energy of a few meV. When the ions are cooled, they're prepared to be used on experiments such SpecTrap [Hit10].

SpecTrap is a novel setup consisting of an ion transport beamline which guides the ions produced by the Hitrap facility to a Penning trap. The ions will be injected on a
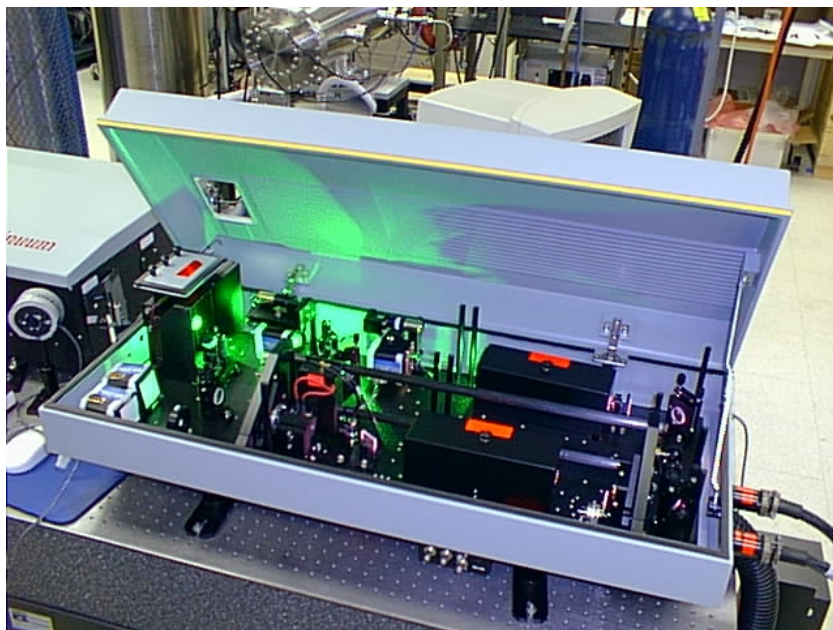
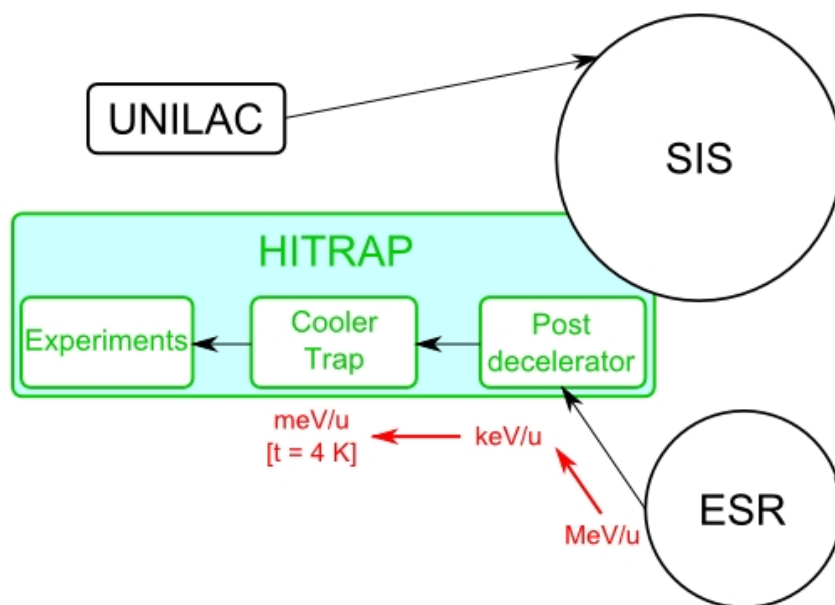Figure 3.4.: YAG laser with lid open working at 532 nm.

Figure 3.5.: Hitrap experiments [Hit10].

cylindrical trap and stored there by electric quadrupole and rotating dipole fields. The excitation is produced by a laser entering axially and the fluorescence light is detected in the radial direction, to minimize the background from scattered laser light. A picture of the SpecTrap setup can be found in Figure 3.6.
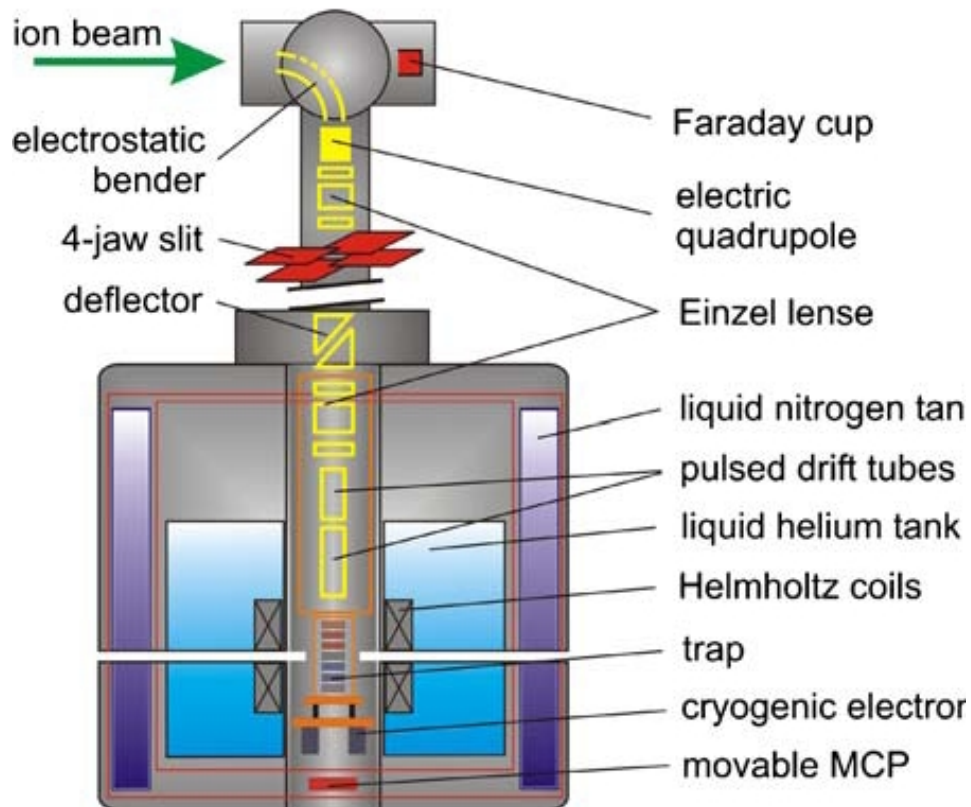

Figure 3.6.: Spectrap setup. Image from [And10].

In order to achieve the detection of the HFS wavelengths of $^{209}\text{Bi}^{80+}$, $^{209}\text{Bi}^{82+}$ and $^{207}\text{Pb}^{81+}$, suitable detector systems have to be developed. For the UV, the visible and the near infrared regime up to 1100 nm, suitable detectors have been identified and tested [Ham08b], [Ani10a], [Jöh10]. The detection system for the 1550 nm transition in $^{209}\text{Bi}^{80+}$ in SPECTRAP is still under study.

3.3. Detection systems

To detect the fluorescence photons emitted by the ions in measurements at the ESR an efficient detection system is needed. For the successful $^{209}\text{Bi}^{82+}$ [Kla94] and $^{207}\text{Pb}^{81+}$ [See99] HFS measurements and the failed $^{209}\text{Bi}^{80+}$ [Bor00], a detector system based on mirrors that reflect the photons emitted by the highly charged ions was used. After the failure of the Li-like Bismuth HFS measurement, a novel detection system consisting of two independent detectors was designed. The location of the detection systems on the

ESR can be seen on Figure 3.7. An analysis of the failure of the first detection system used and a brief introduction of the new setups [Ani10a] will be given in this section.
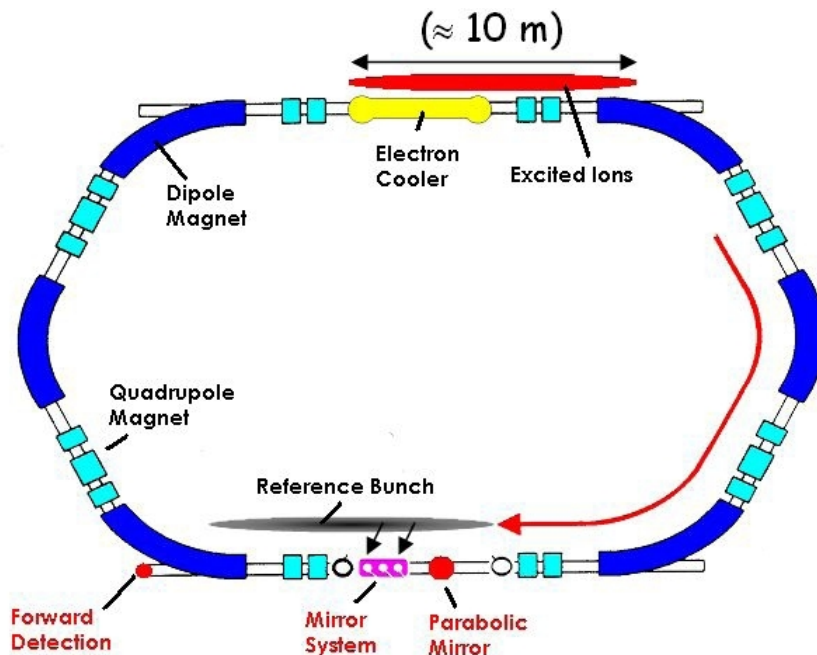

Figure 3.7.: Detector positions at the ESR [Nör07].

3.3.1. Mirror section

The name of the previous detection system used for the HFS measurments is *Mirror section* because it consist of ten identical mirror segments of 55 mm length on a 650 mm support structure. On the lower half, the conic mirrors form an angle of 15° with the horizontal. On the upper part there are also conical mirrors, but with a different Radius. Fluorescence photons collected by the mirrors have a chance to exit through one of three windows located in the upper half of the mirror section. Between the windows and the detectors there is a 130 mm conic light guide with 60 mm diameter in the window part and 50 mm diameter in the detector one. Between the detector and the light guide there is a longpass filter that cuts the wavelengths under 590 nm. The reflectivity of the mirror for the wavelengths of interest (between 640 nm and 900 nm for this section) is between 92% and 80%.

An analysis of the failure to detect single photons during the Li-like Bismuth measurements in 1999 and 2003 has been done by D.Anielski [Ani10a] and the conclusions are the following. The simulated signal rate for the 2003 experiment is $(14.9\pm0.2)s^{-1}$. To have results with a 3σ significance, one has to measure (57.4 ± 0.4)s per wavelength and for a 2σ significance, the measurement must take (25.5 ± 0.2)s. The problem on the last
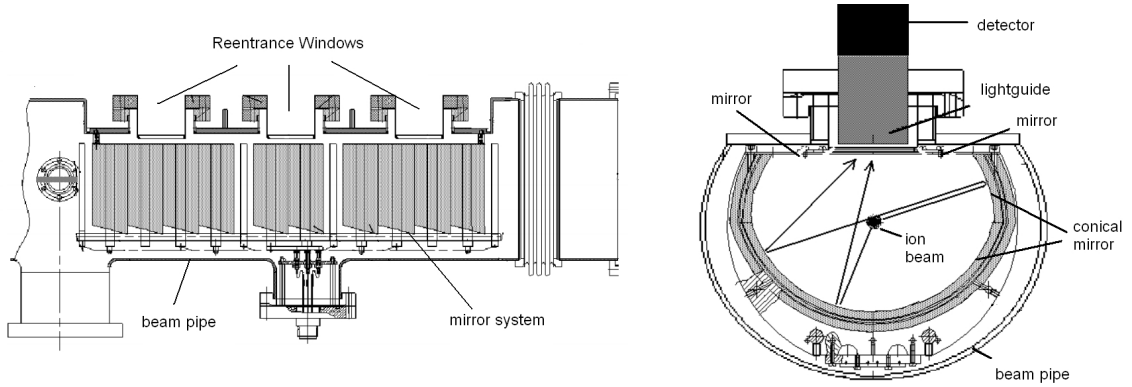
Figure 3.8.: Side view of the mirror section and transversal cut (right). The ten segments that reflect the ligth emitted by the ions can be seen on the side view and also the windows were the detectors are placed. On the transversal cut the setup with the ion beam and the detectors is shown [See99].

experiment was that the measurements took between 23 s and 10 s per wavelength, giving a significance under 2σ and therefore inconclusive results.

To investigate if the mirror section can be used for a successful Li-like Bi measurement in the future, without the need for a much longer beamtime, some simulations have been done in order to optimise the detection system. The proposed changes for this section are mainly a bigger window (72 mm instead of 60 mm) and an optimised light guide. The simulated signal rates for the old mirror section and the optimised one are presented in Table 3.1. There one works with two hypothesis: the conservative one with a 0% reflectivity of the beampipe and a normal quantum efficiency for the PMT R1017 and the optimistic one where a 25% reflectivity of the beampipe is considered and also a 1.4 times higher efficiency as a normal R1017 is included on the simulations for a selected detector. The background for all the situations as well as the needed measurement time per wavelength are also included.

	Signal/s^{-1}	Background/s^{-1}	Time/s
R = 0, QE = QE$_{R1017}$			
Mirror section	$9,0 \pm 0,4$	495 ± 5	$109,6 \pm 2,5$
Optimised mirror section	$10,8 \pm 0,4$	594 ± 6	$91,2 \pm 1,9$
R = 25%, QE = 1.4·QE$_{R1017}$			
Mirror section	$15,4 \pm 0,5$	626 ± 7	$47,6 \pm 0,9$
Optimised mirror section	$18,6 \pm 0,5$	756 ± 8	$39,4 \pm 0,7$

Table 3.1.: Signal rate, background and measurement time for the mirror section. Data from [Ani10a].

It is concluded that a reliable detection of the HFS transition in Li-like Bi is not possible with the mirror section without a substantial increase in beam time.
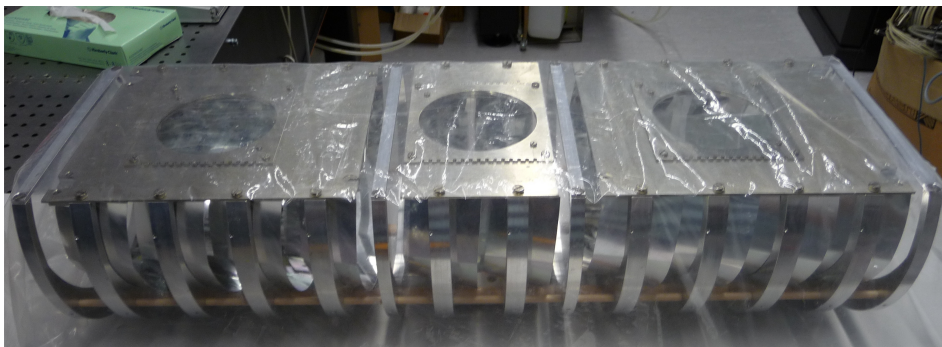
Figure 3.9.: Photo of the mirror section. The mentioned reentrance windows and also the ten conical mirror sections can be seen.

3.3.2. Parabolic mirror system

The parabolic mirror system is the main detector system for the final setup. It'll be mounted on a flange transversal to the beampipe. It consists of an Off-Axis parabolic mirror with a slit for the ions that collect the photons emitted at small angles. For more information see Chapter 4.

3.3.3. Forward direction system

In the forward direction a detector system can be placed. This won't be the main detector system but the one that would confirm the signal if it was found. As it will be placed on the ions direction, the photons coming from the experiment will be emitted with an angle close to 0°. For more information see Chapter 5.

4. Parabolic mirror system

The main detector system that will be used for the upcoming Li-like Bismuth experiment is presented in this chapter. A detailed description, the test done with the components and also the detector used in this setup will also be described.

The parabolic mirror system is the main detector system for the named experiment because it is the one expected to give the highest signal rate. Depending on the quantum efficiency of the PMT used and the reflectivity of the beampipe, a signal rate between 46 Hz and 86 Hz on a background between 378 Hz and 596 Hz can be achieved. The technical drawing of the parabolic mirror system can be found in Appendix A.

	Signal/s^{-1}	Back$_c$/s^{-1}	Back$_o$/s^{-1}	t_c/s	t_o/s
R = 0, QE = QE$_{R1017}$	46.3±0.5	378±9	279±8	3.2±0.1	2.3±0.1
R = 25%, QE = 1.4·QE$_{R1017}$	86.0±0.6	596±11	453±9	1.5±0.1	1.1±0.1

Table 4.1.: Signal rate, background and measurement time simulated for the parabolic mirror section. Subscript c is for the conservative case and o for the normal one. The first row correspond to a case without considering that the PMT R1017 is a selected one with a higher quantum efficiency as the normal ones and that the beampipe has a 0% of reflectivity [Ani10a].

4.1. Design

The parabolic mirror system came up due to the need of having a new detection system that enable a higher signal rate for the Li-like Bismuth experiment. The setup consists of an special DN 200 CF flange where a linear feedthrough with a 180 mm range of movement and a DN 100 CF window are mounted. The linear feedthrough moves a pure copper parabolic mirror with a central slit for the ionbeam. An Aluminum with a high reflectivity coating cone can be found on the vacuum side of the window in order to collect more photons.

The vacuum parts are specified with a leak rate below 1×10^{-10} mbar l/s. All the vacuum relevant parts can be heated to 350°C. The rest of the components may reach 230°C [Ani10b].

To be used together with the parabolic mirror system there is an optical detection system consisting of a Hamamatsu R1017 *PMT* and a *PMT cooler* (PR-TE104RF). The PMT cooler is attached to the DN 100 CF window with an *adaptor*. Coupled onto the window with optical grease there is a *light guide* and between the light guide and the PMT there

are a Linos OG 590 Pale-red and a Linos NIR-Blocking Filter CALFLEX X *filters* (See Figure 4.1). To watch a picture of the adaptor see Section 4.3.1.
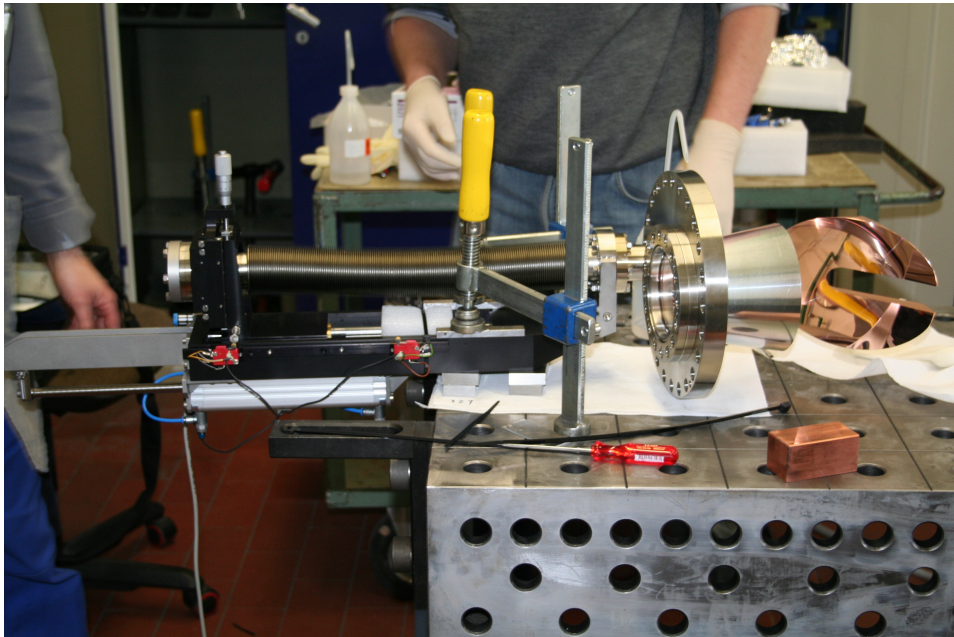

Figure 4.1.: Photo of the parabolic mirror system standing on a bench in Münster workshop.

4.2. Mechanical mirror setup

4.2.1. Linear feedthrough

The linear feedthrough is an ultrahigh vacuum manipulator system that allows for a 180 mm range of movement. The feedthrough is based on the model KPM 12-200 from VAB company [Vab10].

The movement is achieved by a pneumatic cylinder, driven by air pressure. The positioning of the mirror can be transversally adjusted by ± 12.5 mm using two micrometer screws attached on the manipulator. The technical specification can be found in Appendix A.1

The first test measurements performed with this part of the setup were done in Münster. There the linear feedthrough was mounted on the special DN 200 CF flange that had been mounted on a UHV chamber. The main component of this chamber is a 2 meter long stainless steel tube with a diameter of 30 cm. A pressure of 10^{-10} mbar can be achieved thanks to the two pumps used: A primary scroll-pump with a pumping power of 15 m^3/h and a turbomolecular pump with a velocity from 15 to 240 l/s [Rei07]. In the test measurements a 10^{-8} mbar pressure was reached without outbaking of the equipment.
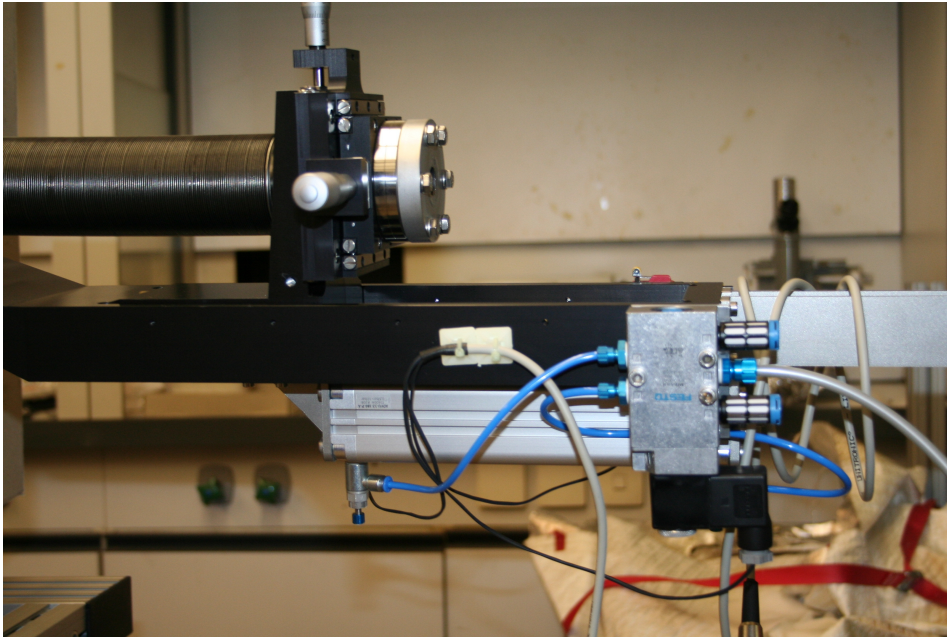
Figure 4.2.: Linear feedthrough on the test bench in Münster.

A leak test of the parts was successfully performed and the linear feedthrough was left attached to the DN 200 CF. Some problems arose regarding the movement of the pneumatic cylinder. The air pressure valve velocity was adjusted, but with a fast or slow movement, the mirror always reached its endpoing shaking up and down. That is a potential problem because the mirror can then interfere with the ion beam. The solution found was to use ball-bearing grease on the linear feedthrough in allow for a smooth movement. This ball-bearing grease must be removed before heating of the vacuum parts.

4.2.2. Parabolic mirror

The mirror used is an Off-Axis-Parabolic mirror made of OFHC-Copper with a central slit for the ions. The width of the slit is w = 30 mm corresponding to ca. 3.5 times the standard deviation σ of the beam profile [Ani10a].
In order not to loose the emitted photons, a high reflectivity coefficient of the mirror is needed. The reflectivity at the relevant wavelengths is specified to be larger than 95% (see Figure 4.3).
The equation that describes the mirror surface is given by the equation of a paraboloid centered on the origin in three dimensions:

$$z(x, y) = \frac{x^2 + y^2}{a^2}; \quad \text{and} \quad f = \frac{a^2}{4} \tag{4.1}$$

Here f is the focal point of the paraboloid. As photons are reflected by an angle ca. 90°, the focal length is given by (see Figure 4.4):
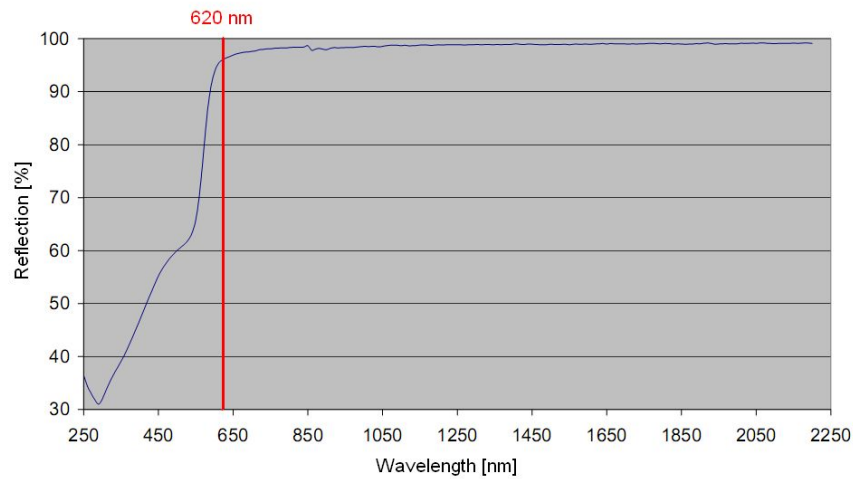
Figure 4.3.: Reflectivity curve of the OFHC-Copper parabolic mirror given by Kugler Company [Kug10].

$$f' = 2f = \frac{a^2}{2} \tag{4.2}$$

Figure 4.4.: Parabola scheme [Ani10a].

The simulations have shown that the optimal focal length for the paraboloid is f' = 200 mm (see Figure 4.5). Then, the parameter a will take the value $a = 20$ mm.

The parabolic mirror was first delivered to the institute without polish in order to do some test measurements and undergo heat treatment before receiving the polished

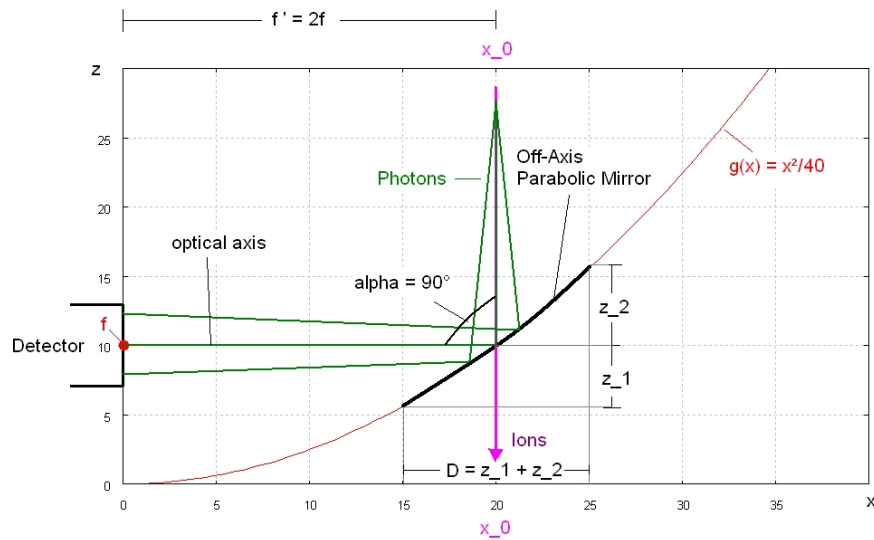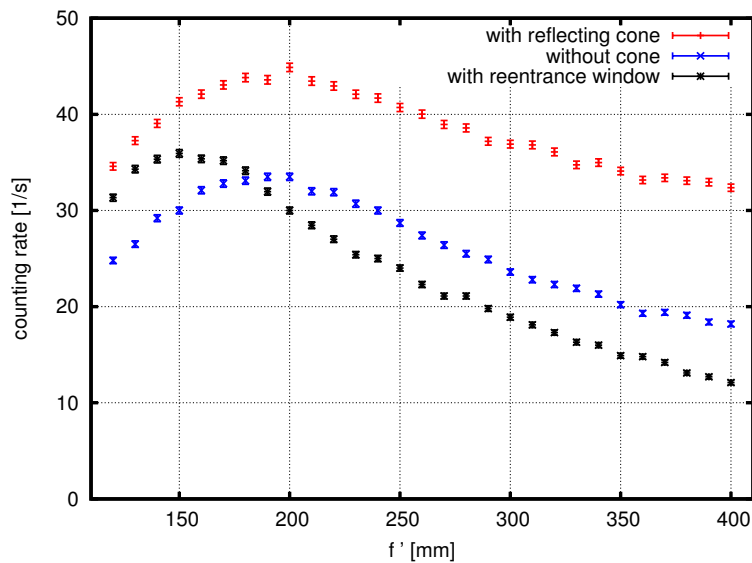Figure 4.5.: Counting rate as a function of the focal length. The focal length that gives the highest counting rate is the option chosen.

surface. With this process further changes of the mirror shape during later bake-out cycles are tried to be avoided. The weight of the unpolished mirror was (3090 ± 1)g. The heat treatment performed in the UHV chamber described in section 4.2.1 at a temperature of 350 °C. The temperature was held for eight hours and then the mirror cooled down.

Another test done on the mirror was checking of the shape. In order to do it, a Stiefelmayer measurement table Model "System C" (see more details in [Jöh07]) was used. The procedure followed to measure the shape is described in Appendix C.

After that, the mirror was polished by LT-Ultra Precision Technology and cleaned following the procedure described in [Ani10b].
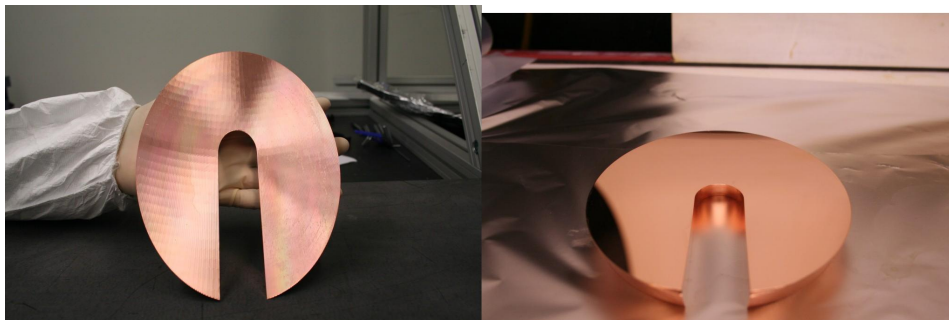

Figure 4.6.: Parabolic mirror before (left) and after the polish (right).

On Figure 4.6 the difference between the mirror surface before and after polishing can be

seen. After the surface cleaning, a measurement of the reflectivity was performed. The reflectivity measured using a 635 nm Laser Pointer and a Laser Powermeter (Coherent, FieldMaxII-TO) was (97.1±0.9)%. This result is consistent with the reflectivity>95% specified by the manufacturer on Figure 4.3.

4.2.3. Aluminum Cone

In order to achieve a higher signal rate (see Figure 4.5) an aluminum cone will be used in the setup. This cone has been made of MIRO-2 material from the Alanod company [Ala10] and is installed on the vacuum side of the window. The datasheet can be seen on Appendix A.3.

The reflectivity of the cone material was measured following the same procedure as described for the parabolic mirror. A possible change of the material reflectivity before and after the heating up was also measured. To do it, a piece of MIRO-2 was heated in the UHV chamber until 350°C temperature. The results of the reflectivity measurements can be found in Table 4.2.

MIRO-2 material	Reflectivity/%
After heating	80.9±0.9
Before heating	89.4±0.9

Table 4.2.: Reflectivity of the cone material before and after heating at 350 ˚C.

The change in the reflectivity of the material may partly be due to a change of the shape of the material. After heating, the piece of MIRO-2 exhibited a slight curvature. The result is a higher light diffusion, and therefore an apparent lower reflectivity. The reflectivity measured for the material before the heating up is smaller than the one given by the company, which is larger than 95% [Ani10b].

4.2.4. Window and flanges

In the complete system there are three different flanges and one window. There is one special DN 200 CF flange where the cone is attached on the vacuum side and also the window and the linear feedtrough. At the outer end of the linear feedthrough there is a special DN 40 CF where the rod holding the mirror is attached. The material of the components is stainless steal 1.4306. The window is mounted in a DN 100 CF flange made of *Kodialglas*.

In Appendix A.4 the window datasheet can be found. The expected transmission coefficient for the window is specified to be larger than 90% for the wavelengths of interest. This coefficient has been measured using a red laser pointer and a laser powermeter and is close to 99% for the forward direction. An angle dependent measurement has also been performedand shows, that the transmission stays above 90% for incidente angles up to 45˚. The results are shown on Figure 4.8.
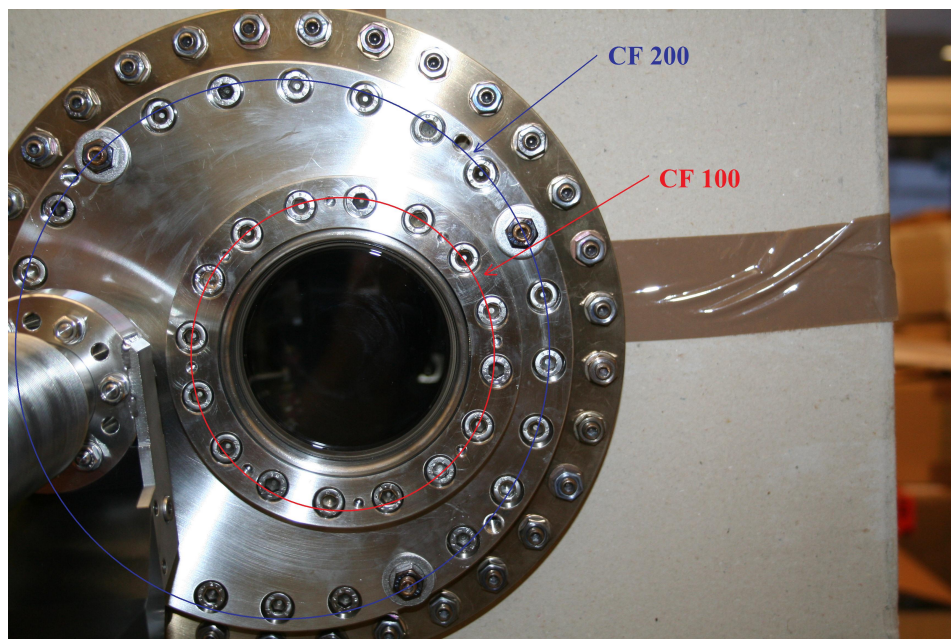
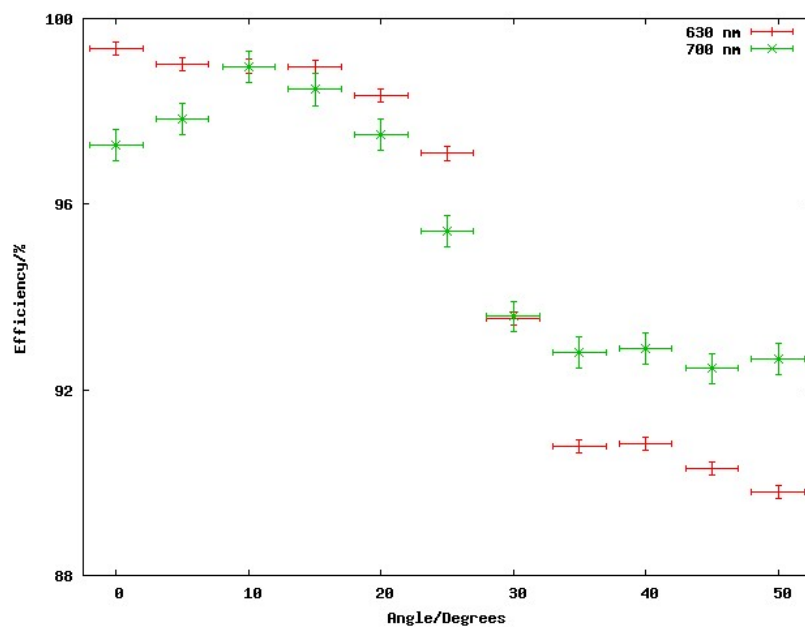Figure 4.7.: Special DN 200 CF flange and DN 100 CF window.

Figure 4.8.: Transmission coefficient as a function of the incident angle for the Kodialglas
window. Two different LEDs were used in order to see the differences of the
transmission coefficient for different wavelengths.

4.3. Photomultiplier setup

The following section describes all the parts of the detector system related to the PMT, as well as a description of the test measurements done in order to determine the quantum efficiency and other characteristics of the detector.

4.3.1. Cooling system and optical adaptor

The cooling system consist of a cooler (PR-TE104RF) to cool down the PMT to reduce the dark count rate. The cooler uses a thermoelectric effect given by Peltier elements. In order to get rid of the heat generated during this process, a water cooling circuit is connected to the cooler. The temperature difference that the cooler can achieve between the PMT and the water temperature is 40°C.

The optical adaptor system has been specially designed for this setup. The requirements that it is has to fulfill are the following:

- There shouldn't be air gaps between the window, the lightguide and the photomultiplier. Without air gaps, there is no significant change in index of refraction change. This avoids partial reflections and therefore the loss of photons.

- It must be light tight. Any environmental light that can enter the system disturbs the measurements and increases the dark count rate of the system.

- It has to contain a light guide whose conical part has a length of 160 mm, according to the simulations and also a filter in order to get rid of wavelengths outside of the range of interest.

All these requirements are fulfilled by a stainless steal adaptor with a flexible bellow that allows an adjustment of the components. Figure 4.9 shows a photo and a cross sectional view of the optical adaptor. The front part of the bellow is in charge of a tight fit between the light guide and the window. The other end, surrounding the cooling house, adjusts the PMT photocathode (with the filter attached to it) and the light guide. Between all the components optical grease is used, in order to avoid air gaps as mentioned before. The adaptor is attached to the CF 100 window by eight screws situated in the flange.

4.3.2. Filters and light guide

Short and long wavelengths photons need to be cut by a filter to reduce noise coming from background photons. It has been shown in [Ani10a] that the wavelengths of interest are on the range between 640 nm and 700 nm. A longpass and a shortpass filter have to be used in order to get rid of as much background photons as possible. The shortpass filter selected is a Linos NIR-Blocking Filter CALFLEX X and the longpass filter is a Linos OG 590 Pale-red filter [Lin10] (the transmission plots of the filters can be seen on Figure 4.10).
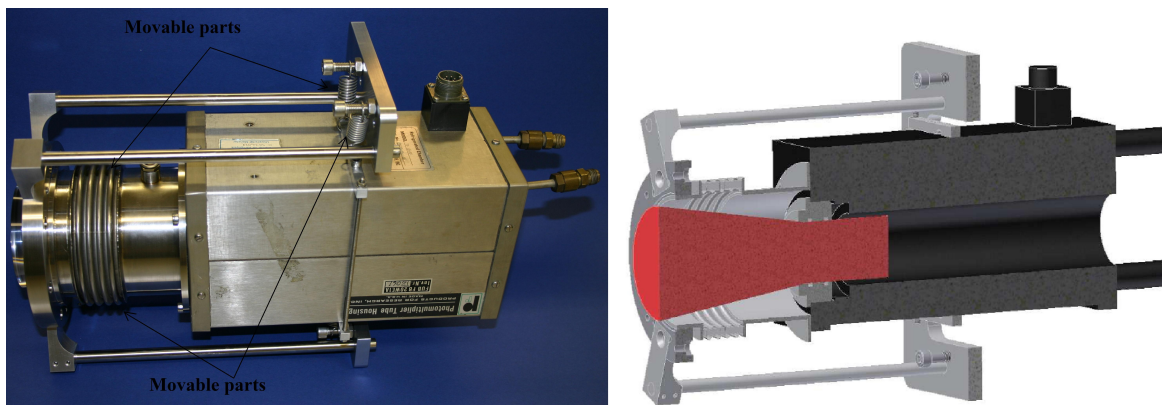
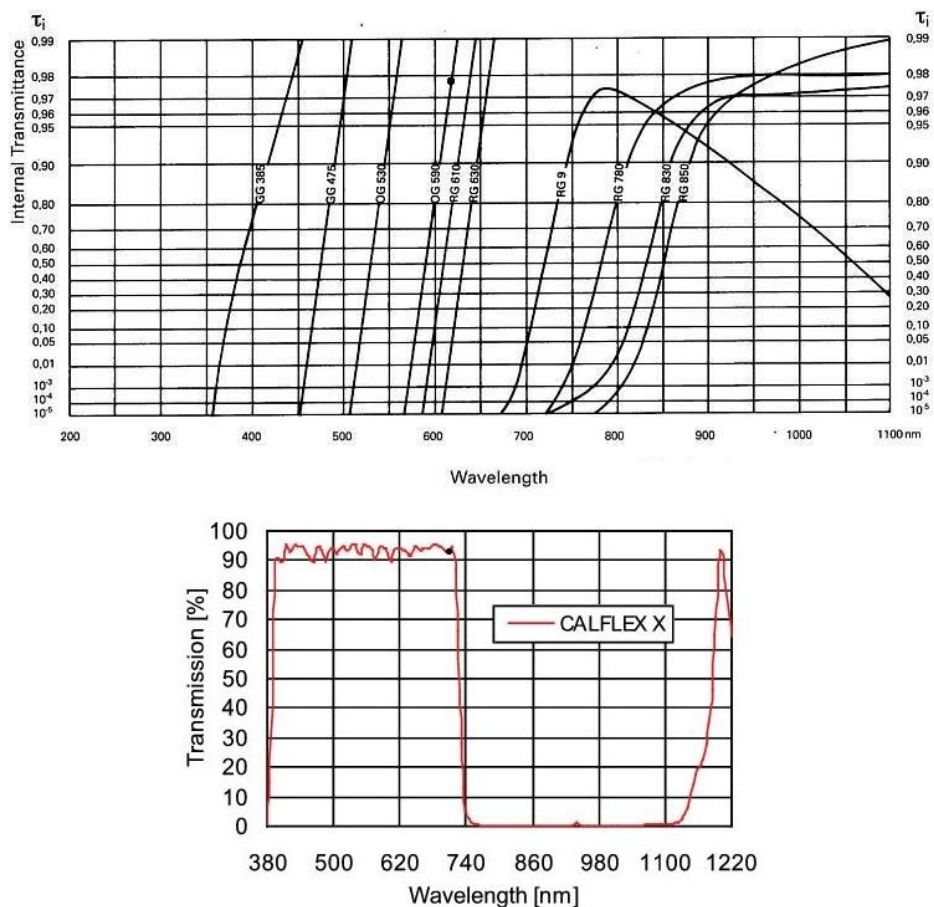Figure 4.9.: Movable parts (left) and longitudinal view of the adaptor system (right).

Figure 4.10.: Longpass and shortpass filter datasheet. As a result of the use of these filters there is a bandpass filter with a transmitance >90% on the region between 620 nm and 700 nm.

The light guide is an optical element that works with the principle of total reflection. Light entering under small angles is reflected without refraction by the light guide walls and is efficiently guided through the system. The optimal height of the conical part of the guide is 160 mm, according to the maximum efficiency obtained in the simulations [Ani10a]. On the cilindrical part of the guide a stainless steal corona is attached in order to screw the light guide into the cooling house. The base of the cone has a 86 mm diameter according to the effective diameter of the window. The smaller part of the cone has a 46 mm diameter according to the PMT photocathode diameter. A photo of the light guide and the filters can be found in Figure 4.11.
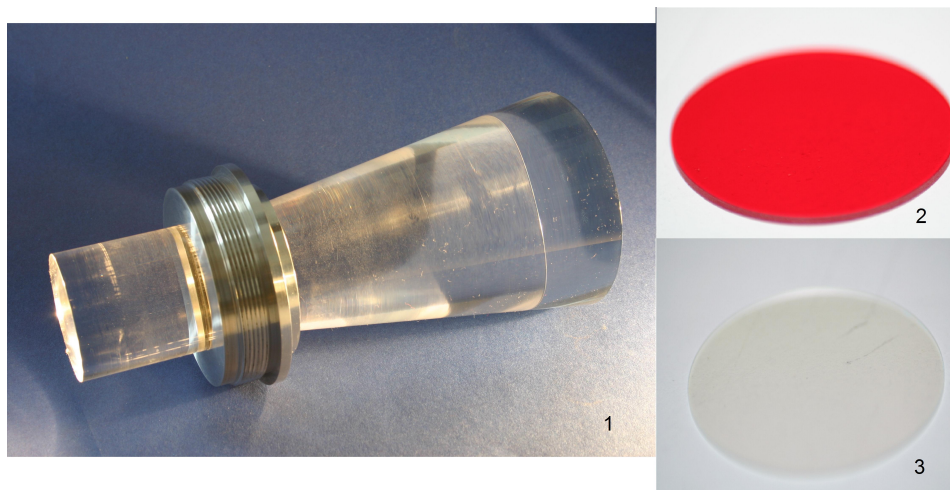
Figure 4.11.: 1.Light guide. 2.OG 590 Pale-red filter. 3. NIR-Blocking Filter.

The effect of the light guide on the PMT temperature was also determined. The dark count rate with light guide was $(113.8\pm1.1)\text{s}^{-1}$, when the typical results for this detector are between 80 s^{-1} and 100 s^{-1}. Using the same laser pointer and power meter as were described in Section 4.2.2, the transmission coefficient of the light guide and the filter were also measured. The results of this measurement are reported in Table 4.3.

	Transmission coefficient/%
Light guide	90.8±0.8
Filter	95.8±0.8
Light guide + Filter	83.3±0.8

Table 4.3.: Transmission coefficients of the filter and light guide at a wavelength of 635 nm.

4.3.3. Detector: PMT R1017

The detector used in this setup is a selected Hamamatsu PMT R1017 [Ham10]. The selected Photomultiplier tube has a higher quantum efficiency compare to the standard R1017s. To determine the optimal electronic parameters (e.g. HV, threshold) for the detector, some test measurements were performed.

The typical PMT R1017 dark count is between 80 s^{-1} and 100 s^{-1}. The amplitude of the signals coming from the detector lies between 5 mV and 60 mV on a 2 mV background. For a reliable discrimination the signals must be amplified. Due to the low signal noise to ratio (SNR) for the smaller signals, one can loose some signals if the discriminator level is too high or measure increased noise if the discriminator level is too low. Therefore, the discriminator level needs to be set up as accurate as possible. The small SNR is due to the relatively low gain of the PMT of $4.3 \cdot 10^5$.
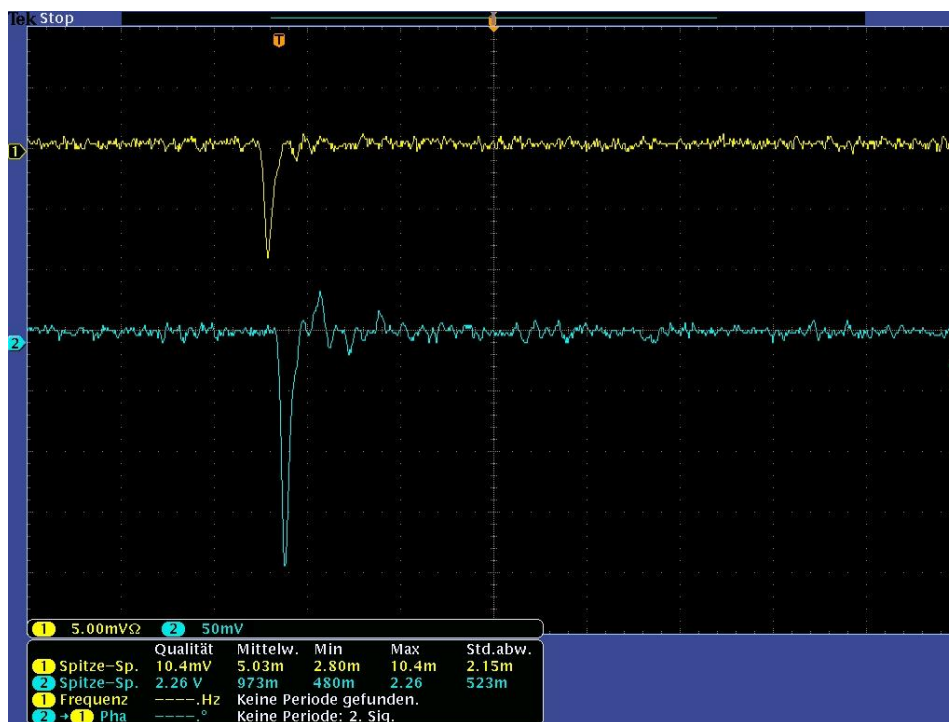
Figure 4.12.: PMT R1017 signals. Upper signal: direct output. Lower signal: Amplified output (amplitude = 200 mV).

In order to calculate the cooling time needed for the PMT to work in optimal conditions, the dark count rate as a function of the cooling time was measured. This measurement was done at the ESR with the cooling house attached to the window in order to reproduce the conditions of the real experiment. Cooling water (with 8°C temperature) supplied by a chiller was also used in order to achieve a lower temperature of the PMT. The results are shown on Figure 4.13.

Figure 4.13.: Dark count rate as a function of the temperature for the PMT R1017. The dark count rate becomes stable after a period of 2 hours. This means that this is the minimum cooling time needed to achieve an optimal operation of the PMT.
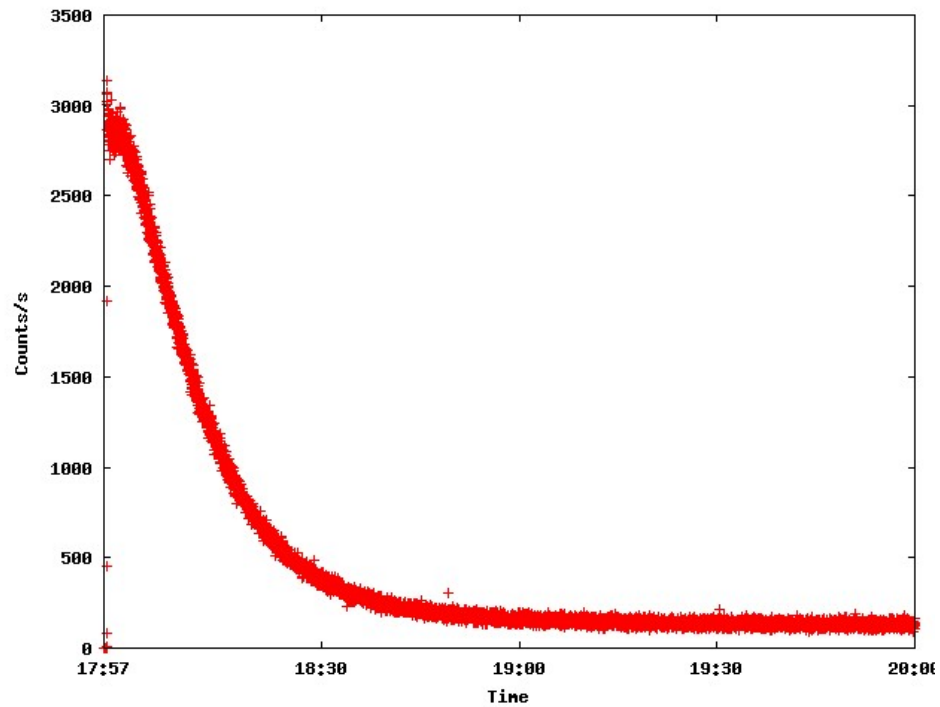
Single photon plateau

In order to determine the optimum PMT bias voltage, the single photon plateau must be determined. To do this, the PMT supply voltage is increased while the discriminator level is kept constant, then the output pulses are counted. The plateau region is reached when the count rate the count rate stays constant when the bias voltage is increased. If this region doesn't exist, the operating bias voltage for the PMT has to be set to a value corresponding to the region where the slope is smaller. The results are shown on Figure 4.14.

The region where the count rate becomes constant cannot be clearly determined, so the supply voltage of the PMT is set on the region where the slope is smallest:

$$V_{ideal}(R1017) = -1300V$$

The maximum supply voltage given in the R1017 datasheet is 1500 V, so the voltage that has to be applied to the PMT is far away from the dangerous region.
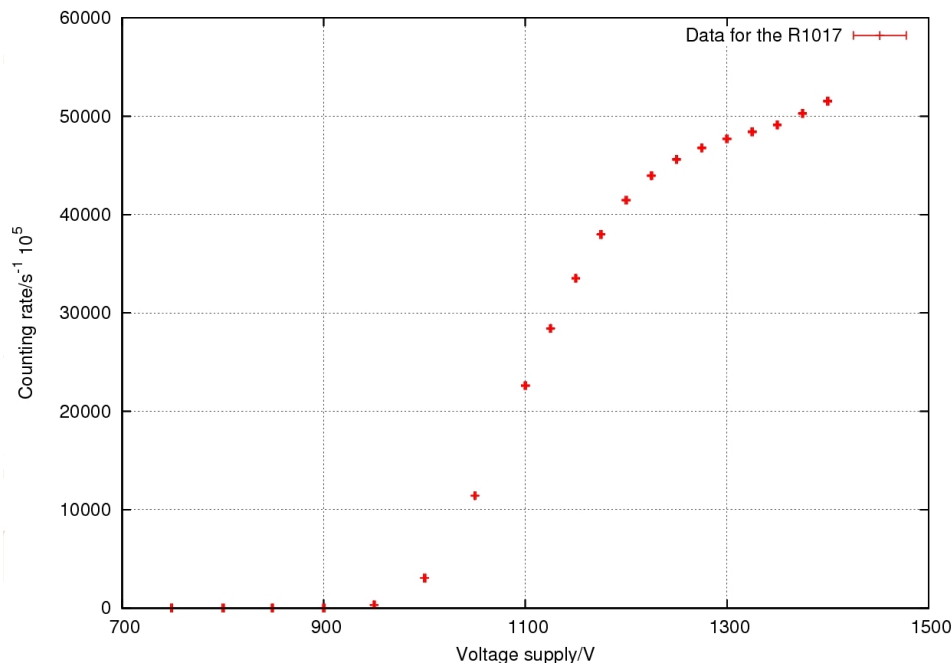
Figure 4.14.: Single photon plateau for the PMT R1017.

Quantum Efficiency of R1017

In order to measure the Quantum Efficiency of the PMTs that will be used with the parabolic mirror setup and at an additional ESR exit window in forward direction (see Chapter 5), a comparison with the Perkin Elmer Channelphotomultiplier (CPM) 1993P [Per10] has been performed. CPMs have a photocathode like PMTs. After the electron is emitted from the cathode, it passes through a narrow semi-conductive curved channel. When the electron hits the surface of the channel, an avalanche effect with a high gain (on the 10^8 order for the CPMs used) is produced. Due to the high gain, CPMs are well suited for single photon counting and have a lower dark count rate as PMTs [Per05].

The quantum efficiency of the 1993P CPM at 640 nm is 4% (see Appendix D.3.2) and the dark count rate at room temperature is between 5 s^{-1} and 10 s^{-1}.

The procedure to do the measuremens is the following: An LED [1] is placed in a black box and excited by a function generator (Tektronix AFG 3102). The signal coming from the function generator has the following characteristics: frequency 50 kHz, leading and trailing edge 5 ns, width 20 ns and a variable amplitude. The CPM signal is duplicated by a Fan In - Fan Out (C.A.E.N. Mod. N625). Then, one of the signals goes to a Discriminator (C.A.E.N. Mod. N843) and the other one to an Oscilloscope (Tektronix TDS 3054B). The discriminator has two outputs, one of them goes to the Oscilloscope and the other one to a Counter (C.A.E.N. Mod N1145). The high voltage is applied to the PMT by a High Voltage Power Supply (ISEG NHQ 226L) See Figure 4.15.

For the PMT, the procedure is almost the same, but in this case the signal coming from

---

[1]The different LEDs used during the test measurements are the following: (Siemens LS 5469-EH, $\lambda_{peak} = 630$ nm), (Kingbright L-13HD, $\lambda_{peak} = 700$ nm), (Multicomp OFL-5102, $\lambda_{peak} = 940$ nm).

the PMT is first amplified by an Amplifier (C.A.E.N. Mod N979) and then goes to the Fan In - Fan Out as for the previous detector. The scheme can be seen on Figure 4.16.
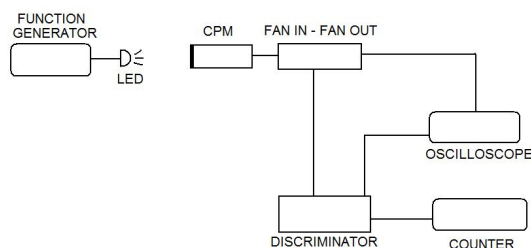
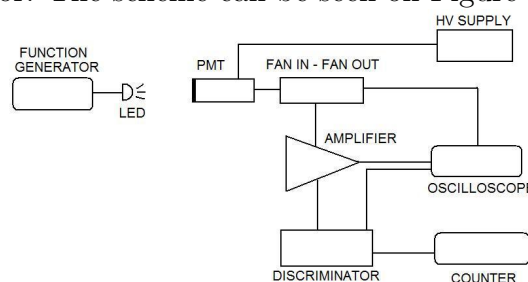

Figure 4.15.: CPM setup.   Figure 4.16.: PMT setup.

In order to have the same amount of light arriving at each photocathode, a black card with a central hole was placed as an aperture in front of the detectors. Placing this card at the same distance in all the experiments ensures the same solid angle and therefore the same quantity of photons arriving at the photocathodes.

- $\lambda = 630$ **nm**

    First of all, a 630 nm LED was used in order to obtain an estimate of the quantum efficiency at the wavelengths of interest. The LED pulse used for this experiment had an amplitude of 619 mV. The count rates obtained for this experiment are shown on Table 4.4.

CPM 1993P			
	Counts	Time/s	Counts/s^{-1}
Dark	1509	200	7.55±0.19
Signal	39348	200	196.7±1.0
PMT R1017			
	Counts	Time/s	Counts/s^{-1}
Dark	13180	100	131.8±1.1
Signal	53294	100	532.9±2.3

Table 4.4.: Counting rates using a $\lambda = 630$ nm LED.

$$\text{Counts-Dark (CPM)} = (189.7 \pm 2.0)\text{Hz}$$

$$\text{Counts-Dark (PMT R1017)} = (401.1 \pm 2.5)\text{Hz}$$

The Quantum efficiency of the PMT R1017 at 630 nm is (2.11±0.03) times higher than the quantum efficiency of the CPM. If a quantum efficiency of 4% is supposed for the CPM 1993P at 630 nm with a 0.5% uncertainty (given by the manufacturer), then Q.E. of the PMT R1017 at 630 nm can be estimated to be (8.4±1.1)%, a result lower as the one expected for a selected detector (see Appendix D.1.2).

- **$\lambda = 700$ nm**

  In this case the LED used had a peak wavelength of 700 nm and the signal coming from the oscilloscope has an amplitude of 2 V.

CPM 1993P			
	Counts	Time/s	Counts/s^{-1}
Dark	1514	200	7.57±0.19
Signal	3380	200	16.9±0.3
PMT R1017			
	Counts	Time/s	Counts/s^{-1}
Dark	12238	100	122.4±1.1
Signal	15129	100	151.3±1.2

Table 4.5.: Counting rates using a $\lambda = 700$ nm LED.

$$\text{Counts-Dark (CPM)} = (9.4 \pm 0.7)\text{Hz}$$
$$\text{Counts-Dark (PMT R943-02)} = (28.9 \pm 1.6)\text{Hz}$$

The quantum efficiency of the PMT is (3.1±0.3) times higher than the quantum efficiency of the CPM at a 700 nm wavelength. If the CPM quantum efficiency at 700 nm is 1%, then the quantum efficiency of the PMT R1017 at 700 nm is (3.1±1.6)%. Again lower as the one expected from the datasheet in Appendix D.1.2.

- **$\lambda = 940$ nm**

  For the 940 nm LED a 2 V signal was used in order to excite it. At this wavelength the dark count rate cannot be distinguished from the signal rate in any of the detectors. The expected quantum efficiency for both detectors is under 0.1 % (see Appendix D.1.2).

CPM 1993P			
	Counts	Time/s	Counts/s^{-1}
Dark	712	100	7.1±0.3
Signal	750	100	7.5±0.3
PMT R943-02			
	Counts	Time/s	Counts/s^{-1}
Dark	10312	100	103.1±1.0
Signal	10564	100	105.6±1.0

Table 4.6.: Counting rates using a $\lambda = 940$ nm LED.

5. Forward detection system

The forward detection system acts, like the mirror section, as a secondary detection system in the final setup. It is placed in forward direction on an exit window near one of the ESR dipoles (see Figure 5.1). The system can be used for the diagnosis of forward peaked background photons and to confirm a resonance signal found by the parabolic mirror system. The signal rate simulated for this section is $S = (2.1\pm0.1)s^{-1}$ on a background of $b = (29.7\pm1.4)s^{-1}$ [Ani10a]. The measurement time needed to confirm a signal with 3σ significance is $t = (119.4\pm5.9)s$. Due to this measurement time, which is 37 times higher than the estimated conservative measuring time with the parabolic mirror system, the forward detection system can't be used as the main detector. The photons that can be detected in this section are emitted at a distance of at least 2.2 m from the exit window under small angles to the beam axis. This results in nearly collimated photons, which can be focused onto the detector with a lens. The detector system will directly be mounted onto the window.
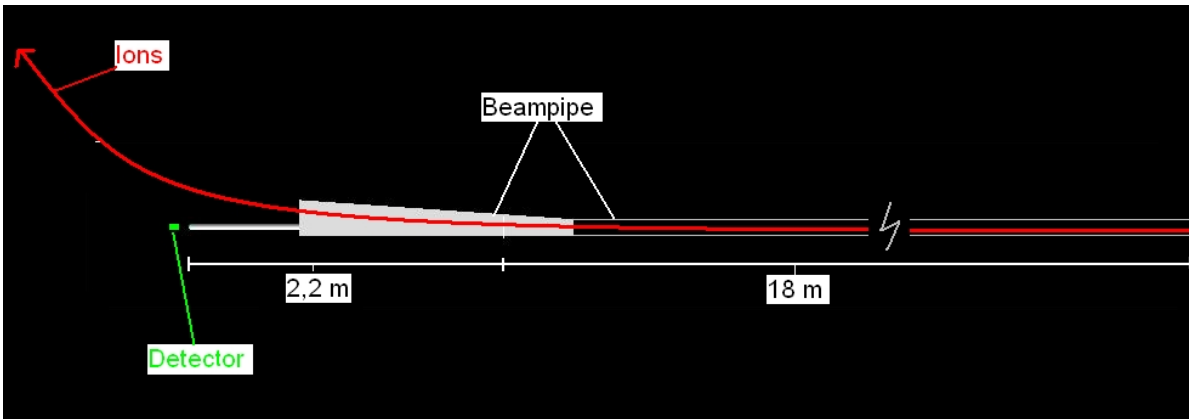
Figure 5.1.: Scheme of the forward direction section.

5.1. Design

The detector system will be mounted on a DN 100 CF special flange 316LN with a 89 mm window diameter. The specifications of the flange can be found in Appendix B.1. The detector system is attached to the window by a stainless steal adaptor that keeps the system light tight. A light guide is attached directly to the window. After the light guide a lens with a focal length f' = 150 mm is used. There is a gap between

the lense and two optical filters, that are coupled to the PMT with optical grease. The photocathode of the PMT is positioned in the front focal point of the lens.
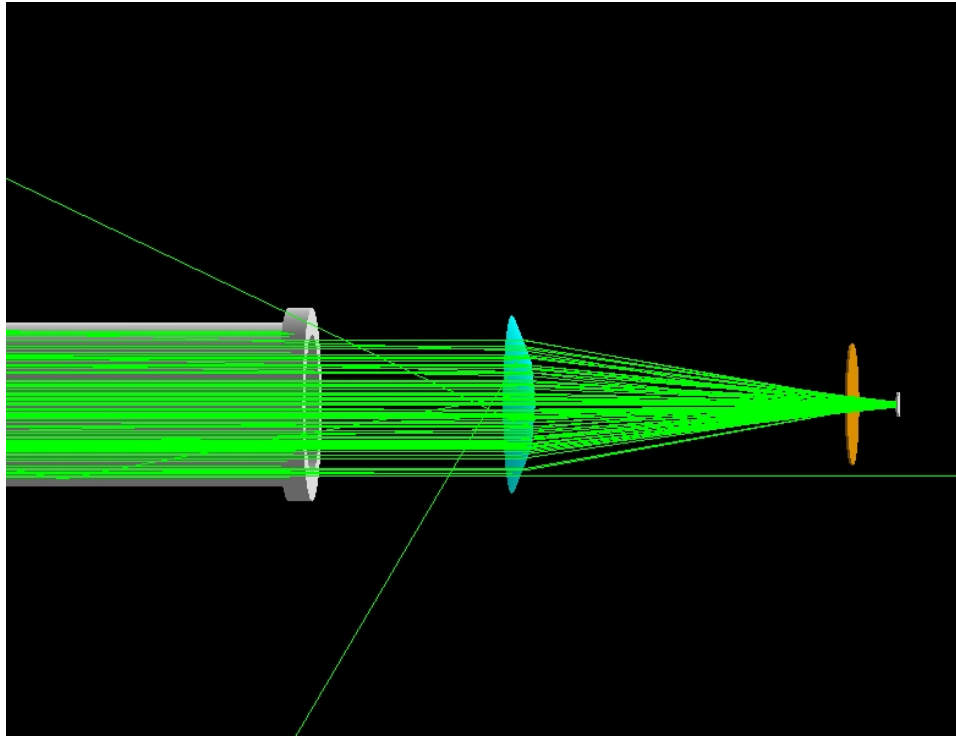

Figure 5.2.: Image of the forward direction simulation. The green lines are photon trajectories, the light blue semicircle is the lens, the orange circle is the PMT window and the grey one is the PMT photocathode. The light guide isn't included on the simulation. It can be seen that all the photons that go through the pipe are focused by the lens and are collected by the photocathode.

5.2. Mechanical setup

5.2.1. Light guide, Lens and filters

The material of the light guide is Plexiglas as is the case in the parabolic mirror section. The height of the conical part of the light guide is 70 mm. The diameter of the side attached to the window is 70.5 mm and the diameter of the side in contact with the lens is 75 mm.

The lens is a LA 1002 N-BK7 Plano-Convex Uncoated from Thorlabs [Tho10]. The lens diameter is $\varnothing = 75$ mm and the focal length f = 150 mm. Additional parameters can be found in Table 5.1.
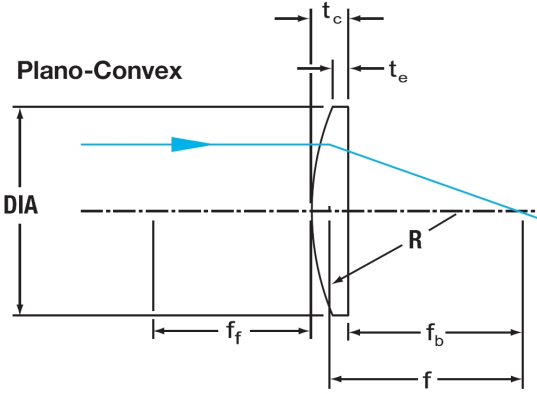
	Measure/mm
DIA	75.0
f	150.0
f_f	150.0
R	77.3
t_c	12.7
t_b	3.0
f_b	141.6

Table 5.1.: Lens parameters.

Figure 5.3.: Lens scheme.

The filters used for the forward PMT are of the same type as the ones used for the parabolic mirror system. The photons to be detected have emission angles close to 0°, so the wavelengths detected are close to 640 nm and the filter range is also valid here.

5.2.2. Cooling system and adaptor

The cooling system used for this detector consist of a PMT cooler (TE-210RF) that can reach a temperature difference between cooling water and the detector of 60°. The cooling housing used here is bigger as the one in the parabolic mirror system. It couldn't be used there due to the lack of space at that setup. This cooling housing also uses a Peltier-element where the heat transfer is done by a cooling water circuit.

The time to reach the operating temperature has been determined by measuring the dark count rate of the PMT as a function of the cooling time (see Figure 5.4). As it can be seen, the time needed to reach the optimal operation of the PMT is larger than in the PMT R1017 case. It can be explained because the temperature difference between the cooling water and the detector reached for the TE-210RF PMT cooler is bigger than the one reached for the PR-TE104RF cooler, used in the parabolic mirror setup.

The adaptor that will be used on this section is similar to the one used on the parabolic mirror setup. At the moment of writing this thesis it hasn't been constructed yet, but the technical drawings can be seen on Appendix B.2.

5.2.3. Detector: PMT R943-02

The PMT R943-02 is a Photomultiplier tube with a square photocathode with a 10×10 mm effective area. The photocathode is mounted at a distance of 19 mm from the entrance window inside the PMT (for more details see Appendix D.2.2). The gain of the PMT is $5 \cdot 10^5$ and the typical dark count rate at -20°C is 20 s^{-1}.

The signal amplitudes of the photomultiplier are between 5 mV and 60 mV so they must be amplified before they are discriminated and counted. Due to the low signal amplitude coming from the PMT, the discriminator level has to be set close to the noise level. The discriminator output provides a logical NIM signal if an incoming signal has a higher
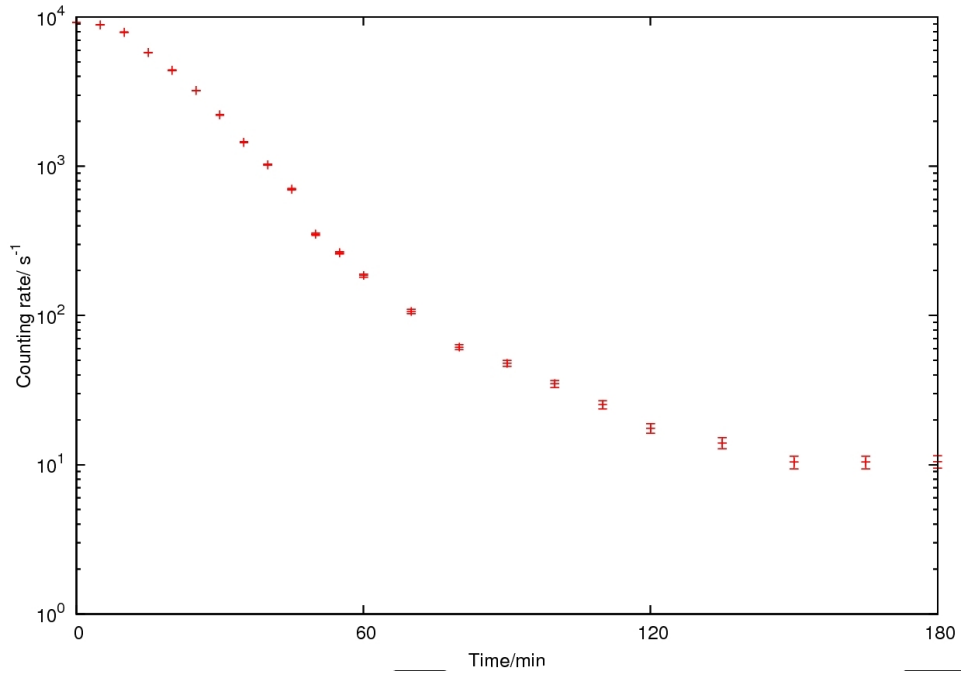
Figure 5.4.: Dark count rate as a function of the cooling time for the PMT R943-02. The dark count rate stays constant after 150 minutes of cooling.

amplitude than the selected threshold (the PMT signals have a negative amplitude). If the noise level is close to the discriminator threshold, some noise signals are also counted. The discriminator threshold is an important setting on the final setup that needs to be optimised. Some preliminary measurements have already been done measuring the dark count rate as a function of the discriminator level. The results are presented in Figure 5.6.

Single photon plateau

The single photon plateau has been determined in the same way as it has been explained in Chapter 4.3.3.
The optimal bias voltage of $V_{ideal}(R943-02) = -1700$ V is taken from the R943-02 plateau measurement shown in Figure 5.7. The maximum supply voltage that can be applied to this PMT is 2200 V as it can be seen in Appendix D.2.1.
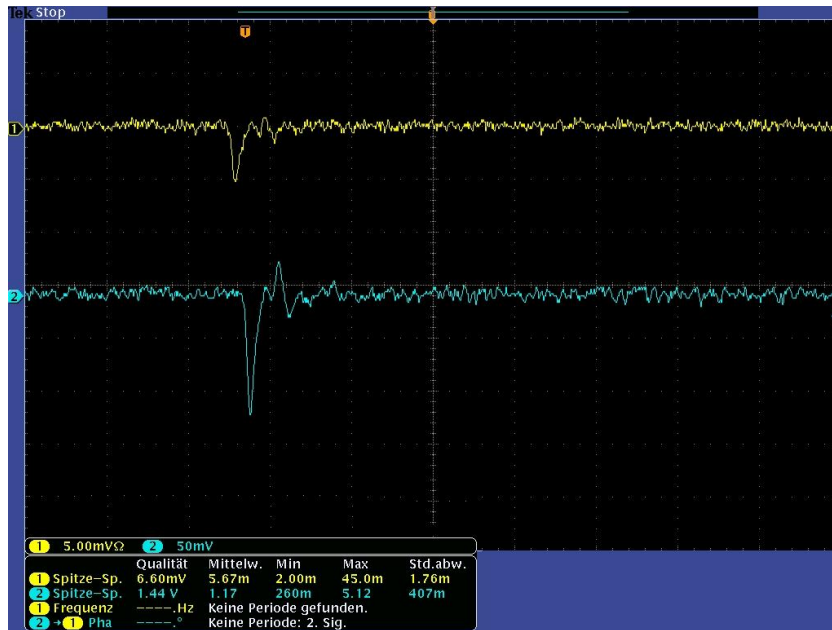
Figure 5.5.: PMT 943-02 signal. Upper signal: direct output. Lower signal: Amplified output (amplitude = 120 mV). It can be seen that the amplitude of the original signal is 5 mV therefore the signal has to be amplified to adapt it to the threshold range of the discriminator.

Figure 5.6.: Dark count as a function of the discriminator level for the PMT R943-02. The discriminator used is a 16 channel C.A.E.N. Mod. N843 where the discriminator level is set between 0 mV and 255 mV.

Figure 5.7.: Single photon plateau for the PMT R943-02.

Quantum Efficiency

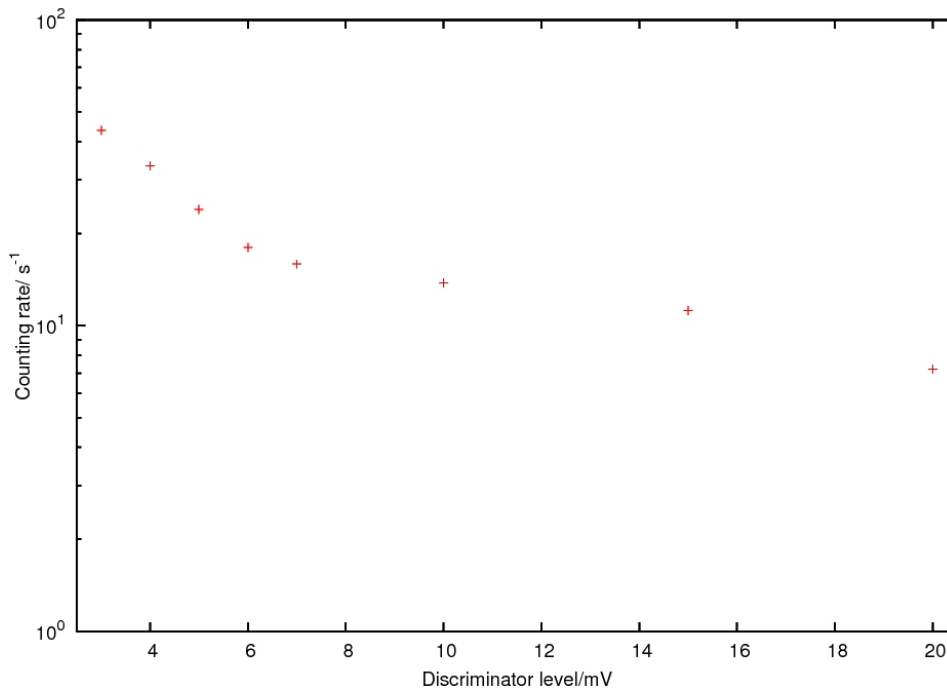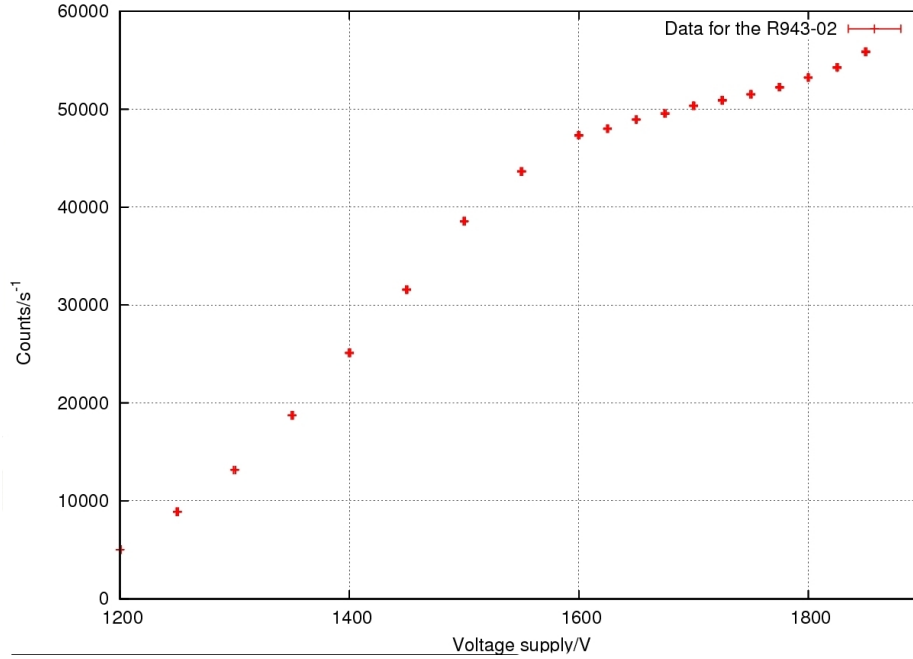The measurement of the quantum efficiency of the PMT R943-02 is done in the same way as described in Section 4.3.3 for the PMT R1017. The measurement setup is the same as the one that can be seen on Figure 4.16.

- $\lambda = 630$ nm

  First of all, a 630 nm LED was used in order to have an estimation of the quantum efficiency at the wavelengths of interest. The signal used for this experiment had an amplitude of 800 mV, the leading and trailing edge was 5 ns and the width was 20 ns. The count rates obtained are shown on Table 5.2.

CPM 1993P			
	Counts	Time/s	Counts/s^{-1}
Dark	1629	200	8.15±0.20
Signal	1992232	200	9961±7
PMT R943-02			
	Counts	Time/s	Counts/s^{-1}
Dark	2250	100	22.5±0.5
Signal	2567464	100	25674±16

Table 5.2.: Count rates using a $\lambda = 630$ nm LED.

$$\text{Counts-Dark (CPM)} = (9953 \pm 7)\text{s}^{-1}$$

$$\text{Counts-Dark (PMT R943-02)} = (25652 \pm 16)\text{s}^{-1}$$

The Quantum efficiency of the PMT R943-02 at 630 nm is (2.577 ± 0.003) times higher than the quantum efficiency of the CPM. As it can be seen in Appendix D.7, the CPM quantum efficiency at 630 nm is 4%. Then, the quantum efficiency measured for the PMT R943-02 is (10.3 ± 1.3)%.

- $\boldsymbol{\lambda = 700}$ **nm**

  In this case the LED used had a $\lambda_{peak} = 700$ nm and the signal that excites the LED had an amplitude of 2 V.

CPM 1993P			
	Counts	Time/s	Counts/s^{-1}
Dark	1416	200	7.08±0.19
Signal	2793	200	14.0±0.3
PMT R943-02			
	Counts	Time/s	Counts/s^{-1}
Dark	1943	100	19.4±0.4
Signal	4954	100	49.5±0.7

Table 5.3.: Counting rates using a $\lambda = 700$ nm LED.

$$\text{Counts-Dark (CPM)} = (6.9 \pm 0.4)\text{Hz}$$

$$\text{Counts-Dark (PMT R943-02)} = (30.1 \pm 0.8)\text{Hz}$$

The quantum efficiency of the PMT is (4.4 ± 0.3) times higher than the quantum efficiency of the CPM at a 700 nm wavelength. If the quantum efficiency of the CPM at 700 nm is 1% (see Appendix D.3.2), the quantum efficiency of the PMT at the same wavelength is (4.4 ± 2.2)%. According to the figure on Appendix D.2.3, the PMT 943-02 Q.E. should be 11% at 700 nm. These differences between the theoretical curves and the experimental results will be discussed at the end of this section.

- $\boldsymbol{\lambda = 940}$ **nm**

  For the 940 nm LED a 2 V pulse was used in order to excite it. At this wavelength the dark count rate cannot be distinguished from the signal rate in any of the detectors used. The expected quantum efficiency is in both cases under 0.1% (see Appendix D.5 and D.7).

CPM 1993P			
	Counts	Time/s	Counts/s^{-1}
Dark	703	100	7.0±0.3
Signal	689	100	6.9±0.3
PMT R943-02			
	Counts	Time/s	Counts/s^{-1}
Dark	1832	100	18.3±0.4
Signal	1923	100	19.2±0.4

Table 5.4.: Counting rates using a $\lambda = 940$ nm LED.

Discussion

Possible reasons for the differences of the measured PMT Q.E. and the Q.E. stated in the datasheet are:

1. The CPM quantum efficiency is higher as listed in the datasheet.

2. The PMT quantum efficiency is lower as listed in the information received from Hamamatsu.

3. There might be a temperature dependence of the Q.E. of the PMT R943-02. The PMT is operated at temperatures between -40°C and -30°C, which is at the lower edge of the operational range quoted in the datasheet of the device.

4. Strictly speaking, we are not measuring the quantum efficiency of the devices, but the Photodetection efficiency (PDE). The PDE results from the product of the Q.E. and the photoelectron collection efficiency (CE). The collection efficiency is the probability that single photoelectrons emitted from the photocathode can be finally collected at the anode. The latter can vary in a rather broad range between 50% and 90% [Ham08a], depending on the actual device and the base used with the PMT, and is usually not quoted in the datasheets. On Figure 5.8 the collection efficiency as a function of the photocathode to first dynode voltage can be seen.

   In the measurements presented in this (and the previous) chapter, we implicitely assume the photoelectron collection efficiencies of the CPM and of the different PMTs to be identical.
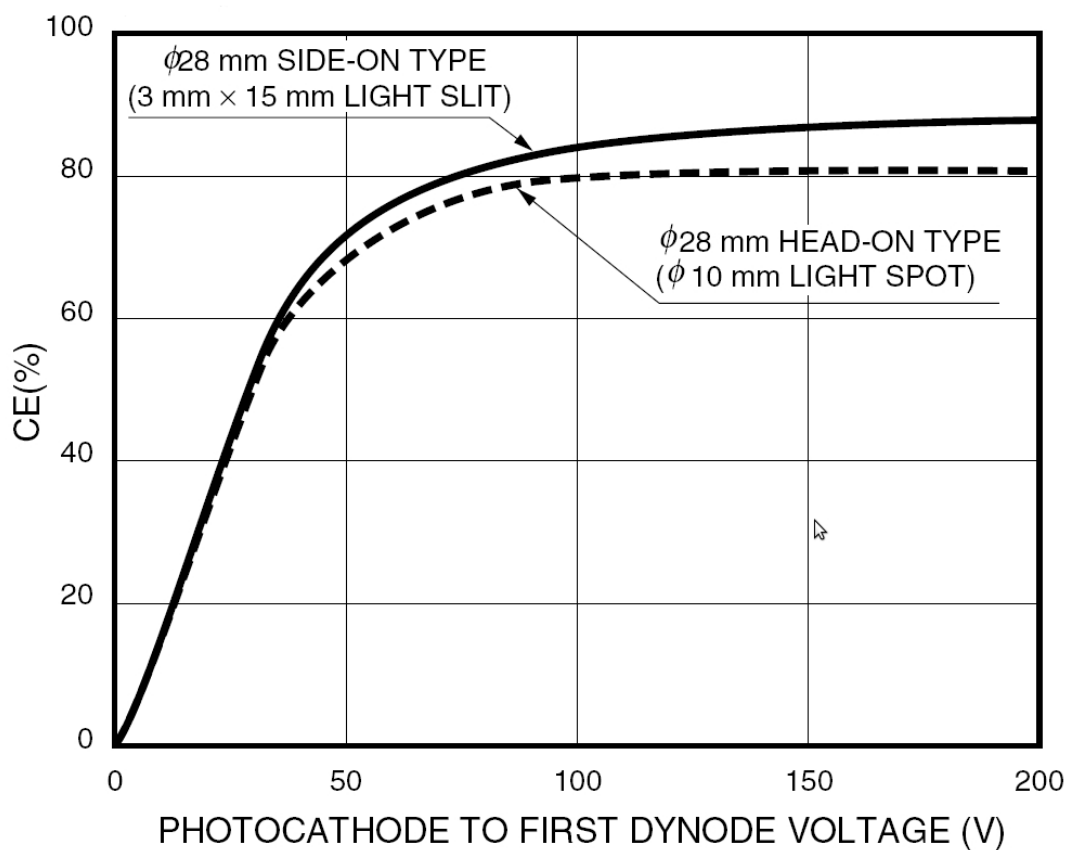
Figure 5.8.: The figure shows the relation between the collection efficiency and the pho-
tocathode to first dynode voltage for the $\varnothing = 28$ mm PMT. The collection
efficiency (CE) sharply varies at voltages lower than 100 V, but becomes sat-
urated when the voltage exceed this. This means that a sufficient voltage
should be applied across the photocathode and the first dynode to obtain
stable CE. Image from [Ham01].

6. Parasitic test measurements at ESR

In this chapter test measurements performed with the parabolic mirror setup at the ESR will be presented. The measurments took place in a parasitic mode during a special relativity (SRT) experiment [Sph10], where a Li$^+$ beam with $\beta = 0.338$ was circulated in the ESR. The main points of interest during the test were firstly to see if the parabolic mirror has a negative effect on the stored ion beam and secondly to study the sources and characteristics of background photons in the ESR. As there was only very limited access to the ESR hall and also only a short measurement interval for beam tests with the mirror during the SRT experiment, no fine-tuning of the mirror system and its readout electronics could be performed. Some of the results obtained during the beamtime therefore don't have quantitative importance because the settings used weren't the optimal ones, but they are qualitatively relevant. The results of the beam tests are summarized in Section 6.1. An optimization of the readout electronics of the parabolic mirror setup has been performed at a later stage, during a scheduled downtime of the ESR, see Section 6.2.

It's important to remark that all these measurements have been performed using the Linos OG 590 Pale-red filter. Due to the outcome of the measurements, it was decided that for the actual Bismuth experiment a second filter (Linos NIR-Blocking Filter CALFLEX X) will to be used in order to have high transmission only at the wavelengths of interest.

6.1. Beamtime tests

It is crucial to experimentally observe the effect of the movement and final placement of the mirror on all the parameters related to the experiment. If the mirror were to interfere with the beam and absorbing ions the experiment can't be successful. The efficient collection of the fluorescence photons has also to be checked. Finally, the effect on the detectors of the mirror section, which might be shaded by the parabolic mirror, will be measured in order to study the possibility of using them as additional diagnosis tool.

6.1.1. Effect of the parabolic mirror on the ion current

The mirror was designed not to interfere with the ion beam. As is mentioned in Section 4.2.2, the width of its central slit corresponds to $> \pm 3\sigma$ of the width of the Li-like Bi ion cloud and should thereforeonly interact with ions in the tail of the density profile of the beam.
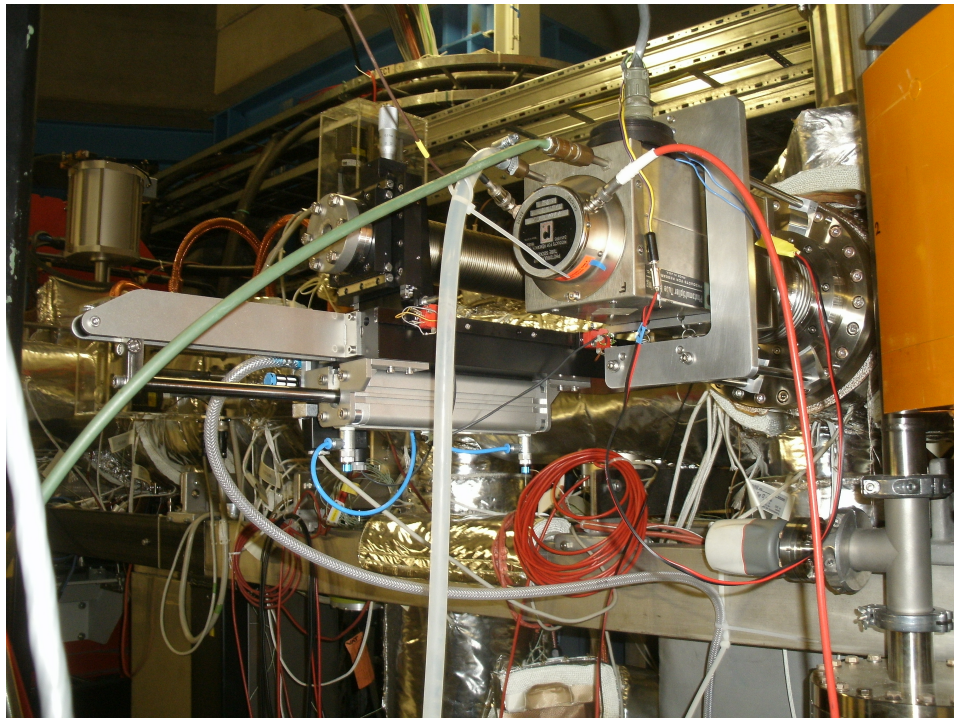
Figure 6.1.: Picture of the parabolic mirror setup mounted at the ESR.

In spite of the theoretical calculations, the effect of the mirror on the ion current must be checked especially because of a slight shaking of the copper mirror when it is moved to the center of the beampipe. A representation of the ion current and the dark count rate of the PMT can be found on Figure 6.2.

The ion current decreases by 21% to 26% when the mirror is moved into the beam, what means that not just ions situated in the region $> 3\sigma$ are absorbed by the mirror. One possible reason of this drop of the ion current is that the mirror isn't centered around the beam, therefore an adjustment of the mirror height needs to be done in order to find a position where the losses are minimized. Another possible reason is the already mentioned shaking of the copper mirror, when it is moved into position. This can only be minimized by proper lubrication of the linear feedthrough and by a slow movement of the mirror. A bigger problem is that the width of the Li beam used is three times smaller than the expected width of the Li-like Bismuth beam of the planned experiment [Loc10b]. Therefore, with the Bi beam, more ions are expected to be absorbed by the mirror. An important point is that the PMT count rate doesn't exhibit an overshout when the mirror is moved into the center position. This means the ions don't generate a large amount of photons when they hit the mirror.

In order to model the decrease of the ion current the fit function shown on Equation 6.1 is used:

$$I_{ion}(t) = A_0 \cdot \exp\left(\frac{t - t_0}{\tau}\right) + y_0 \qquad (6.1)$$
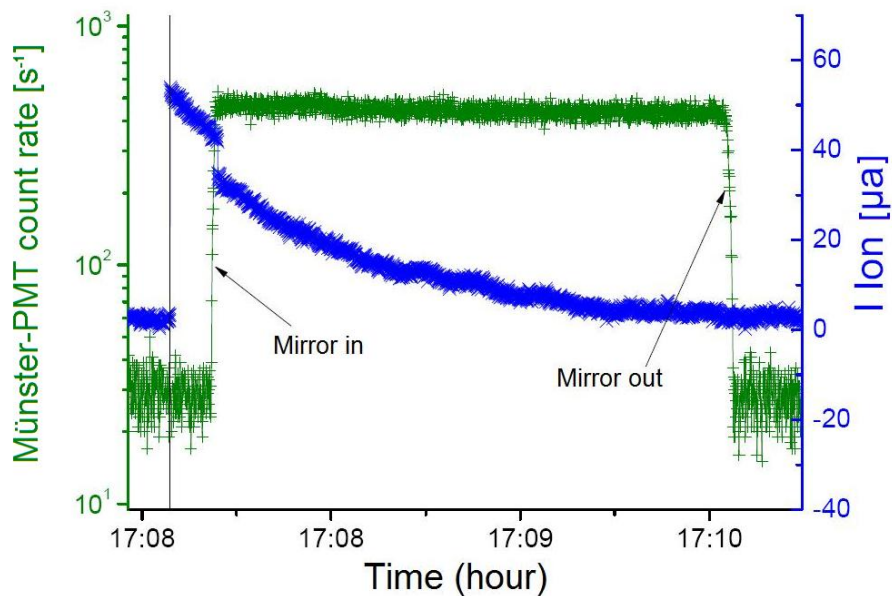
Figure 6.2.: Ion current (right scale) and PMT R1017 background count rate (left scale). When the mirror is moved into the beam an increment of an order of magnitude in the count rate measured by the PMT can be seen. On the other hand, a decrease of the ion current can also be seen.

Ion current/μA		Difference
before	after	
42.28	33.51	-21%
43.92	34.87	-21%
39.95	29.94	-25%
40.91	30.07	-26%

Table 6.1.: Decrease of the ion current when the mirror is moved into the Li$^+$-beam. The decrease goes from 21% to 26%.

t_0 is the injection time. The parameters y_0 corresponds to an offset of the current measuremtent and is calculated to be -1.16321 μA. τ is the decay time of the ion current and A_0 the amplitude at $t = t_0$. On Figure 6.3 fitted A_0 and τ values for 95 injections of ions into the ESR during the experiment are represented. To calculate mean values just the points lying inside the 2σ area of the parameter space have been taken into account. Outside this area we find 10% of the data points. As the parameters should follow a Gaussian distribution, only 4.6% of the data should be out of the 2σ area. An explanation could be that there were some variable conditions during the experiment (in the ion injection) or there aren't data points enough to have a statistically reasonable adjustment.
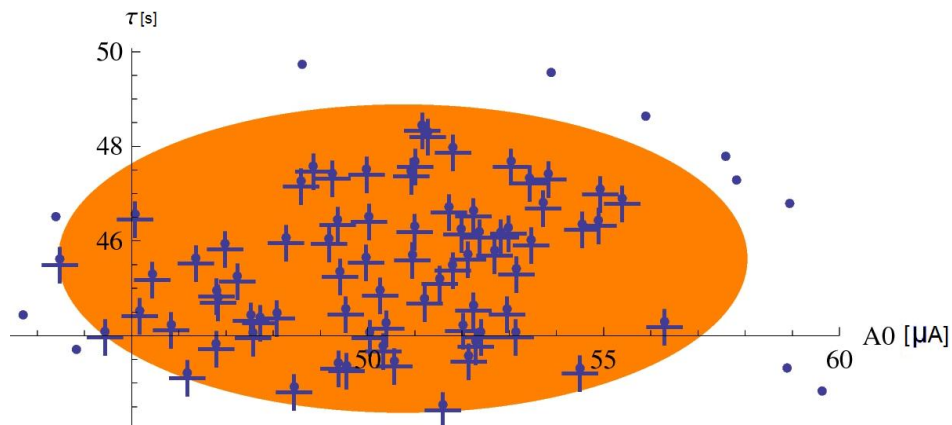

Figure 6.3.: Limitation of the fit parameter space. Each point corresponds to one current decay. A_0 is the amplitude in μA, τ is the decay constant in seconds. The points marked with a + are the ones inside the 2σ area and are considered in the mean values given. Image from [Loc10c].

The results are separated into ion injections with (4 injections) and without (91 injections) the insertion of the mirror into the beam.

$$\tau_{\text{without mirror}} = (45.5 \pm 1.6)\text{s} \tag{6.2}$$

$$\tau_{\text{with mirror}} = (46.8 \pm 4.8)\text{s} \tag{6.3}$$

It can be seen on equations 6.2 and 6.3 that the life time of the ions with and without mirror is identical within the uncertainty of the measurement. This shows, that after an initial decrease in the number of stored ions due to the mirror stripping off the tails of the density distribution of the beam, there is no further interference of the mirror with the ions.

6.1.2. Measured background count rates

The measured rate of background photons with the mirror in or out of the beam position can also be seen on Figure 6.2. The dark count rate when the mirror is moved into

the beam increases by an order of magnitude, which means that the mirror collects more background photons. These background photons were mostly generated by LEDs mounted near the laser entry windows for calibration purposes during the beamtime of the SRT experiment that was taking place at the time these parasitic measurements were done. The background count rates of the PMT for the different situations are shown in Figure 6.4 and on Table 6.2.

Ions	Mirror	Counts· Hz (1)	Counts· Hz (2)
In	Out	408.5±2.0	406.9±2.0
In	In	6106.9±8.0	5857.73±8.0
Out	In	5549.51±7.0	
Out	Out	357.5±1.9	

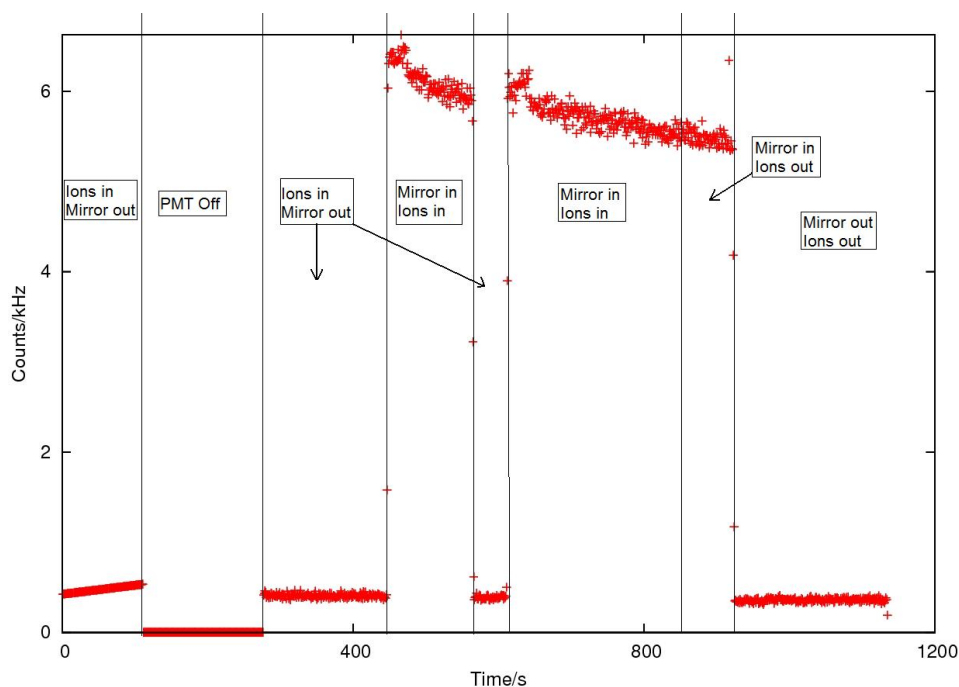Table 6.2.: Count rate for different combinations of ion beam and mirror position.

Figure 6.4.: Plot of the R1017 count rate during the test measurement at the ESR. The count rate variation reported in Table 6.2 can be seen here.

Looking at the plots of Figure 6.5, the different situations tested with the PMT R1017 and the parabolic mirror setup are represented. Shown is the ion current together with the dark count rate of the PMT. In the upper plots the decrease in the dark count rate of the PMT when the mirror is moved out can be observed. In the lower left plot the decrease of the ion current when the mirror is moved in and also the exponential decay of the count rate when there are ions in the ESR is reported. As the lasers were switched

off when the tests of the parabolic mirror were performed, the decrease of the measured photon rate with the beam current is due to the decrease of excitations of rest gas atoms by the ion beam. The last picture shows that there aren't any changes of the count rate when ions are injected if the mirror is in the retracted position.
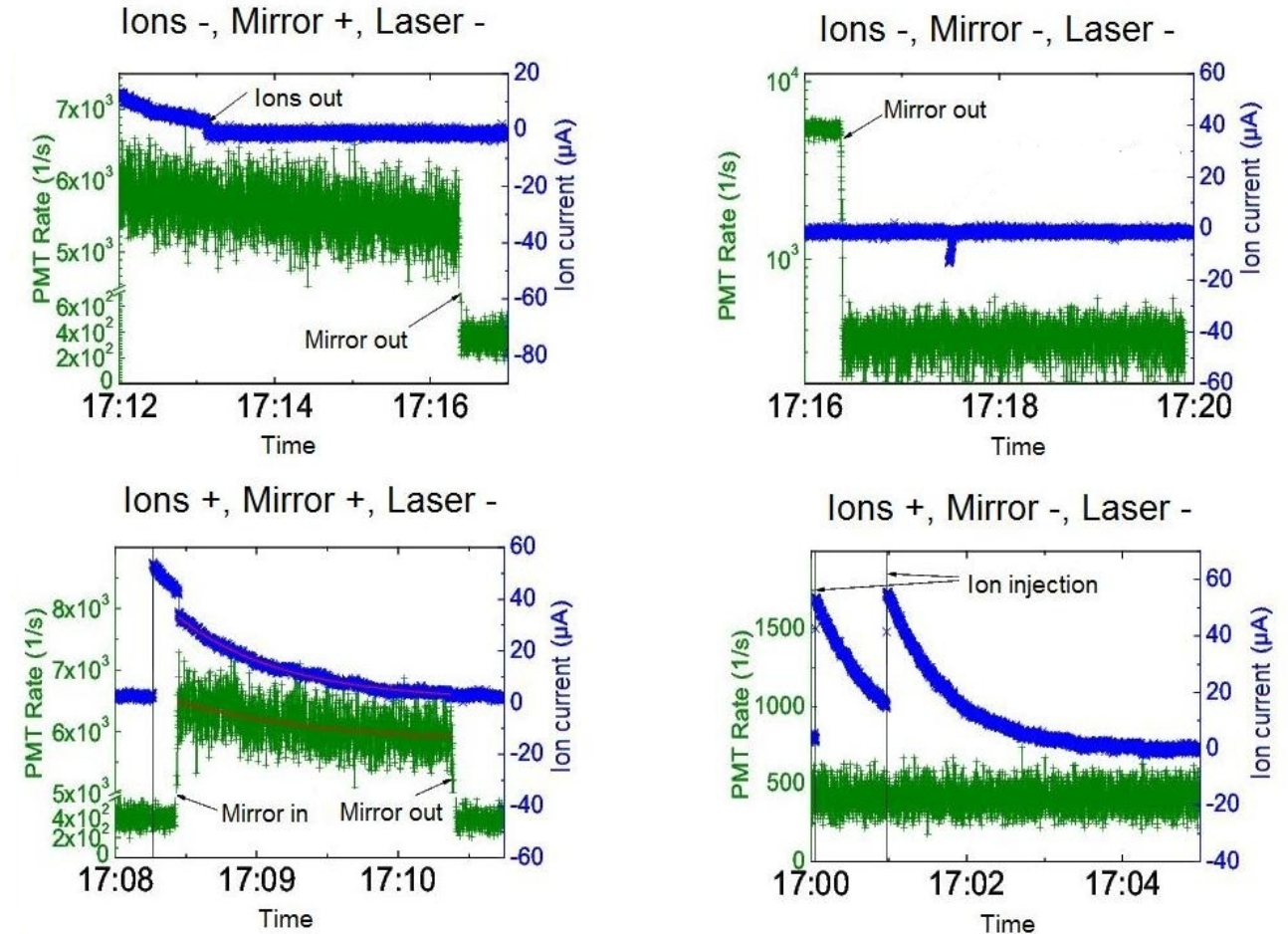

Figure 6.5.: Count rate of the selected PMT R1017 used in the parabolic mirror setup. The reported effect can be seen on the plots. The lasers were swichted off during these measurements because the filter used, a Linos OG 590 Pale-red filter, protects the PMT only from the 386 nm laser but not from the 780 nm laser.

A measurement of the dark count rate without ion beam was performed to check the sources of background photons not related to the ion beam. To do it, measurements with open and closed laser windows, a flashlight and also the LED lamp on the colinear laser window were done. The results are reported in Table 6.3.
Looking at the quoted count rates it is obvious, that the largest source of background photons is the infrared LED that has been placed for calibration purposes of the SRT experiment behind the laser window in colinear direction.

	Mes.1	Mes.2	Mes.3	Mes.4	Mes.5	Mes.6	Mes.7	Mes.8
Flashlight	Off	Off	Off	Off	Off	On	Off	Off
Window in the colinear direction	Closed	Open	Open	Open	Open	Closed	Closed	Closed
Window in the anti-colinear direction	Closed	Closed	Closed	Closed	Closed	Open	Open	Open
Mirror	Out	Out	Out	In	In	In	In	Out
Infra-red LED on the colinear window	On	Off	On	Off	On	Off	Off	Off
Counts·Hz	12.8±0.3	136.4±1.2	1296±4	165.6±1.3	25822±16	180.2±1.3	169.8±1.3	18.9±0.4

Table 6.3.: Count rates for different experimental configurations. The highest count rates are observed when the window in colinear direction is open and the infrared LED behind this window switched on. Table from [Lop10b].

As the laser excitation of ions in the Li-like Bi experiment will take place on the opposite side of the ESR, and both windows on the detector sice will be closed, we expect a much lower background rate then. Nevertheless it has been decided to add another filter blocking infrared photons (Linos Calflex-X [Lin10]) for any upcoming measurements.

6.1.3. Effect of the new setup on the mirror section

The measurements performed with the detectors of the mirror section that is located upstream of the parabolic mirror setup had the objective to check wheter both detection systems can be operated in parallel or interfere with each other. The detectors of the mirror section are suitable to be used with the laser on because they have different filters and don't have problems due to the stray light coming from the laser. The detectors used in this setup are three selected PMT R1017. The detectors are more than ten years old and therefore the Q.E. may have decreased due to the aging effects. The results of the measurements are shown on Figure 6.6.

- In the upper left plot it can be seen again that the ion current decreases when the parabolic mirror is moved into the beam position. The background count rate of the SRT-PMT stays constant over the largest part of the measurement.

- In the lower plot on the left it can be seen that the movement of the mirror results in a short increase of the background count rate of the SRT-PMT. This can be due to Li-ions that undergo a collision with the mirror material and are excited in the process.

- In the upper plot on the right the exponential decay of the ion current can again be observed. It has to be remarked that the laser was switched on during this measurement and the count rate of the PMT measuring fluorescence photons of the excited Li^+ ions therefore presents an exponential decay too.

- In the lower plot on the right the laser effect is also observed. The background count rate is constant when the laser is off and only has a peak due to the movement of the mirror. When the laser is switched on, the count rate increases and starts to decay exponentially as it has been said before. It can be seen that also the retraction of the mirror causes again some losses in the ion current, that lead to a decreased count rate in the SRT-PMT.

6.2. Optimization of the readout electronics

This section covers the optimization of the readout electronics of the parabolic mirror setup. The selection of the optimal threshold level for the discriminator, the dependence of the count rates on the placement of the devices and also ways to minimize background light sources will be discussed.
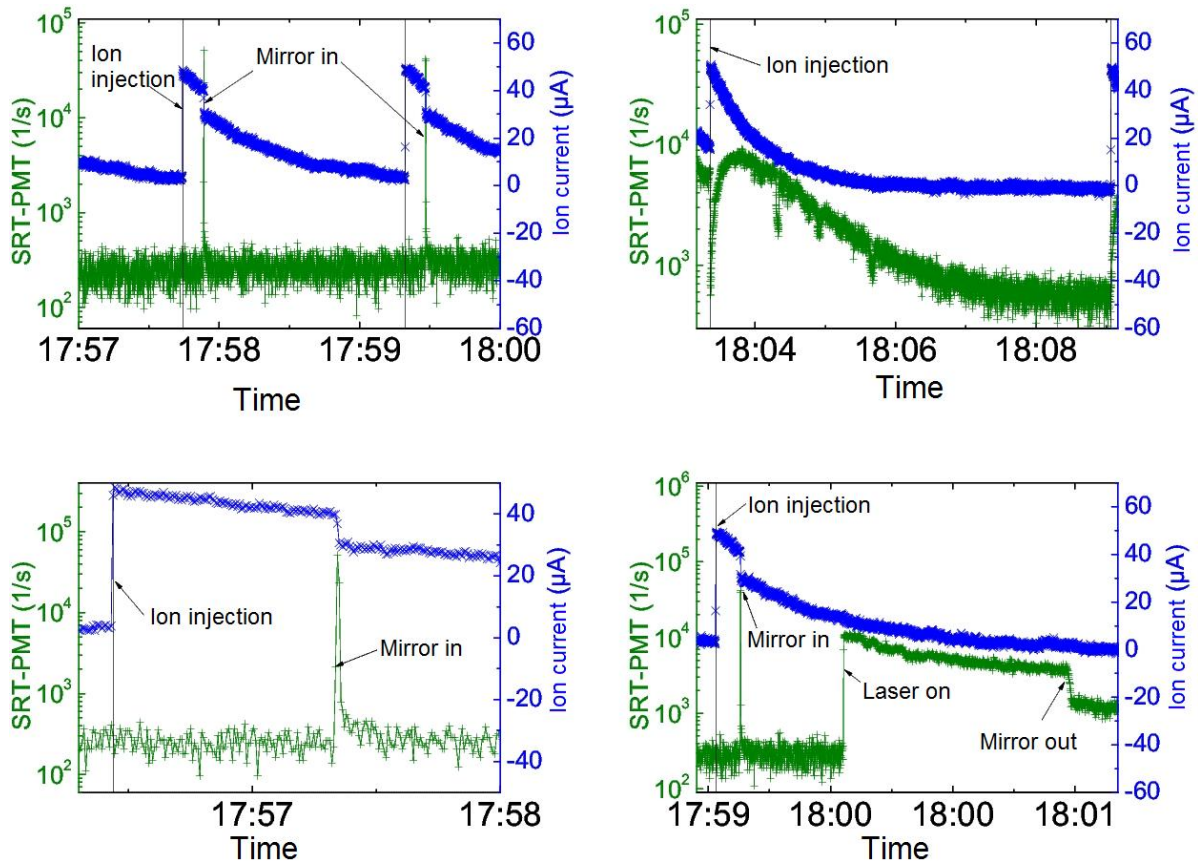
Figure 6.6.: Count rates of the mirror section detectors. Upper left: background count rate of the SRT-PMT with and without the parabolic mirror. Lower left: close up of the upper left plot. A short increase in the background rate is observed when the mirror is moved into position. Upper right: count rate of the SRT-PMT without parabolic mirror, but with the laser switched on. Lower right: count rate of the SRT-PMT with parabolic mirror and laser.

6.2.1. Determination of the optimal threshold level

In order to determine the optimal threshold level to be used in the final setup the procedure indicated in the "photon counting" booklet by Hamamatsu [Ham01] will be applied. That method consists of measuring the count rate as a function of the discriminator level. When this is done, the curve obtained needs to be differentiated. The resulting curve has a local minimum which corresponds to the optimum threshold value (see Figure 6.7).
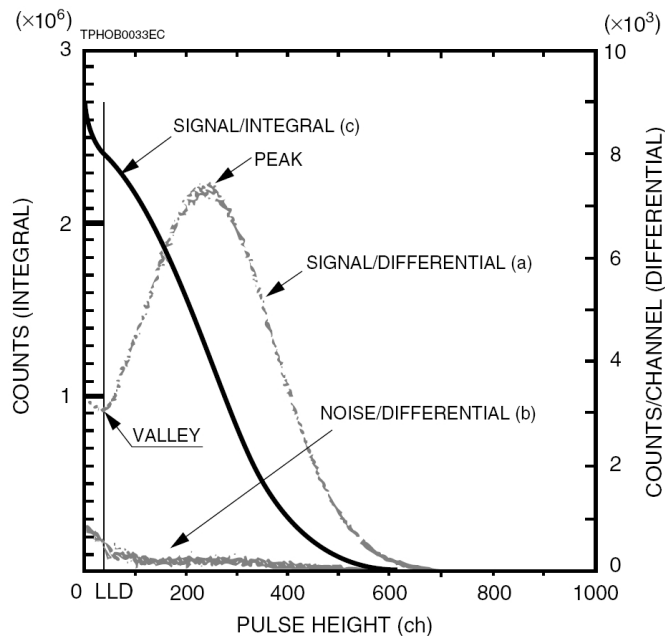

Figure 6.7.: Differential and Integral curves of the pulse height distribution. The point marked with LLD corresponds to the optimum Lower Level Discrimination threshold. This is where the discriminator level needs to be set in order to get rid a large part of the noise while retaining as many signal counts as possible.

Because a precise timing of the PMT signals is required to allow a narrow gate to be set for the count rate measurement during the periods when the ion cloud passes the detector, we will use a Constant Fraction Discriminator (CFD). The delay of the CFD should be set to:

$$T_{\text{delay}} = T_{\text{fall}}(1 - F) \tag{6.4}$$

where F is the constant fraction, which for the C.A.E.N. Mod. N843 discriminator is F = 20%. The fall time of the PMT signals has been measured with the oscilloscope and is ca. $T_{\text{fall}} = 7$ ns. If these values are introduced in Equation 6.4, the value for the optimal delay of the discriminator is:

$$T_{\text{delay}} = 5.6 \text{ ns} \tag{6.5}$$

The pulse height distribution was measured placing the discriminator in the measurement hut in order to determine its optimal level in this situation. The measurements were performed with different delay values of the discriminator. Channels 0 and 1 of the discriminator were used with 4 ns and 8 ns delay respectively.

The CFD used can operate also with small (below 10 mV) input signals, but in this case the Constant Fraction operation is not performed, i.e. the time walk is higher [Cae02]. In order to have a sufficient signal amplitude for the CFD, the PMT signals are amplified twice using cascaded channels of a C.A.E.N. N979 fixed gain amplifier.

Two measurements using the cascaded amplifier were performed. One with the discriminator placed inside the ESR hall and the other one with the discriminator in the measurement hut. The results are shown on Figures 6.8 and 6.9.
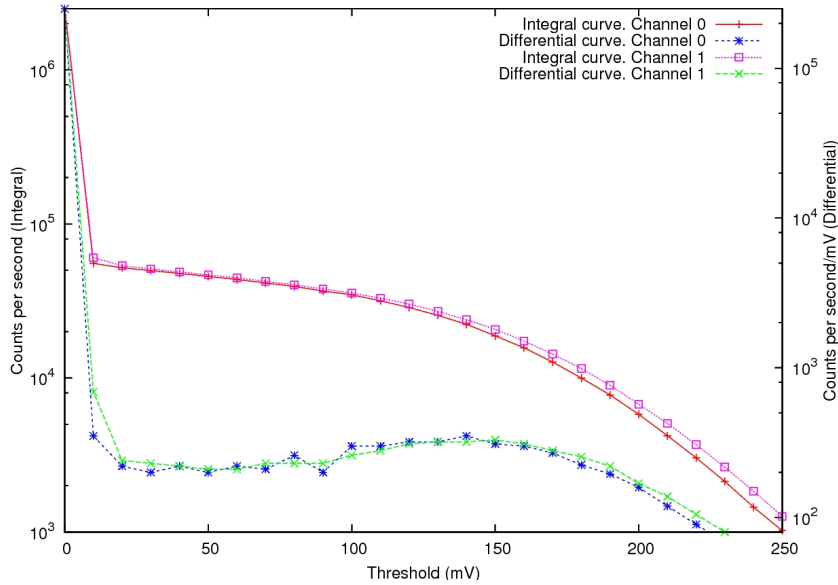

Figure 6.8.: Differential and Integral curves of the pulse height distribution measured in the ESR hall. The optimum LLD is located in the valley of the differential curve. For a delay time $t_{delay} = 4$ ns the optimal threshold level is -50 mV and for $t_{delay} = 8$ ns the optimal threshold level is -60 mV.

The measurements placing the discriminator inside the ESR were performed in order to check for effects of signal degradation during transport of the signals to the measurement hut. The data of interest is measured with the discriminator in the measurement hut, where it will be placed for the actual experiment. When the discriminator is placed next to the amplifier in the ESR hall, the optimum threshold values are -50 mV (for $t_{delay} = 4$ ns) and -60 mV (for $t_{delay} = 8$ ns). For a placement of the discriminator in the measurement hut we obtain:

$$\text{Op.threshold (4 ns)} = \text{Op.threshold (8 ns)} = -30 \text{ mV} \qquad (6.6)$$

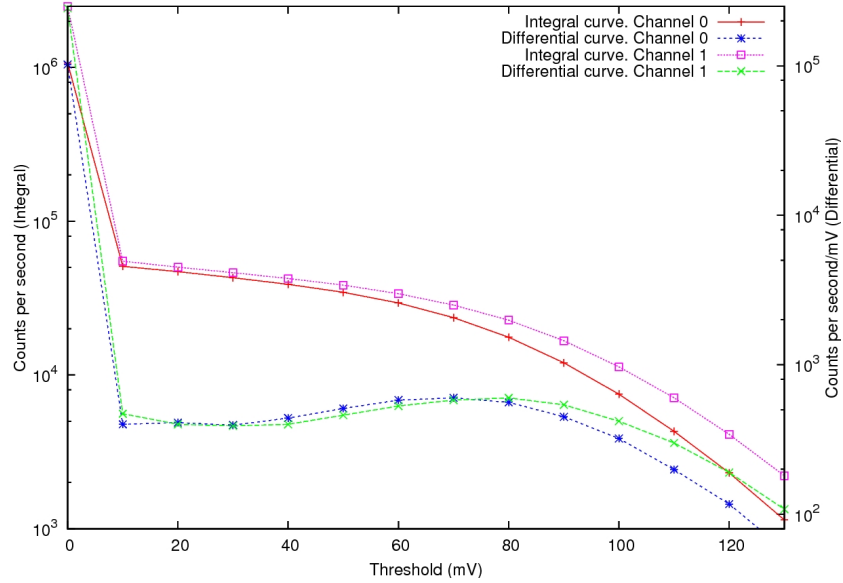The results are summarized in Table 6.4.

Figure 6.9.: Differential and Integral curves of the pulse height distribution measured in the Measurement hut. For both channels the optimal threshold level is -30 mV.

Discriminator placement	Internal delay/ns	Threshold/mV	Measured rate/kHz
Measurement hut	4	30	42.9±0.1
Measurement hut	8	30	46.3±0.1
ESR	4	50	45.6±0.1
ESR	8	60	44.6±0.1

Table 6.4.: Count rates obtained at the optimal threshold levels for different situations. It can be seen that the count rates obtained by placing the discriminator inside the ESR hall or in the Measurement hut are similar. All the measurements have been performed with the same light source (ESR lights) in order to be comparable.

6.2.2. Differences between the location of the devices

It has been shown by the results in Table 6.4 that the location of the *Constant Fraction Discriminator* doesn't influence the measured count rate. It has also to be checked if the location of other devices influences the results of the measurements.

The *High Voltage Power Supply* (ISEG NHQ 226L) used for these measurement is one of the devices that must be tested. It can be remote controlled so it could be placed either in the measurement hut or inside the ESR hall. The results of the test measurements are shown in Table 6.5. It can be seen that there aren't significant differences between the results obtained placing the HV power supply inside or outside the ESR hall.

HV placement	Internal delay/ns	ESR Lights	Mirror	Counting rate/kHz
Inside ESR	4	On	In	764.4±0.3
			Out	43.01±0.07
Measurement hut	4	On	In	764.4±0.3
			Out	42.40±0.07
		Off	In	1.990±0.014
			Out	0.211±0.005
	8	On	In	770.1±0.3
			Out	48.27±0.07
		Off	In	2.253±0.015
			Out	0.236±0.005

Table 6.5.: Count rates for the different placements of the HV power supply.

As no significant drawbacks have been observed when discriminator and HV supply are placed in the measurement hut, for easy access during the experiment, the proposed experimental setup is shown on Figure 6.10.

6.2.3. Background light sources

Having a light tight setup is one of the most important aspects to decrease the rate of detected background photons. To reduce this background, some measurements have been performed in order to check the places where the enviromental light could enter the beamline and arrive at the photocathode of the PMT.

First of all, the *pressure gauges* installed inside the beampipe need to be disconnected during the experiments because they emit light. All feedthroughs containing *ceramic isolators* need to be covered because the ceramic let the light get through. The *mirror section windows* must also be covered. The *LED connector* placed on the cooling house adaptor also needs to be covered because it has a plastic piece that also lets the light get through.

The most important light leak that needs to be closed is part of the *optical adaptor*. The joints of the adaptor to the ESR window and also to the cooling housing have a slight
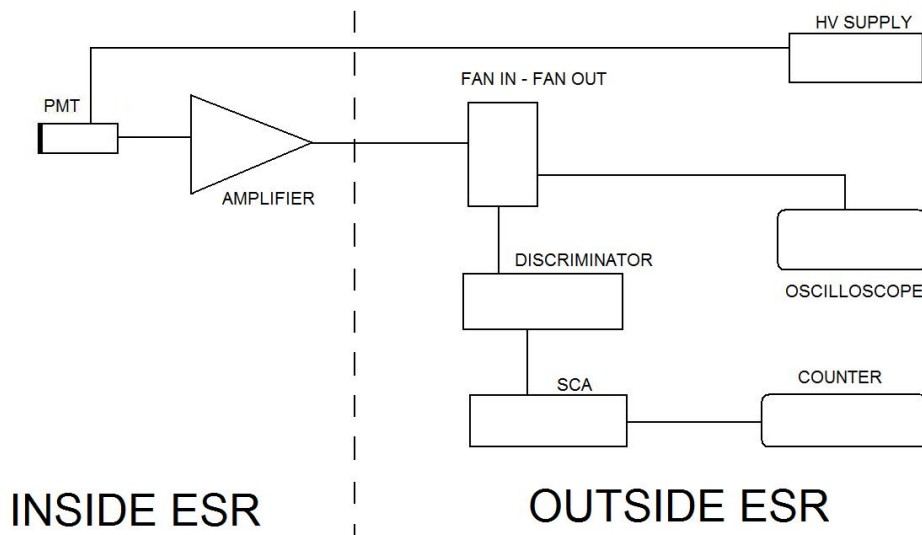
Figure 6.10.: Location of the devices in the final setup.

gap in the metal-metal junction. To close it a deformable rubber piece is proposed to be used in between these joints.

6.3. Jitter and delay of the different signals

Jitter corresponds to variations in the timing of digital signals. It determines the quality of timing measurements. The delay is measured between the photon emission and the signal being counted. In order to measure the jitter and the delay of the signals an LED attached to the optical adaptor of the parabolic mirror was used. The setup used for these measurements can be seen on Figure 6.11 for the measurements inside the ESR hall and on Figure 6.12 for the measurements in the measurement hut.

The function generator was set to a pulse with a 50 kHz frequency, leading and trailing edges of 5 ns and width 10 ns. It has to be taken in account that the jitter measurement is limited by the unknown photon emission time of the LED due to the width of the pulse. This uncertainty is estimated to be smaller than ± 5 ns. To this uncertainty on the photon emission, the uncertainty on the jitter measurement has to be added. This has been estimated to be ± 2.5 ns.

As the extension of the ion cloud in time is 100 ns [Ani10a] and the CFD jitter is (15 ± 8) ns, if we the jitter is supposed to be symmetric, the measurement window should be set to 123 ns in order to be sure that all the signals will be detected.
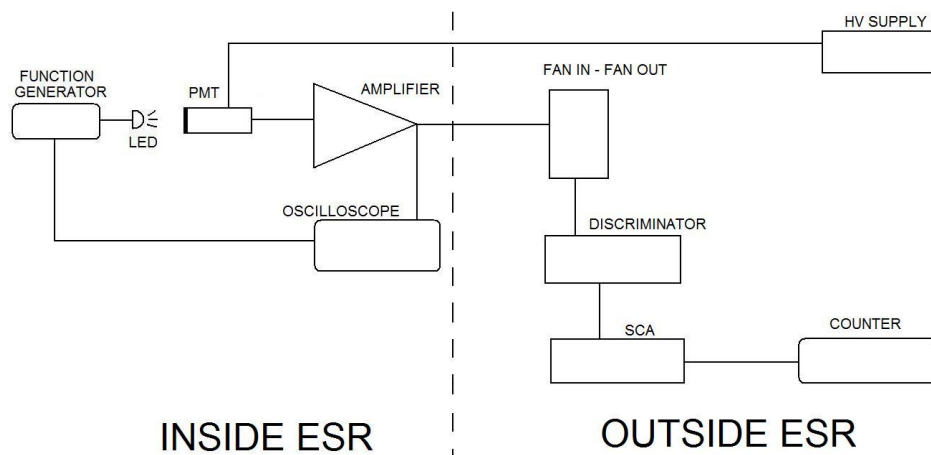
Figure 6.11.: Jitter and delay measurement setup inside the ESR hall. Function generator and oscilloscope were also placed inside the ESR.
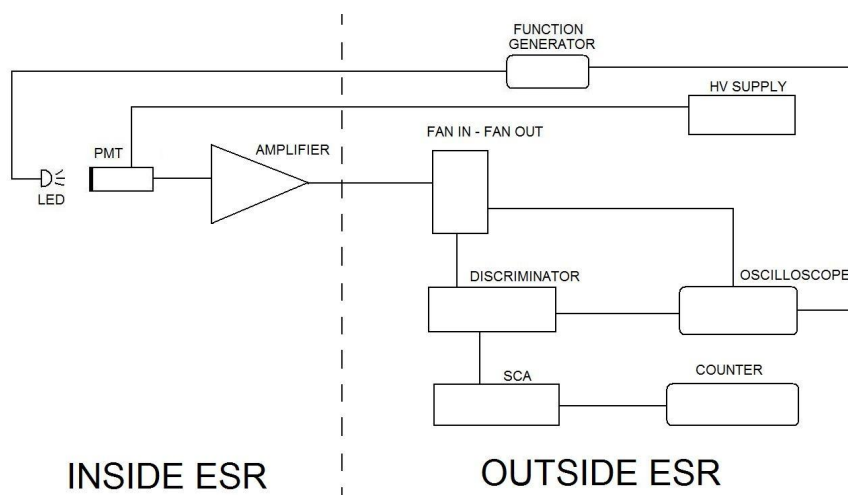

Figure 6.12.: Jitter and delay measurement setup in the measurement hut. The amplifier and discriminator signals were measured in the place where the signal will finally be received. Function generator and oscilloscope were placed together with the other devices in the measurement hut.

Positioning of pulse generator and oscilloscope	Output measured	Jitter/ns	Delay/ns
ESR	Fast amplifier	10±8	130±5
Measurement hut	Fast amplifier	20±8	800±5
Measurement hut	CFD (t_{delay} = 4 ns)	15±8	814±5
Measurement hut	CFD (t_{delay} = 8 ns)	15±8	818±5

Table 6.6.: Jitter and delay of the signals after the Fast amplifier and the Constant Fraction Discriminator (CFD).

7. Conclusion and Outlook

To finish the thesis the most important results will be summarized in this chapter. A summary of preparation tasks that still need to be completed in order to have the setup ready for the beamtime that is expected to take place Spring 2011 is given at the end of the chapter.

7.1. Conclusion

- The parabolic mirror setup doesn't interfere with the segmented mirror section.

- The reflectivity of the materials of the parabolic mirror setup has been checked:

  -MIRO-2 reflectivity = $(89.4\pm0.9)\%$

  -OFHC-Copper reflectivity = $(97.1\pm0.9)\%$

- Transmission of optical components of the setup:

  -Light guide + Filter transmission coefficient = $(83.3\pm0.8)\%$

  -Window transmission coefficient (angles $< 45°$) $>90\%$

- The quantum efficiencies of the detectors for the parabolic mirror setup and the forward detection setup have been checked by a Perkin Elmer 1993P Channel Photomultiplier (see Table 7.1).

Wavelength	CPM 1993P	R1017	R943-02
630 nm	$(4.0\pm0.5)\%$	$(8.4\pm1.1)\%$	$(10.3\pm1.3)\%$
700 nm	$(1.0\pm0.5)\%$	$(3.1\pm1.6)\%$	$(4.4\pm2.2)\%$

Table 7.1.: Quantum efficiency of the detectors for the different wavelengths.

- Additional parameters of the detectors that have been measured:

  <u>R1017</u>

  The cooling time needed to achieve the operational temperature is 120 minutes. The bias voltage of the PMT has been measured to be -1300 V. The dark count rates achieved with the cooled PMT on the test bench are < 100 s^{-1}. The lowest background rate achieved with the setup mounted at the ESR (without ion beam)

is 211±5 s^{-1}. The background can possibly be further reduced using the shortpass filter mentioned in Chapter 4.3.2.

<u>R943-02</u>

The cooling time needed to achieve the operational temperature is 150 minutes. The optimum bias voltage has been found to be -1700 V. The dark count rate of the cooled detector is around 20 s^{-1}.

- The influence of the movement of the mirror on the ion current in the ESR is significant but still aceptable for the proposed experiment. An important improvement of this effect is expected when the position of the mirror in the beam pipe is adjusted precisely with the help of a laser system. The lifetime of the ions in the ESR is the same with and without mirror in the beam position. This means that the mirror only interferes with the beam when it is moved in. No excess of background photons have been measured when the ions hit the mirror.

- Placement and settings of the readout electronics of the parabolic mirror setup have been found. The optimal delay for the CFD is 4 ns and the threshold level in the measurement hut -30 mV. The timing jitter of the discriminated pulses has been found to be (15±8) ns. Considering the time the ion cloud in the ESR takes to pass the detector a measurement window of ca. 123 ns needs to be set to make sure all fluorescence photons can be detected.

7.2. Outlook

- Using the optimized settings and the proposed additional filter, another beam test should be performed to check the background photon rate. The sources of background light identified in this thesis should be removed during that measurement.

- Similar beam test measurements for the forward direction system need to be done in order to find the optimal settings.

- Light leaks between the adaptor, the cooling house and the ESR window need to be fixed. A rubber ring has been proposed as a solution but it has to be tested before the final experiment.
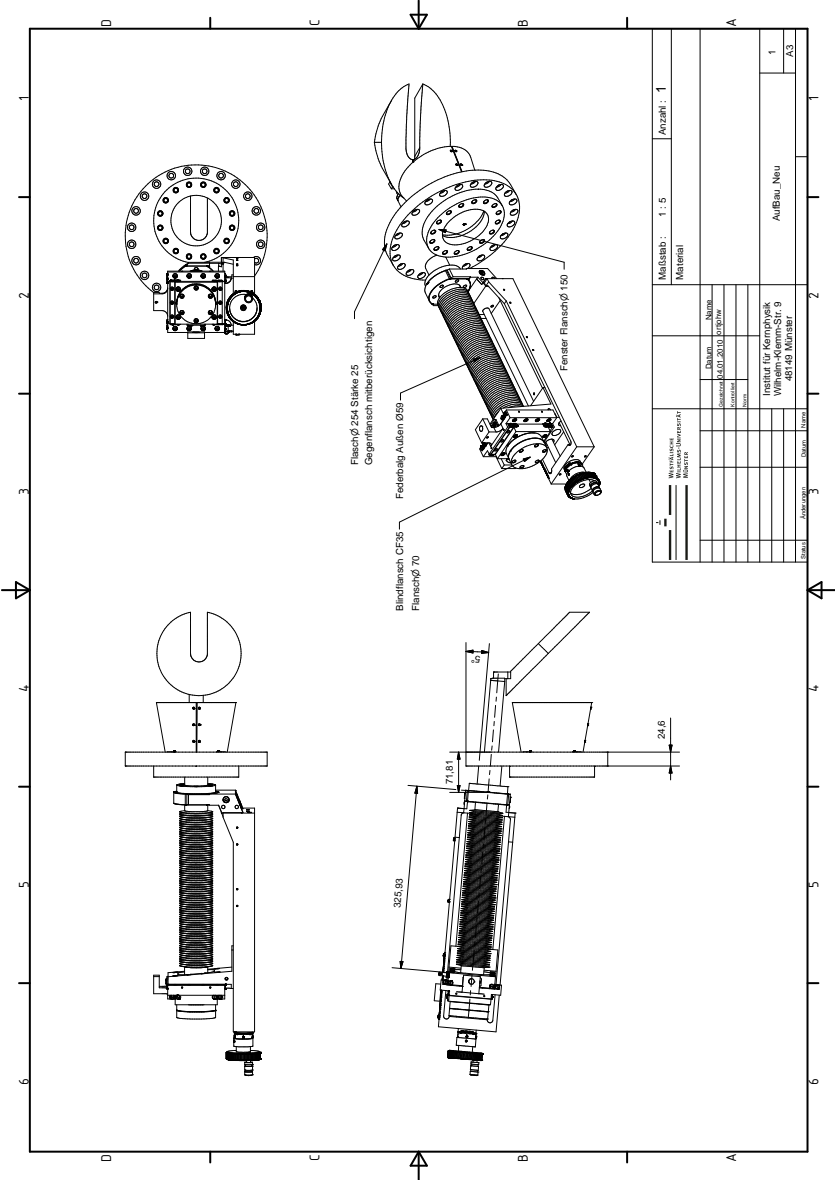
Appendix

A. Parabolic mirror setup specifications

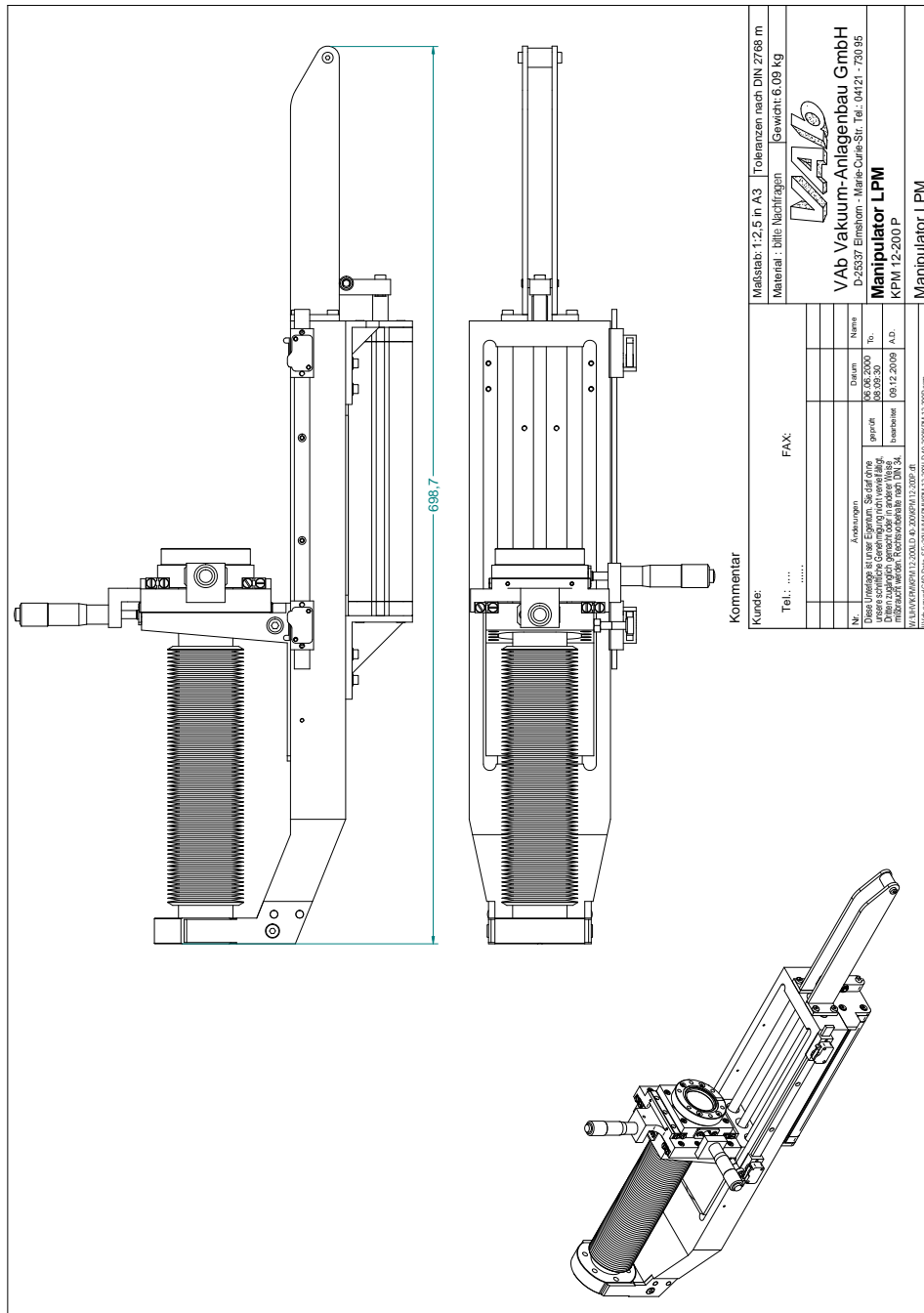Figure A.1.: Parabolic mirror system.

A.1. Linear feedthrough

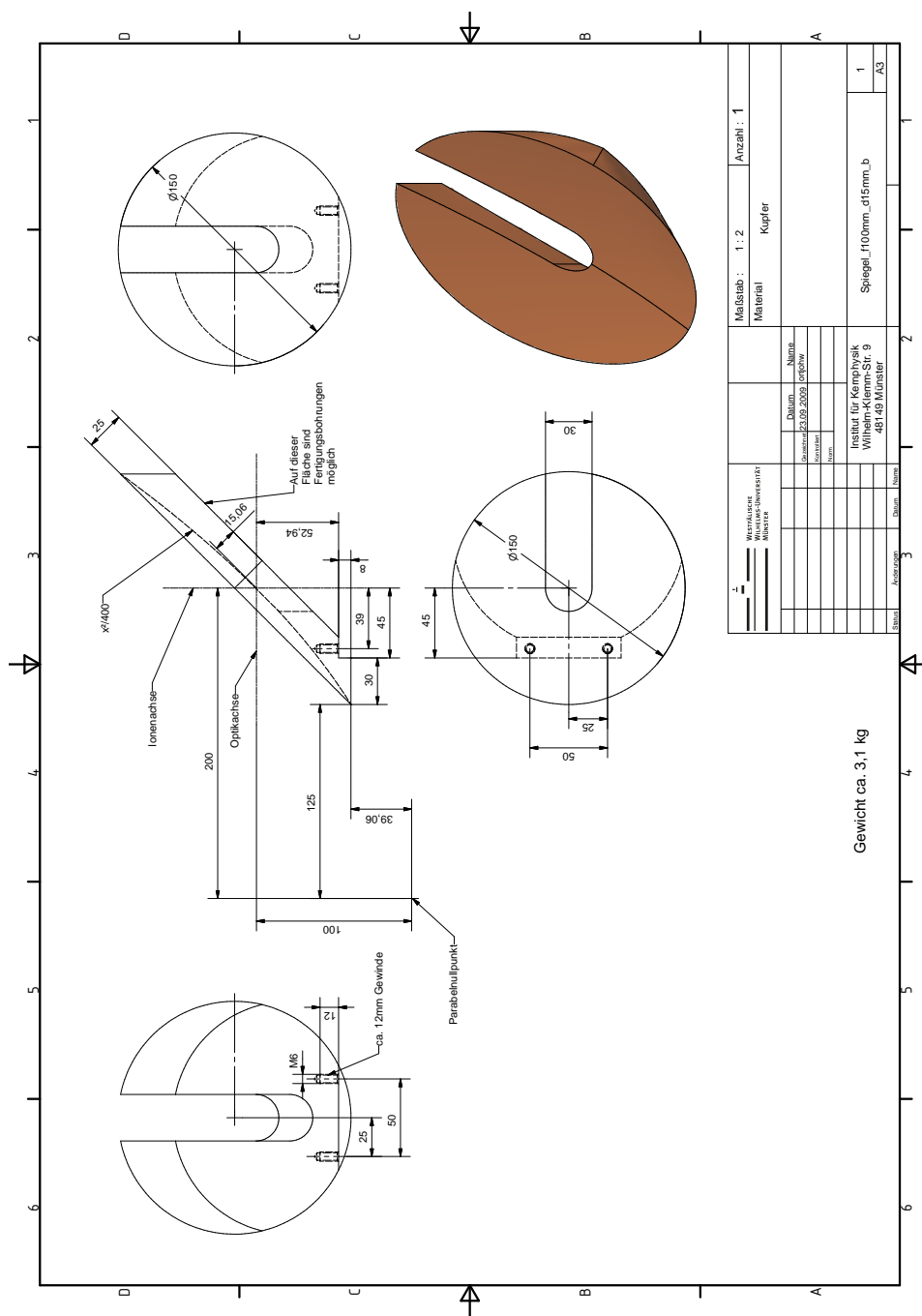
Figure A.2.: Linear feedthrough.

A.2. Parabolic mirror

Figure A.3.: Parabolic mirror.

A.3. Aluminum cone

Figure A.4.: Aluminum cone.

A.4. Flange and window

CF - Flansche

CF - Flansch Spezifikationen	1.4306	1.4429 ESU
Veredlungverfahren des Ausgangswerkstoffes		ESU erschmolzen
Weiterverarbeitung	geschmiedet	geschmiedet
	lösungsgeglüht	lösungsgeglüht
		Ni - kontrolliert
Magn. Permeabilität	<1,05	<1,005
Kohlenstoffgehalt	<0,02%	<0,02%
Brinell-Härte	170	170
Ausheiztemperatur	>450°C	>450°C
Internationale Norm	ISO 3669 (Pneurop 6606)	ISO 3669 (Pneurop 6606)
Dichtheitsprüfung aller Bauteile	He-Lecktest: <10^{-10} mbar l s^{-1}	He-Lecktest: <10^{-10} mbar l s^{-1}
erreichbares Endvakuum aller CF-Bauteile	<1 x 10^{-11} mbar	<1 x 10^{-11} mbar
UHV-gerechte Reinigung für alle CF-Bauteile	ja	ja
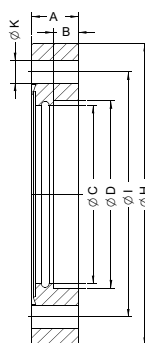
CF-Flansche fest	A	B	ø C	ø D	ø H	ø I	ø K
Nennweite	mm	mm	mm	mm	mm (Zoll)	mm	Anzahl x mm
DN 16 CF	7,3	2,5	16,0	18,2	33,8 (1 1/3")	27,0	6 x 4,3
DN 40 CF	13,0	8,2	38,5	42,6	69,4 (2 3/4")	58,7	6 x 6,5
DN 63 CF	17,5	9,5	67,0	70,3	113,5 (4 1/2")	92,1	8 x 8,4
DN 100 CF	19,8	10,3	100,0	104,3	151,6 (6")	130,2	16 x 8,4
DN 160 CF	22,2	12,7	150,0	154,3	202,4 (8")	181,0	20 x 8,4
DN 200 CF	24,6	15,1	200,0	205,5	253,2 (10")	231,8	24 x 8,4
DN 250 CF	24,6	15,1	250,0	256,3	306,0 (12")	284,0	32 x 8,4
DN 300 CF	28,5	15,9	300,0	306,4	355,6 (14")	325,4	30 x 10,5
DN 350 CF	28,5	15,9	350,0	356,4	419,1 (16 1/2")	388,9	36 x 10,5
DN 400 CF	28,5	15,9	400,0	406,5	457,1 (18")	431,8	36 x 10,5
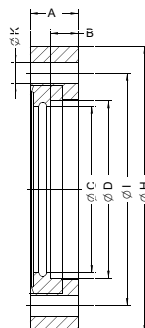
CF-Flansche drehbar	ø A	ø B	ø C	ø D	ø H	ø I	ø K
Nennweite	mm	mm	mm	mm	mm (Zoll)	mm	Anzahl x mm
DN 16 CF	7,3	2,5	16,0	18,2	33,8 (1 1/3")	27,0	6 x 4,3
DN 40 CF	13,0	8,2	38,5	42,6	69,4 (2 3/4")	58,7	6 x 6,5
DN 63 CF	19,0	9,5	67,0	70,3	113,5 (4 1/2")	92,1	8 x 8,4
DN 100 CF	21,5	112	100,0	104,3	151,6 (6")	130,2	16 x 8,4
DN 160 CF	24,0	14,5	150,0	154,3	202,4 (8")	181,0	20 x 8,4
DN 200 CF	24,6	15,1	200,0	205,5	253,2 (10")	231,8	24 x 8,4
DN 250 CF	24,6	15,1	250,0	256,3	306,0 (12")	284,0	32 x 8,4
DN 300 CF	28,5	15,9	300,0	306,4	355,6 (14")	325,4	30 x 10,5
DN 350 CF	28,5	15,9	350,0	356,4	419,1 (16 1/2")	388,9	36 x 10,5
DN 400 CF	28,5	15,9	400,0	406,5	457,1 (18")	431,8	36 x 10,5

Figure A.5.: Flange specifications.

CF - Sichtfenster

VAb
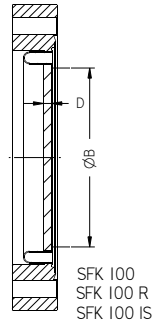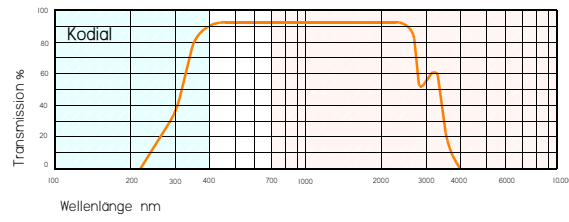
CF - Sichtfenster — Kodial

Nennweite	Maße in mm	Ø B	D	Artikel	€ / Stck
DN 16 CF		16	1	SFK 16	89,-
DN 40 CF (38)		38	2,5	SFK 38	85,-
DN 40 CF		40	3	SFK 40	93,-
DN 63 CF		63	3	SFK 63	125,-
DN 100 CF		89	4	SFK100	275,-
DN 160 CF		136	6,5	SFK160	425,-

Die Ausheiztemperatur von max 350°C sollte mit einem Temperaturanstieg von max 150 °C/h erreicht werden.
CF-Sichtfenster nur in Verbindung mit weichen Dichtungen einsetzen

CF - Sichtfenster — Kodial Anti-Reflex-Beschichtung MgF$_2$ beidseitig

Nennweite	Maße in mm	Ø B	D	Artikel	€ / Stck
DN 16 CF		16	1	SFK 16 R	235,-
DN 40 CF (38)		38	2,5	SFK 38 R	195,-
DN 40 CF		40	3	SFK 40 R	205,-
DN 63 CF		63	3	SFK 63 R	315,-
DN 100 CF		89	4	SFK100 R	555,-
DN 160 CF		136	6,5	SFK160 R	825,-

Die Ausheiztemperatur von max 350°C sollte mit einem Temperaturanstieg von max 150 °C/h erreicht werden.
CF-Sichtfenster nur in Verbindung mit weichen Dichtungen einsetzen

CF - Sichtfenster — Kodial InSnO$_2$-Beschichtung vakuumseitig

Nennweite	Maße in mm	Ø B	D	Artikel	€ / Stck
DN 40 CF (38)		38	2,5	SFK 38 IS	245,-
DN 63 CF		63	3	SFK 63 IS	395,-
DN 100 CF		89	4	SFK100 IS	395,-
DN 160 CF		136	6,5	SFK160 IS	625,-

Die Ausheiztemperatur von max 350°C sollte mit einem Temperaturanstieg von max 150 °C/h erreicht werden.
CF-Sichtfenster nur in Verbindung mit weichen Dichtungen einsetzen
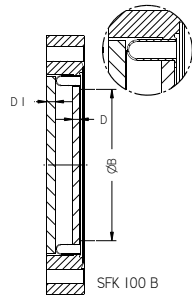
SFK 100
SFK 100 R
SFK 100 IS

CF - Sichtfenster — Kodial mit Bleiglas-Einsatz

Nennweite	Maße in mm	Ø B	D	D 1	Artikel	€ / Stck
DN 16 CF		16	2,5	5	SFK 16 B	125,-
DN 40 CF		38	2,5	5	SFK 38 B	155,-
DN 63 CF		63	3	5	SFK 63 B	262,-
DN 100 CF		89	4	5	SFK100 B	435,-

Die Ausheiztemperatur von max 350°C sollte mit einem Temperaturanstieg von max 150 °C/h erreicht werden.
CF-Sichtfenster nur in Verbindung mit weichen Dichtungen einsetzen

SFK 100 B

Figure A.6.: Window specifications.
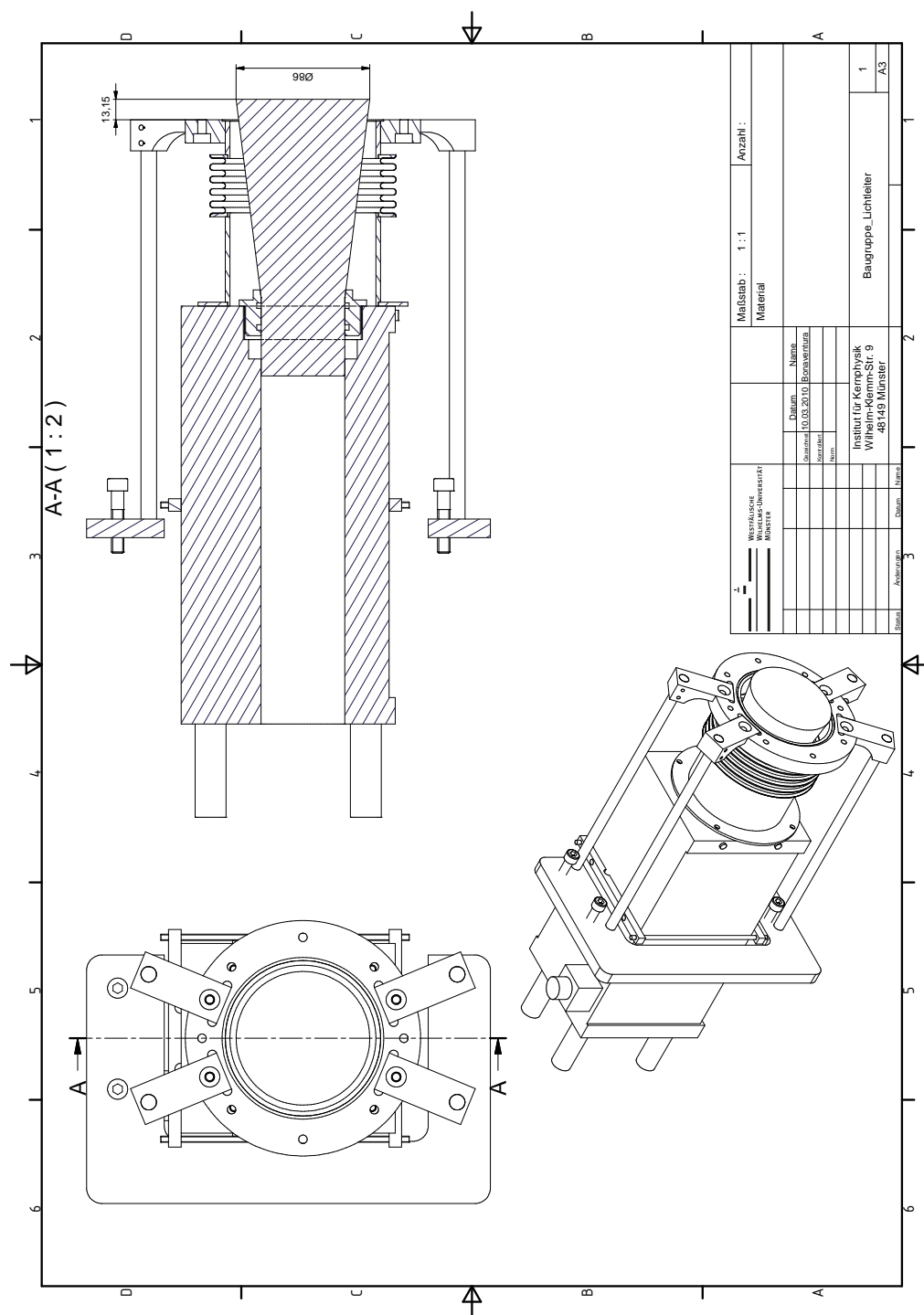
A.5. Adaptor

Figure A.7.: Specifications of the parabolic mirror setup adaptor.

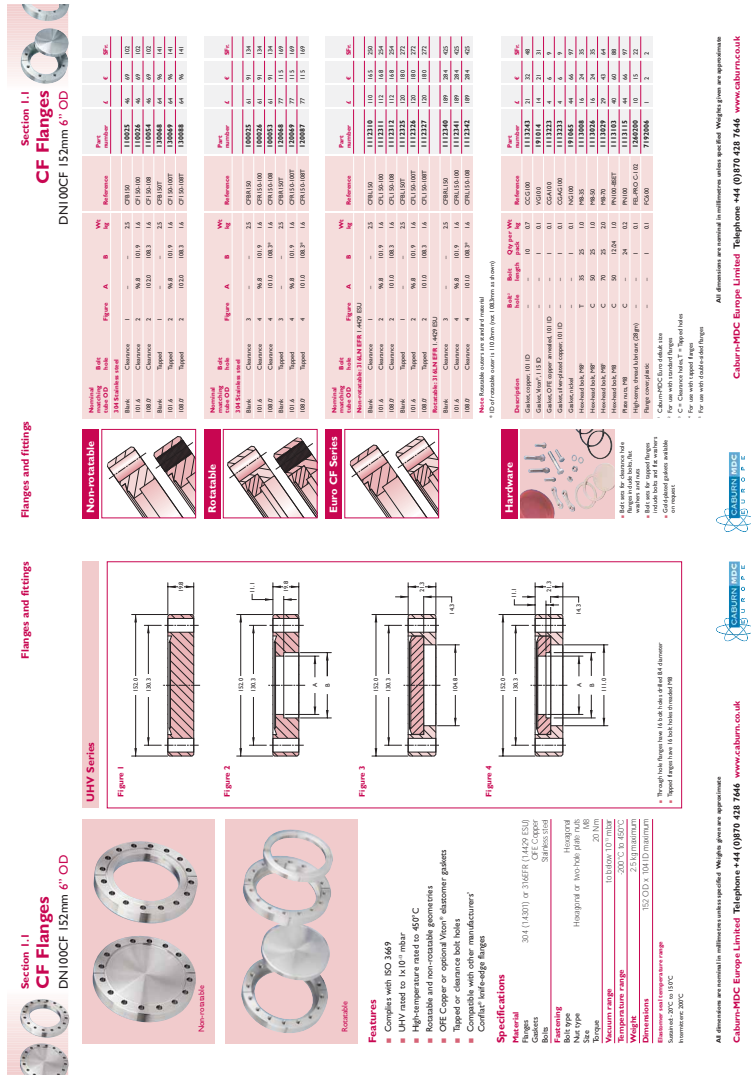# B. Forward detection setup specifications

B.1. Flange

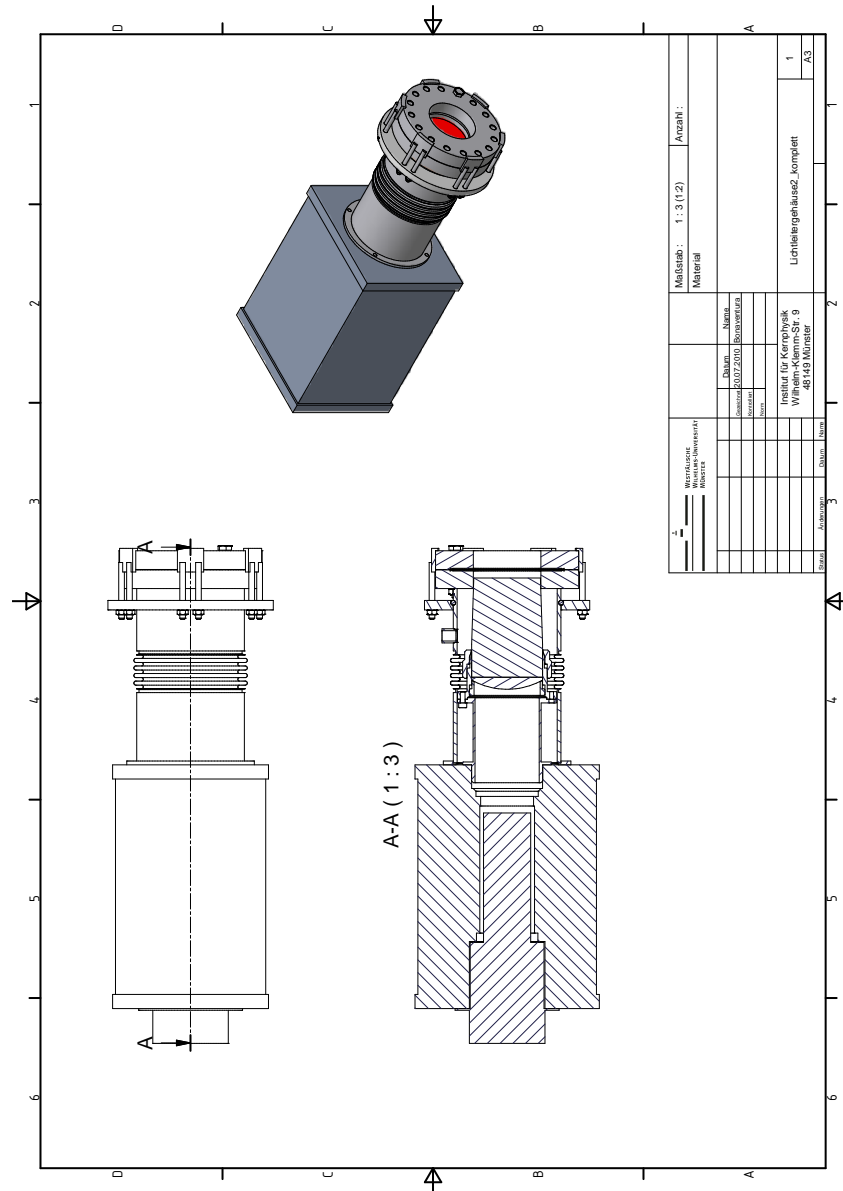Figure B.1.: Flange specifications.

B.2. Adaptor

Figure B.2.: Specifications of the forward detector adaptor.

C. Mirror shape

Two identical mirror blanks were received prior to the surface finish and both were measured on a 3D coordinate table in order to do a check of their shape.

As it can be seen on Figure C.1 the coordinate system in which the shape of the mirror was measured (x',y',z') isn't the same as the one used for the construction of the paraboloid shape. A 135° rotation must be performed. The corresponding rotation matrix around the y-axis is given by:

$$\begin{pmatrix} x \\ y \\ z \end{pmatrix} = \begin{pmatrix} \cos\theta & 0 & \text{-}\sin\theta \\ 0 & 1 & 0 \\ \sin\theta & 0 & \cos\theta \end{pmatrix} \begin{pmatrix} x' \\ y' \\ z' \end{pmatrix} \tag{C.1}$$

As the rotation has an angle of θ=135°, the points on the original axis-system have the equations

$$x = \cos135° \cdot x' - \sin135° \cdot z' = -\cos45° \cdot (x' + z') \tag{C.2}$$
$$y = y' \tag{C.3}$$
$$z = \sin135° \cdot x' + \cos135° \cdot z' = \cos45° \cdot (x' - z') \tag{C.4}$$
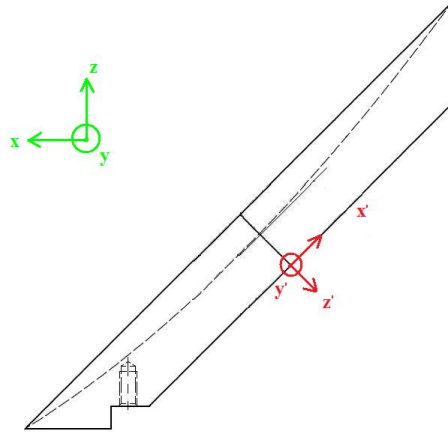
Figure C.1.: Coordinate systems of mirror shape measurement.

All measured points have been converted to the original coordinates. Now what has to be done is to adjust the points to the equation of a paraboloid not centered in the origin. This equation is given by:

$$z = \frac{(x-b)^2 + (y-c)^2}{a^2} + d \qquad (C.5)$$

Where (b,c,d) is the origin of the paraboloid in the original coordinates. As it has been shown on Chapter 4.2.2, the value chosen for the parameter a is 20 mm.
After the fit of the parameters with gnuplot, the value found for the two mirrors are the following:

$$a_1 = 19.92 \pm 0.04$$

$$a_2 = 20.002 \pm 0.012$$

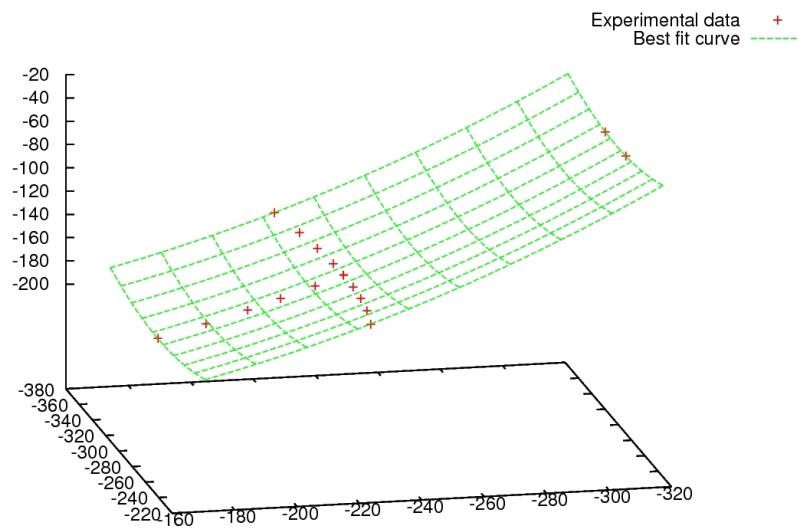So the parameter a of the curvature of the mirror blanks corresponds in both cases to the theoretical value with a relative error of <0.4%.

Figure C.2.: Plot of the mirror shape of mirror blank 1.

From these measurements it has been concluded, that both mirror blanks can be used for production of the actual parabolic mirror.

D. Data Sheets and Quantum Efficiencies

D.1. Hamamatsu PMT R1017

D.1.1. Data Sheet

R1017

Part Number	R1017
Type	Head on
Size	51mm
ActiveDia/L	46mm
Min λ	300nm
Max λ	900nm
Peak Sens.	650nm
Cathode Radiant Sensitivity	50mA/W
Window	Borosilicate
Cathode Type	Multialkali
Cathode Luminous Sensitivity	230mA/lm
Red White Ratio	0.35
Anode Luminous Sensitivity	100A/lm
Gain	4.3E+05
Dark Current after 30 min.	9nA
Rise Time	16ns
Transit Time	70ns
Number of Dynodes	12
Applied Voltage	1000V
Multi Anode	N
Magnetic Shield	E989-05
Power Supply	C3830(100V) C4720 C4710
Amplifier	C7319 C6438 C5594 M7279 M8879

Figure D.1.: Hamamatsu PMT R1017 datasheet.

D.1.2. Quantum efficiency
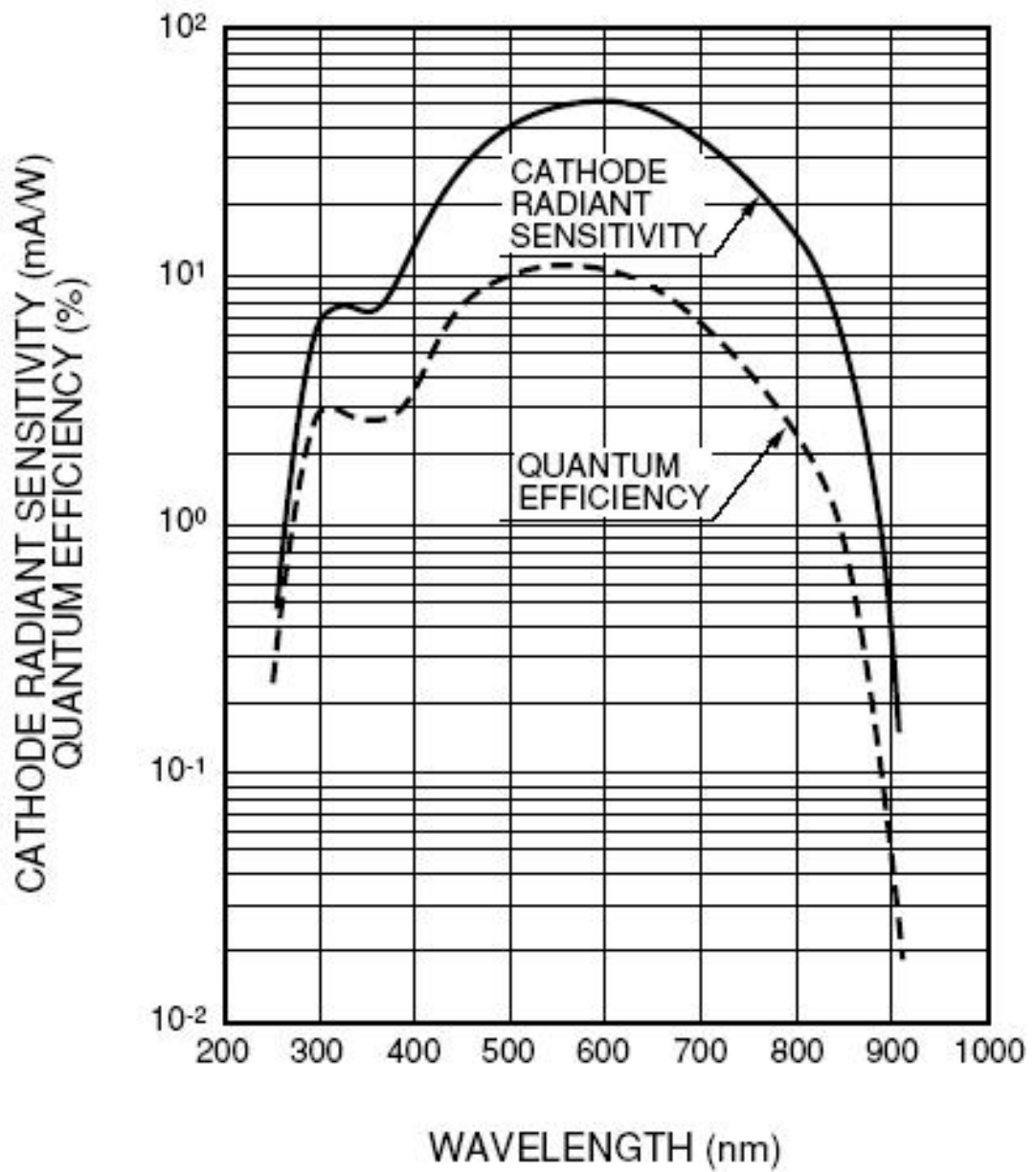
Figure D.2.: R1017 quantum efficiency.

D.2. Hamamatsu PMT R943-02

D.2.1. Data Sheet

PHOTOMULTIPLIER TUBE R943-02

MAXIMUM RATINGS (Absolute Maximum Values)

Parameter	Value	Unit
Supply Voltage		
Between Anode and Cathode	2200	V
Between Anode and Last Dynode	250	V
Average Anode Current [B]	1	μA
Average Pulse Count Rate [C]	6×10^6	s^{-1}
Average Cathode Current [D]	1	nA

CHARACTERISTICS (at 25 °C)

Parameter	Min.	Typ.	Max.	Unit
Cathode Sensitivity [E]				
Quantum Efficiency				
at 253.7 nm (Hg-Line)	—	15	—	%
at 632.8 nm (He-Ne Laser)	—	14	—	%
Luminous [F]	300	600	—	μA/lm
Radiant at 253.7 nm (Hg-Line)	—	30	—	mA/W
at 632.8 nm (He-Ne Laser)	—	70	—	mA/W
at 700 nm	—	71	—	mA/W
at 852.1 nm (Cs-Line)	—	65	—	mA/W
Red/White Ratio [G]	—	0.58	—	—
Anode Sensitivity [H]				
Luminous [F]	150	300	—	A/lm
Radiant at 253.7 nm (Hg-Line)	—	1.5×10^4	—	A/W
at 632.8 nm (He-Ne Laser)	—	3.5×10^4	—	A/W
at 700 nm	—	3.6×10^4	—	A/W
at 852.1 nm (Cs-Line)	—	3.3×10^4	—	A/W
Gain [H]	—	5×10^5	—	—
Equivalent Anode Dark Current [J]	—	1	10	nA
Anode Dark Counts [K]	—	20	50	s^{-1}
Single Photoelectron PHD (Peak to Valley Ratio)	—	2.3	—	—
Time Response [H]				
Anode Pulse Rise Time [L]	—	3.0	—	ns
Electron Transit Time [M]	—	23	—	ns

NOTES

[A] For cooling operation, another ceramic socket, type number E678-21D is recommended, because the teflon socket type number E678-21C supplied with the tube is not suitable for cooling operation due to its high thermal expansion coefficient. Alternatively, it is recommended to solder a resistor, capacitor, etc. directly on stem pins using a socket contact (100-2520S) supplied by Winchester.

[B] Averaged over any interval of 30 seconds maximum.

[C] Measured at single photoelectron level. The discriminator level is set at valley point.

[D] In practical operation, the cathode current should be lower than 0.1 nA to prevent shortening the life of the photocathode.

[E] Supply voltage is 150 volts between the cathode and all other electrodes.

[F] The light source is a tungsten filament lamp operated at a distribution temperature of 2856 K.

[G] The quotient of the cathode sensitivity measured with the light source is the same as Note [E] passing through a red filter (Toshiba R-68) divided by the cathode luminous sensitivity without the red filter.

[H] Measured with supply voltage and voltage distribution ratio in Table 1.

[J] Measured with supply voltage to provide the anode luminous sensitivity of 200 (A/lm) and the voltage distribution ratio in Table 1 after 30 minute storage in the darkness.

[K] Measured with supply voltage that gives 2×10^6 gain and with the voltage distribution ratio shown in Table 1 after one hour storage in the cooler set at -20 °C.

The discriminator is set at 1/3 of a single photoelectron level.

[L] The rise time is the time it takes the output pulse to rise from 10 % to 90 % of the peak amplitude when the entire photocathode is illuminated by a delta function light pulse.

[M] The electron transit time is the interval between the arrival of a delta function light pulse at the entrance window of the tube and the time when the output pulse reaches the peak amplitude. In measurement the entire photocathode is illuminated.

Table 1: Voltage Distribution Ratio

Electrode	K	Dy1	Dy2	Dy3	Dy4	Dy5	Dy6	Dy7	Dy8	Dy9	Dy10	P
Distribution Ratio	3	1.5	1	1	1	1	1	1	1	1	1	1

Supply Voltage : 1500 V,   K : Cathode,   Dy : Dynode,   P : Anode

Replacement Information

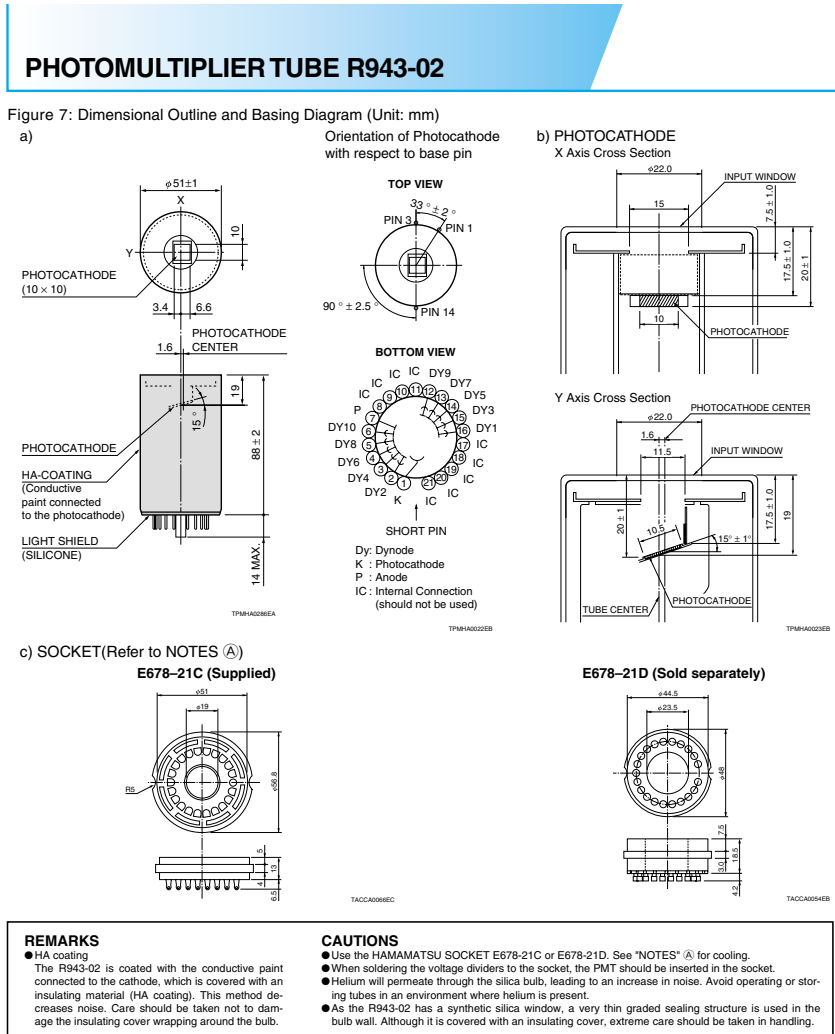The R943-02 is similar to the Burle C31034 series photomultiplier tube. The base and voltage divider are different.

> **Warning–Personal Safety Hazards**
> Electrical Shock — Operating voltages
> applied to this device present a shock hazard.

Figure D.3.: Hamamatsu PMT R943-02 datasheet.

D.2.2. Drawings

PHOTOMULTIPLIER TUBE R943-02

Figure 7: Dimensional Outline and Basing Diagram (Unit: mm)

a)

Orientation of Photocathode with respect to base pin

b) PHOTOCATHODE
X Axis Cross Section

Y Axis Cross Section

c) SOCKET(Refer to NOTES Ⓐ)

E678–21C (Supplied)

E678–21D (Sold separately)

REMARKS
● HA coating
The R943-02 is coated with the conductive paint connected to the cathode, which is covered with an insulating material (HA coating). This method decreases noise. Care should be taken not to damage the insulating cover wrapping around the bulb.

CAUTIONS
● Use the HAMAMATSU SOCKET E678-21C or E678-21D. See "NOTES" Ⓐ for cooling.
● When soldering the voltage dividers to the socket, the PMT should be inserted in the socket.
● Helium will permeate through the silica bulb, leading to an increase in noise. Avoid operating or storing tubes in an environment where helium is present.
● As the R943-02 has a synthetic silica window, a very thin graded sealing structure is used in the bulb wall. Although it is covered with an insulating cover, extreme care should be taken in handling.

Figure D.4.: Hamamatsu PMT R943-02 drawings.

D.2.3. Quantum efficiency
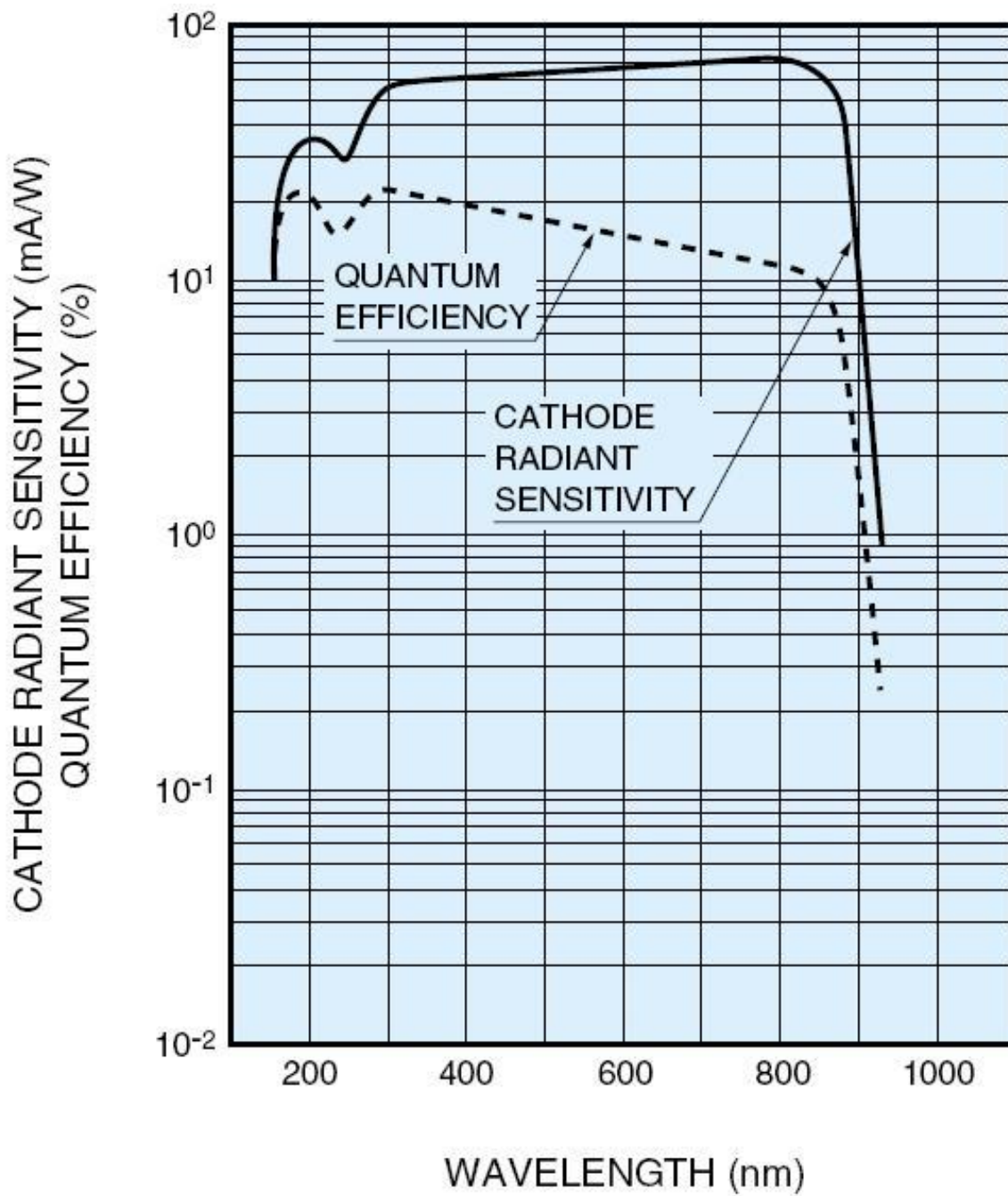
Figure D.5.: Hamamatsu PMT R943-02 quantum efficiency.

D.3. Perkin Elmer CPM 1993

D.3.1. Data Sheet

PerkinElmer
precisely.

test report

PerkinElmer

Optoelectronics GmbH & Co. KG

Wenzel-Jaksch-Straße 31

65199 Wiesbaden, Germany

Phone: +49 (6 11) 4 92-0

Fax: +49 (6 11) 4 92-1 77

http://www.perkinelmer.com

CPM-Channel Photomultiplier C 1993 P

Serial Number:	C806-83
Type of Photocatode:	Yellow Extended
Faceplate Material:	UV-Glass
Spectral sensitivity:	185 - 750 nm
Cathode sensitivity @ 560 nm:	6,1 %
Gain @ 2000V:	6,1E+6
Dark current @ 2000V:	43,3 pA
Bias Current @ 2000V:	34 µA
Single photo electron gain @ 3000V:	2,2E+8
Dark counts @ 3000 V:	19 cps

04.04.08

CAUTION

High light levels can damage the photocathode permanently. When high voltage is applied, it has to be assured, that maximum signal current will not exceed the value of 10 µA (max. 30 sec).

High Voltage Warning:

This product is operated at high voltage. Extreme care must be taken to ensure operator's safety and to avoid damage to other instruments. Avoid direct contact with the photomultiplier when high voltage is applied. Keep at least 5 mm space around the cathode when operated with negative high voltage.

Figure D.6.: Perkin Elmer CPM 1993 datasheet.

D.3.2. Quantum efficiency
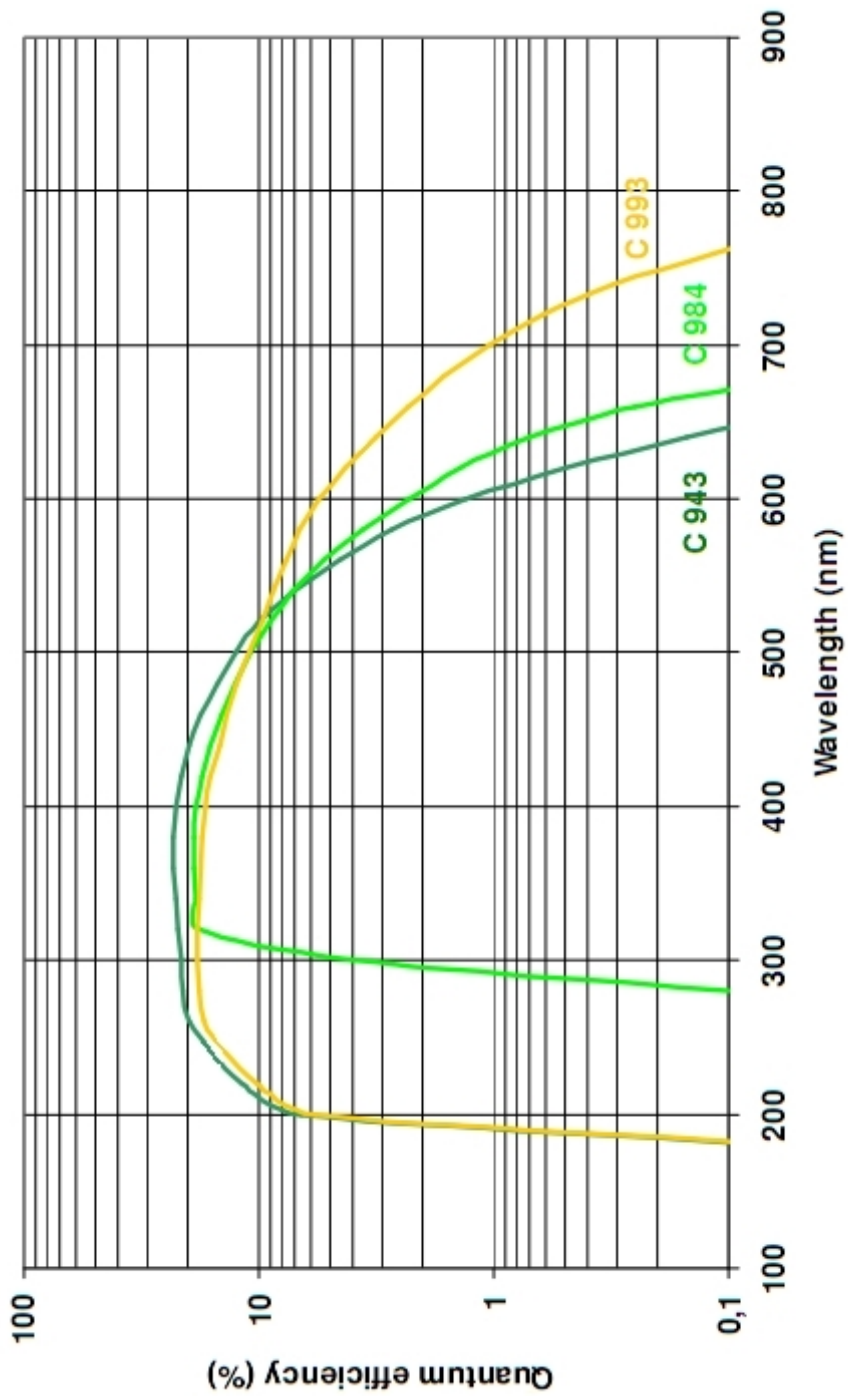
Figure D.7.: CPM 1993P quantum efficiency.

Bibliography

[Ala10] Alanod Company: http://www.alanod.de/

[And10] Z. Andjelkovic, S. Bharadia, B. Sommer, M. Vogel, W. Nörterhäuser *Towards high precision in-trap laser spectroscopy of highly charged ions.* Hyperfine interact 196:81-91 (2010).

[Ani10a] D. Anielski: *Entwicklung eines Detektoraufbaus zur Bestimmung der 2s-Hyperfeinstrukturaufspaltung von $^{209}Bi^{80+}$ am Experimentierspeicherring an der GSI.* Diploma Thesis in Münster University, 2010.

[Ani10b] D. Anielski, V.M. Hannen, H-W. Ortojohann: *Zeichnungen und Spezifikationen des beweglichen Parabolspiegels fur Laserspektroskopie am ESR.* Institut für Kernphysik, WWU Münster, 2010.

[Ari10] J.M. Arias y A.M. Moro, *"Apuntes de Fsica Atmica y Molecular".* Universidad de Sevilla, Spain. Unpublished.

[Bei98] Beiersdorfer, P., A. L. Osterheld, J. H. Scofield, J. R. C. López-Urrutia, and K. Widmann: *Measurement of QED and Hyperfine Splitting in the $2s_{1/2}$- $2p_{3/2}$ X-Ray Transition in Li-like $^{209}Bi^{80+}$.* Phys. Rev. Lett. 80 (1998) 3022.

[Bei00a] T. Beier: *The g_j factor of a bound electron and the hyperfine structure splitting in hydrogenlike ions.* Phys. Rep. 339, 79-213 (2000).

[Bei00b] T. Beier et al: *The g_j factor of a bound electron in hydrogenlike ions.* Phys. Rev. A, Volume 62, 2000.

[Bei01] P. Beiersdorfer, S.B. Utter, K.L. Wong, J.R. Crespo Lopez-Urrutia, J.A. Britten, H. Chen, C.L. Harris, R.S. Thoe, D.B. Thom, E. Träbert, M.G.H. Gustavsson, C. Forssen, A.M. Martensson-Pendrill: *Hyperfine structure of hydrogenlike thallium isotopes.* Phys. Rev. A, **64**, 032506 (2001).

[Boh50] A.Bohr, V.S.Weisskopf: *The Influence of Nuclear Structure on the Hyperfine Structure of Heavy Elements.* Physical Review, Volume 77, 1950.

[Bor00] Borneis, S., A. Daxa, T. Engel, C. Holbrow, G. Huber, T. Khl, D. Marxa, P. Merz, W. Quint, F. Schmitt, P. Seelig, M. Tomaselli, H. Winter, K. Beckert, B. Franzke, F. Nolden, H. Reich, and M. Steck, *Ground-state hyperfine structure of heavy hydrogen-like ions.*, Hyperfine Interact. 127 (2000) 305.

[Cae02] C.A.E.N. Company: *Technical information Manual N843.*, 2002.

[Coh77] C.Cohen-Tannoudji, B.Diu, F.Laloë: *Quantum Mechanics.* Wiley-Interscience, 1977.

[Cre96] J.R. Crespo Lopez-Urrutia, P. Beiersdorfer, D.W. Savin, K. Widmann: *Direct Observation of the Spontaneous Emission of the Hyperfine Transition F=4 to F=3 in Ground State Hydrogenlike $^{165}Ho^{66+}$ in an Electron Beam Ion Trap.* Phys. Rev. Lett. **77**, 826-829 (1996).

[Cre98] J.R. Crespo Lopez-Urrutia, P. Beiersdorfer, K. Widmann: *Nuclear magnetization distribution radii determined by hyperfine transitions in the 1s level of H-like ions $^{185}Re^{74+}$ and $^{187}Re^{74+}$.* Phys. Rev. A **57** 879-887 (1998).

[Dem05] W. Demtröder: *Experimenalphysik 3 - Atome, Moleküle und Festkörper.* Springer Berlin Heidelberg New York, 2005.

[Fey61] R.P.Feynman: *Quantum Electrodynamics.* W.A.Benjamin, New York, 1961.

[Fey85] R.P.Feynman: *QED: The Strange Theory of Light and Matter.* Princeton University Press, 1985.

[Fra87] B.Franzke: *The heavy ion storage and cooler ring project ESR at GSI.*, Nuclear Instruments and Methods in Physics Research B24/25 (1987) 18-25.

[Gri87] D.J.Griffiths: *Introduction to elementary particles.* Harper & Row Publisher, New York, 1987.

[Ham01] Hamamatsu Company: *Photon counting: Using photomultiplier tubes.* 2001.

[Ham08a] Hamamatsu Company: *Photomultiplier Tubes, Basic and Applications.* PMT Handbook, 3rd Edition. 2008.

[Ham08b] Daniel Hampf: *Untersuchung der APD S1315 von RMD im Hinblick auf ihren Einsatz als Detektor am SpecTrap Experiment.* Diploma Thesis in Münster University, 2008.

[Ham10] Hamamatsu Company: http://www.hamamatsu.com/

[Han10] Volker Hannen, Institut für Kernphysik, WWU Münster, 2010, *priv.comm.*

[Her07] T.Herrmannsdörfer, J.Wosnitza: *100 Tesla fr die Forschung. Das Hochfeld-Magnetlabor in Dresden.* Physik in unserer Zeit, Volume 38, 2007.

[Hit10] HITRAP-Website: http://www.gsi.de/forschung/ap/projects/hitrap/index.html

[Joh70] J. Johnson and R. A. Sorensen: *Magnetic Hyperfine structure of muonic atoms.* Phys. Rev. C 2, 102 (1970).

[Jöh07] Raphael Jöhren: *Entwicklung eines automatischen Messsystems zur Qualitätskontrolle der Elektrodenmodule für das KATRIN Hauptspektrometer.* Diploma Thesis in Münster University, 2007.

[Jöh10] Raphael Jöhren, Institut für Kernphysik, WWU Münster, 2010.

[Kla94] I. Klaft, S. Borneis, T. Engel, B. Fricke, R. Grieser, G. Huber, T. Kühl, D. Marx, R. Neumann, S. Schröder, P. Seelig, L. Völker: *Precision Laser Spectroscopy of the Ground State Hyperfine Splitting of Hydrogenlike $^{209}Bi^{82+}$*. Phys. Rev. Lett. **73**, 2425-2427 (1994).

[Krä07] Jörg Krämer: *Aufbau und Test einer Ionenfalle für die Laserspektroskopie an hochgeladenen Ionen.* Diplom Thesis on Mainz University, 2007.

[Kug10] Kugler Company: http://www.kugler-precision.com/

[Küh96] T. Kühl et al. :*Precision laser spectroscopy of heavy charged ions.* Hyperfine Interactions 99 (1996) 145-153.

[Lin10] Linos Company http://www.linos.com/

[Loc10a] M. Lochmann: *Ein Experiment zur laserspektroskopischen Bestimmung der Hyperfeinstruktur von lithiumähnlichen $^{209}Bi^{80+}$*. Poster in SNI-Tagung, 2010.

[Loc10b] Matthias Lochmann, GSI, Darmstadt, 2010: *priv. comm.*

[Loc10c] Matthias Lochmann: *LIBELLE monthly report.* March-April, 2010.

[Loc10d] Matthias Lochmann: *LIBELLE monthly report.* June, 2010.

[Lop10a] Rubén López Coto: *Detector system for hyperfine structure measurements at the Experimental Storage Ring (ESR) at GSI.* Talk in DPG Tagung Bonn, 2010.

[Lop10b] Rubén López Coto: *Parasitic test measurements at the Experimental Storage Ring (ESR) at GSI for the $^{209}Bi^{80+}$ experiment.* April report, 2010.

[Ltu10] LT-Ultra Precision Technology: http://www.lt-ultra.com/

[Man10] P.P. Man *NMR Periodic Table for half-integer quadrupole spins.* Paris, France, 2010 http://www.pascal-man.com/periodic-table/periodictable.html#

[Mig83] A.B. Migal: *Theory of Finite Fermi Systems and properties of Atomic Nuclei.* Nauka, Moscow, 1983.

[Nör07] Wilfried Nörterhäuser: *Laserspektroskopie hochgeladener Ionen an HiTrap.* Talk on the IKP Münster research seminar, 2007.

[Nör08] Wilfried Nörterhäuser: *Laser spectroscopy of lithium-like Bismuth at the ESR.* Experiment proposal, 2008.

[Nov08] Christian Novotny: *Laser spectroscopy on lithium ions stered at a velocity of 33.8% of the speed of light.* Dissertation for the degree of Doctor of Natural Science, Johannes Gutenberg Mainz University, 2008.

[Per05] Perkin Elmer Company: *CPM Datasheet.* http://optoelectronics.perkinelmer.com/content/relatedlinks/cpmdatasheet.pdf

[Per10] Perkin Elmer Company: www.perkinelmer.de

[Rei07] Martina Reinhardt *Entwicklung eines Lasersensors und Materialcharakterisierung für die Drahtelektroden des KATRIN Hauptspektrometers.* Diploma Thesis in Münster University, 2007

[Ros32] J.E.Rosenthal, G.Breit: *The Isotope Shift in Hyperfine Structure.* Physical Review, Volume 41, 1932.

[Sap01] Sapirstein, J. and K. T. Cheng: *Hyperfine splitting in lithiumlike bismuth.* Phys. Rev. A 63 (2001) 032506.

[See99] Peter Seelig: *Laserspektroskopie der 1s-Hyperfeinstrukturaufspaltung an wasserstoffähnlichem $^{207}Pb^{81+}$.* Dissertation on Mainz University, 1999.

[Sha97] V.M. Shabaev et al.: *Ground-state hyperfine splitting of high-Z hydrogenlike ions.* Phys. Rev. A 56, 252 (1997).

[Sha98] V.M. Shabaev, M. Tomaselli, T. Kühl, A.N. Artemyev, and V.A. Yerokhin: *Transition energy and lifetime for the ground-state hyperfine splitting of high-Z lithiumlike ions.* Phys. Rev. A 57, 149 (1998).

[Sha00] V. M. Shabaev, A. N. Artemyev, O. M. Zherebtsov, V. A. Yerokhin, G. Plunien, and G. Soff: *Calculation of the hyperfine structure of heavy H- and Li-like ions.* Hyperfine Interact. 127 (2000) 279.

[Sha01] V.M. Shabaev et al.: *Towards a test of QED in Investigations of the Hyperfine Splitting in Heavy Ions.* Phys. Rev. Lett. 86, 3959 (2001).

[Sph10] Laser-SpHERe-Group, Group leader:Wilfried Nörterhäuser, Johannes Gutenberg-Universität, Mainz, 2010.

[Str00] H.H.Stroke et al.: *Bohr-Weisskopf effect: influence of the distributed nuclear magnetization on HFS.* Hyperfine Interactions 129 (2000) 319 335.

[Tho10] Thorlabs Company: www.thorlabs.com

[Tom95] M. Tomaselli, S. M. Schneider, E. Kankeleit, and T. Khl: *Ground-state magnetization of ^{209}Bi in a dynamic-correlation model.* Phys. Rev. C 51, 2989 (1995).

[Tom00] M. Tomaselli, S. Fritzsche, T. Kühl, and H. Winter: *Hyperfine structure of Li-like Bismuth.* Hyperfine Interact. 127 (2000) 315.

[Vab10] VAB Vacuum Company: http://vab-vakuum.de/

Acknowledgements